Quantum information processing beyond ten ion-qubits

A dissertation submitted to the
FACULTY OF
MATHEMATICS, COMPUTER SCIENCE AND PHYSICS,
OF THE LEOPOLD-FRANZENS UNIVERSITY OF INNSBRUCK,

in partial fulfillment
of the requirements for the degree of

DOCTOR OF NATURAL SCIENCE
(DOCTOR RERUM NATURALIUM)

carried out at the Institute of Experimental Physics
under the guidance of Rainer Blatt

presented by
THOMAS MONZ

AUGUST 2011

Kurzfassung

Die Verarbeitung von Quanteninformation basiert grossteils auf zwei Aspekten: a) der Anwendung von Quantenoperationen hoher Güte sowie b) der Vermeidung bzw. Unterdrückung von Dekohärenzprozessen welche Quanteninformation vernichtet. Die hier präsentierte Arbeit zeigt unsere Fortschritte auf dem Gebiet der experimentalen Quanteninformationsverarbeitung in den letzten Jahren. Auf dem Gebiet der Implementierung und Charakterisierung zahlreicher Quantenoperationen wird unter anderem die erste Realisierung des Quanten-Toffoli Gatters in einem Ionenfallenquantencomputer präsentiert. Die Erzeugung von verschränkten Zuständen mit bis zu 14 Quantenbits dient als Grundlage zur Untersuchung von Dekohärenzprozessen im verwendeten Quantencomputer. Auf Grundlage der realisierten Quantenoperationen sowie den Erkenntnissen zu dominanten Rauschprozessen in der verwendeten Apparatur werden die "Verschränkung von Teilchen ohne direkte Wechselwirkung", besser bekannt als "entanglement swapping", sowie Quantenoperationen innerhalb eines dekohärenzfreien Unterraums demonstriert.

Abstract

Successful processing of quantum information is, to a large degree, based on two aspects: a) the implementation of high-fidelity quantum gates, as well as b) avoiding or suppressing decoherence processes that destroy quantum information. The presented work shows our progress in the field of experimental quantum information processing over the last years: the implementation and characterisation of several quantum operations, amongst others the first realisation of the quantum Toffoli gate in an ion-trap based quantum computer. The creation of entangled states with up to 14 qubits serves as basis for investigations of decoherence processes. Based on the realised quantum operations as well as the knowledge about dominant noise processes in the employed apparatus, entanglement swapping as well as quantum operations within a decoherence-free subspace are demonstrated.

Contents

Chapter 1

Introduction

Quantum mechanics has been one of the main focuses in the field of experimental physics for the last century. Based on experiments concerning the photoelectric effect, Einstein noted that energy is only exchanged in discrete packets [1] - an observation for which he received a Nobel prize in 1922. This discovery led to further investigations about the behaviour and description of atoms. In 1926, Schrödinger provided an equation to describe physics at an atomic scale [2] - work for which he received a Nobel prize in 1933. His eponymous equation describes particles and photons, and quantum mechanics in general, in terms of wave phenomena. Here, quantum effects need not only be considered in terms of quantised energies - but also in terms of waves and phases which may interfere constructively or destructively, similar to the interference observed with light. However, discussions regarding the interaction of single atoms and light fields were largely theoretical, as Schrödinger summarised in 1952 by the expression: "We never experiment with just one electron or atom or (small) molecule. In thought-experiments we sometimes assume that we do; this invariably entails ridiculous consequences... we are not experimenting with single particles, any more than we can raise Ichthyosauria in the zoo" [3].

Schrödinger's statement turned out to be wrong. Only one year later, in 1953, Wolfgang Paul suggested the confinement of charged particles using electric fields [4] - work for which he (together with Norman Ramsey) received a Nobel prize in 1989. In 1980 Neuhauser, Toschek and Dehmelt managed to store a single Barium atom in an ion-trap [5]. From there it was a short step to detect "quantum jumps", that is, the direct observation of sudden jumps between electronic states within a single atom [6–8].

In these experiments, the electronic structure of atoms is generally very rich, making interactions on few, desired transitions challenging. The progress in creating narrow-linewidth lasers enables experimentalists to overcome this problem. Here, a monochromatic light-field allows one to approximate an atom as a two-level system with states $|0\rangle$ and $|1\rangle$ (and neglect the rest of the atomic level structure). This binary approach to describe the state of an atom steered investigations in analogy to classical computation - especially whether information can be stored in single atoms and to which degree this would open up new possibilities for fast and efficient computations.

In contrast to a classical computer, information stored in a single atom follows the laws of quantum mechanics. A quantum bit, or qubit, is able to be not only in either $|0\rangle$ or $|1\rangle$, it may also be in any superposition of these two states. This leads to new possibilities that are extensively investigated in the field of quantum information processing [9] with results such as

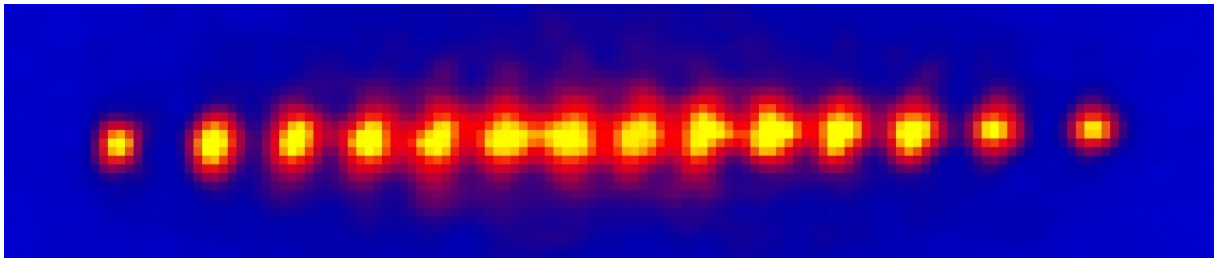

Figure 1.1: 14 bright $^{40}Ca^{+}$ ions: Stored in a linear ion trap, a string of ions serves as a register for quantum information processing experiments.

Shor's factoring algorithm [10], which may find the factors of large numbers notably faster than any classical algorithm, or Grover's search algorithm [11], which can be used to efficiently find elements in an unsorted database.

The requirements for a functional quantum computer have been summarised by DiVincenzo [12]: it is imperative to be able to initialise a well-defined quantum register, to manipulate it and be able to retrieve the information before the information is lost. These criteria have originally been suggested with regards to quantum computation and are, besides their challenging nature, partially fulfilled in several current experiments. However, devices that fulfil these criteria cannot only be applied to quantum computation tasks. For instance, quantum simulations may be performed, which allow the investigation of problems that can hardly be tackled with classical computers [13, 14]. Alternatively, quantum metrology can be implemented by employing quantum effects to outperform classical precision measurements [15]. In that regard, any experiment excelling in the field of coherent quantum control represents an ideal candidate for investigations in the general field of quantum mechanics.

Several approaches have been devised to experimentally study and implement a number of topics related to the broad field of quantum information processing, quantum metrology and quantum simulations, such as employing neutral atoms, photons and several other systems [16]. Charged atoms stored in an ion-trap show several characteristics that currently outperform most other experiments in the field of coherent quantum control: Stored ions are generally well localised which simplifies manipulations of a specific qubit. Ultra-high vacuum apparatuses allow the description of stored ions with few considerations concerning collisions with other atoms and enable the experimentalist to run experiments on the very same ion for several hours or days. Initialisation of the quantum register, as required by DiVincenzo, can be achieved by optical pumping with fidelities close to 100%. State-of-the-art control electronics for lasers and magnetic fields induce almost negligible noise on the ion-qubits, allowing for long information-storage times in ions. The remaining point mentioned by DiVincezo, qubit readout, is generally implemented with high fidelity via electron-shelving [17], a technique discussed in more detail in Sec. 4.

In the presented work, $^{40}Ca^{+}$ ions are stored in linear crystals, as shown in Fig. 1.1, for several days. Here, different electronic states of the ions serve as quantum states to encode information. Several parameters in our experiment facilitate high-performance quantum information processing. For our trap parameters, the ions are well localised to about 11 nm. In comparison to the wavelength of the qubit-manipulating light field at 729 nm, this tight confinement allows for phase-stable and coherent operations on ion-qubits. The average distance

between ions is usually about 4 μm, large enough to individually address single qubits within the diffraction limit of a focused beam. These starting conditions for ion-trap based quantum computation have been the stepping stone for several experiments that illustrate the precision as well as the ease with which quantum operations can be applied to a quantum register of stored ions: controlled-NOT operations acting on a quantum register [18], teleportation of quantum information [19], the first realisation of a quantum byte [20] and many more. The presented work illustrates recent experiments that surpass previous achievements in fidelity as well as in complexity and it also provides new insight into the nature of quantum computation.

The structure of the presented thesis is as follows: Quantum states, quantum operations, their description and properties are discussed in the following chapter. The third chapter introduces methods to infer information about a realised quantum state or operation via tomography. The fourth chapter explains changes to the apparatus in the last few years, followed by a chapter describing quantum operations that have successfully been implemented in our quantum computer. Based on these operations, the sixth chapter explains how quantum states can effectively be realised in our apparatus. In conclusion, the seventh chapter combines the presented knowledge and explains the implementation of more complex quantum algorithms.

Chapter 2

Quantum states and quantum gates

The following chapter explains how a quantum system can be described. Considering that the number of parameters to describe a system scales exponentially with the size of the system, a list of measures will be presented that allows one to describe aspects of a system using only a few numbers. Subsequently, a similar description as well as characterisation will be provided for quantum operations.

2.1 Describing a quantum system

A quantum mechanical system can be described by its density matrix ρ:

$$\rho = \sum_i p_i |\psi_i\rangle\langle\psi_i| \tag{2.1}$$

with $p_i \in \mathbb{R}_{\geq 0}, \sum_i p_i = 1$. Here, $|\psi_i\rangle$ corresponds to a pure state of the system, with p_i describing the probability of finding the quantum system in that state. In the case of a single qubit, a system consisting of the two states, $|0\rangle$ and $|1\rangle$, any pure state $|\psi\rangle$ can be written in the form:

$$|\psi\rangle = \alpha\ |0\rangle + \beta\ \exp(i\phi)\ |1\rangle, \tag{2.2}$$

with $\{\alpha, \beta, \phi\} \in \mathbb{R}$ and $\alpha^2 + \beta^2 = 1$. The term α^2 (β^2) corresponds to the probability of finding the quantum state $|\psi\rangle$ in the state $|0\rangle$ ($|1\rangle$), and ϕ represents the phase of the superposition with respect to a chosen reference. With these properties, the different $|\psi_i\rangle$ in Eq. (2.1) can be chosen to represent an ortho-normal basis of the Hilbert space $\mathcal{H}$ of the single qubit.

A quantum state can be investigated by measurements, which are described by applying Hermitian operators $\hat{M}$ to the quantum state. Of particular importance are projective or von - Neumann measurements. Here, the measurement of an observable M projects the initial quantum state onto one of the eigenstates of the operator $\hat{M}$. A Hermitian operator $\hat{M}$ can be described by

$$\hat{M} = \sum_m m P_m \tag{2.3}$$

where $P_m = |\psi_m\rangle\langle\psi_m|$ is the projector onto the eigenstate $|\psi_m\rangle$ of $\hat{M}$ with eigenvalue m. The probability $p(m)$ of observing an eigenvalue m or finding its eigenstate $|\psi_m\rangle$ is given by Born's

rule [21]

$$p(m) = \mathrm{Tr}(\rho P_m) \tag{2.4}$$

from which the expectation value $\langle \hat{M} \rangle$ for an operator $\hat{M}$ follows directly

$$\langle \hat{M} \rangle = \sum_m p(m) \cdot m = \sum_m \mathrm{Tr}(\rho P_m) \cdot m = \mathrm{Tr}(\rho M). \tag{2.5}$$

Repeatedly performing projective measurements on a set of identical quantum states results in a list of eigenvalues indicating which eigenstate of the operator has been observed. The frequencies f_m of finding the eigenstate $|\psi_m\rangle$ within N experiments are multinomially distributed. The corresponding uncertainty based on the limited number of measurements is referred to as projection noise.

Using a set of Hermitian operators $\hat{M}$ that constitutes a basis of the Hilbert space $\mathcal{H}$, it is possible to describe a quantum state in terms of expectation values for the complete set of operators. In particular, this allows for an intuitive representation of the density matrix of a single qubit via the decomposition of the density matrix in the Pauli basis. Using the Pauli matrices

$$\sigma_x = X \;= \begin{pmatrix} 0 & 1 \\ 1 & 0 \end{pmatrix}, \quad \sigma_y = Y \;= \begin{pmatrix} 0 & i \\ -i & 0 \end{pmatrix}, \quad \sigma_z = Z \;= \begin{pmatrix} 1 & 0 \\ 0 & -1 \end{pmatrix}, \tag{2.6}$$

a single-qubit density matrix can be rewritten in the form

$$\rho = \frac{1}{2}(\mathbb{1} + \vec{n} \cdot \vec{\sigma}) \text{ with } \vec{n} = \begin{pmatrix} \langle \sigma_x \rangle \\ \langle \sigma_y \rangle \\ \langle \sigma_z \rangle \end{pmatrix} \text{ and } \vec{\sigma} = \begin{pmatrix} \sigma_x \\ \sigma_y \\ \sigma_z \end{pmatrix} \tag{2.7}$$

This decomposition has a graphical representation in the Bloch sphere, depicted in Fig. 2.1. The values of the decomposition (and by that the density matrix) are equivalent to a point within the Bloch sphere and defined by its coordinates or the corresponding Bloch vector. The components of the vector correspond to projections onto the different axes, equivalent to the expectation values of the density matrix for the respective Pauli operators.

For N qubits, the total Hilbert-space $\mathcal{H}_{\mathrm{total}}$ is derived by expanding the individual single qubit Hilbert spaces $\mathcal{H}_i$ via the tensor-product[1]:

$$\mathcal{H}_{\mathrm{total}} = \bigotimes_{i=1}^{N} \mathcal{H}_i = \mathcal{H}_N \otimes \mathcal{H}_{N-1} \otimes \ldots \otimes \mathcal{H}_1 \tag{2.8}$$

A distinct feature appearing in a quantum system consisting of multiple qubits is entanglement. Here, although the complete Hilbert space is the product Hilbert space of the subsystems, the state can not be decomposed into a product of states of the respective subsystems. The terminology is as follows: A pure state $|\psi\rangle$ in the Hilbert space $\mathcal{H} = \bigotimes_{i=1}^{N} \mathcal{H}_i$ is fully separable if and only if the state can be written as a product of states of the subsystems:

$$|\psi\rangle_{\mathcal{H}} = |\psi\rangle_{\mathcal{H}_N} \otimes \ldots \otimes |\psi\rangle_{\mathcal{H}_1} \tag{2.9}$$

[1]The definition to count qubits from the right-hand side follows the computational, binary representation of numbers.

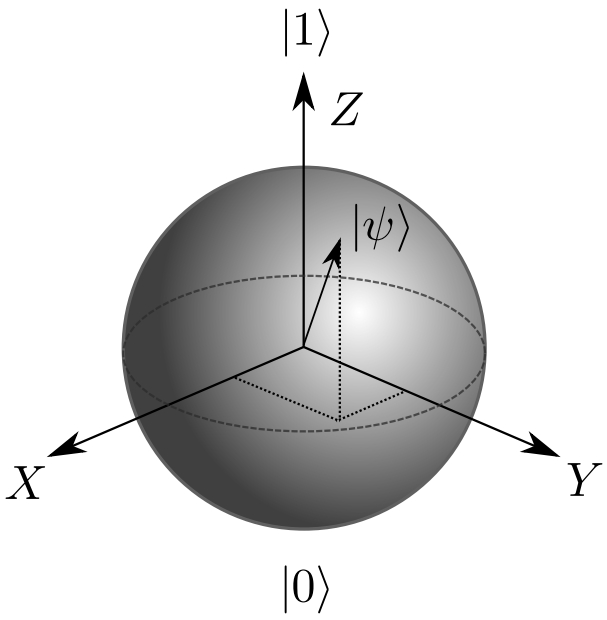

Figure 2.1: Bloch sphere of a single qubit: Any quantum state can be described by its coordinates, given by projections onto the axes {X,Y,Z} pertaining to the operators $\sigma_{\{x,y,z\}}$. A pure state would be on the surface of the sphere, whereas mixed states are closer to the centre.

If such a decomposition is not possible, the state is said to be "entangled". A violation of this condition however does not allow one to conclude full N-qubit entanglement. A state is fully (with respect to all subsystems) entangled, if and only if all bipartite partitions produce mixed reduced density matrices [22]. However, finding a quantum state to be separable in all possible bipartitions does not allow one to conclude that the state is fully separable.

Depending on the size of the Hilbert space, different classes of entangled states can be distinguished. A selection of entanglement classes is briefly introduced in the following[2]:
For a two-qubit system, entangled states can be described in terms of Bell states

$$\begin{aligned} |\phi^{\pm}\rangle &= \tfrac{1}{\sqrt{2}}(|00\rangle \pm |11\rangle) \\ |\psi^{\pm}\rangle &= \tfrac{1}{\sqrt{2}}(|01\rangle \pm |10\rangle). \end{aligned} \tag{2.10}$$

For a system of three qubits, two prominent classes of entanglement emerge: the Greenberger-Horne-Zeilinger (GHZ) states [23]

$$|\mathrm{GHZ}\rangle = \frac{1}{\sqrt{2}}(|000\rangle + |111\rangle) \tag{2.11}$$

and the class of W-states, which is a coherent superposition of quantum states described by all possible permutations of two $|0\rangle$ and a single $|1\rangle$ (or vice versa)

$$|\mathrm{W}\rangle = \frac{1}{\sqrt{3}}(|001\rangle + |010\rangle + |100\rangle) \tag{2.12}$$

[2]Commonly used and example quantum states are presented. However, the corresponding class of entangled states includes all states that are locally equivalent to the presented one - meaning all states that can be generated from the presented one using single-qubit operations only.

Interestingly it is not possible to transfer quantum states from one class to another using local operations, meaning operations that can be decomposed into operations acting on single qubits, and classical communications (LOCC) only.

For $N > 3$ qubits, a generalisation of GHZ and W states is straight-forward. W states actually belong to the class of Dicke-states. These states can be described as

$$|\mathrm{D}^m\rangle = \frac{1}{\sqrt{\binom{N}{m}}} \sum_k P_k(|0^{\otimes(N-m)}1^{\otimes m}\rangle) \tag{2.13}$$

with P_k generating all possible permutations of states consisting of m ones and $N-m$ zeros. Several other classes (such as cluster states, graph states, Werner states , ... [22]) exist but their description would exceed the scope of this work.

Properties of these classes can be significantly different under the influence of identical processes. For instance, tracing out a single qubit from a pure GHZ-state collapses the remaining state to an incoherent mixture of maximally orthogonal states. However, after removing a single qubit from a W state there is some entanglement left [24, 25]. Other properties such as the sensitivity of certain states to noise will be discussed later in the presented work.

Knowing the precise density matrix is equivalent to knowing everything about the quantum state. This allows one to answer any question with regards to the quantum state. However, the supposedly simple question whether a certain density matrix includes entanglement can be very challenging to answer - especially considering that the size of the density matrix grows exponentially with the number of qubits. Instead of providing the complete density matrix, it is often preferable to describe a quantum state using a few parameters, for example the fidelity of the generated quantum state with regards to a desired quantum state. An alternative parameter would be the distinguishability between the desired and generated quantum state. One possible problem can be already noted here - these parameters are not unique and several measures exist. In some cases, such as the fidelity, there are even different definitions that differ notably from each other.

The approach to describe complex density matrices with a few measures, however, can severely limit the precision of the conclusions that are drawn from these numbers [26]. In the following, a collection of generally employed measures will be provided, including a description of their applications as well as their shortcomings.

2.1.1 Absolute measures of quantum states

Absolute measures of a density matrix describe its properties without reference to other states. These properties ought to be independent of the chosen basis of the Hilbert space. In the following we consider a system consisting of N qubits, a corresponding Hilbert space $\mathcal{H}$ of $d = 2^N$ dimensions, and ρ describing an arbitrary density matrix of the system.

The purity $P(\rho)$ refers to the degree of mixture of a quantum state, and is a prominent absolute measure of a quantum state. A quantum state can be an uncorrelated mixture of several pure quantum states. The corresponding states and their probabilities can be obtained as eigenvalues and eigenvectors of the density-matrix. The eigenvectors are orthonormal and considering $\sum_i p_i = 1$, it is straight forward to see that

$$P(\rho) = \mathrm{Tr}(\rho^2) = \sum_i p_i^2 \leq 1. \tag{2.14}$$

Here, $P \in [\frac{1}{2^N}, 1]$ is referred to as purity, and can only be equal to 1 iff the investigated density-matrix can be described by a pure quantum state. A state with $P(\rho) = \frac{1}{2^N}$ is totally mixed.

There exist connections between the purity of a state and its separability. If the state of a two-qubit system has a purity that is below a specific value [27], namely

$$\mathrm{Tr}(\rho^2) \leq \frac{1}{2^2 - 1}, \tag{2.15}$$

then ρ is separable and therefore not entangled. This full separability criterion can be generalised for N-qubit quantum systems [28]:

$$\mathrm{Tr}(\rho^2) \leq \frac{1}{2^N - \alpha^2} \text{ with } \alpha = \frac{2^N}{\frac{17}{3}3^{N-3} + 1},\ N \geq 3. \tag{2.16}$$

Another parameter considering the "mixture" of a quantum state follows the ideas of classical thermodynamics where the classical entropy S_{class} of a system is defined as $S_{\text{class}} = -k_B \sum_i P_i \ln(P_i)$, with k_B being the Boltzmann constant and P_i describing the probability of finding the system in state i. For quantum systems an equivalent of the entropy exists in the form of the von Neumann entropy S_{vN}

$$S_{vN}(\rho) = -\mathrm{Tr}(\rho \ln(\rho)) \tag{2.17}$$

Using the approximation $\ln(\rho) \approx \rho - \mathbb{1}$ for strongly mixed states from the Mercator series (for small x: $\ln(1 + x) \approx x$), the linear entropy S_{lin} [29] is obtained which relates to the purity[3]:

$$S_{lin}(\rho) = -\mathrm{Tr}(\rho(\rho - \mathbb{1})) = -\mathrm{Tr}(\rho^2) + 1 = 1 - P(\rho) \tag{2.18}$$

Some authors [26] prefer a slightly different normalisation of the linear entropy to ensure that its quantity ranges between zero and one and is mentioned here for completeness:

$$S_{lin}(\rho) = \frac{2^N}{2^N - 1}(1 - P) \tag{2.19}$$

Describing entanglement via an absolute measure is challenging. Entanglement may be a feature between specific subsystems only; different classes of entanglement exist with distinct properties; local operations do not change the class of entanglement, requiring a non-local description. With that background, necessary conditions for all entanglement measures $E(\rho)$ [30] are:

(i) $E(\rho) = 0$ iff ρ is separable

(ii) Local unitary operations leave $E(\rho)$ invariant

(iii) $E(\rho)$ can not increase under LOCC

[3] From a resource point of view, the linear entropy is significantly easier to calculate as it does not require a decomposition of ρ into its eigenbasis.

Notwithstanding these challenging demands, there exist measures that fulfil these criteria.

A pure, entangled state $|\psi_{AB}\rangle$ of a bipartite system $\mathcal{H}_{AB}$ will collapse to a mixed state by tracing out one subsystem. With the entropy being a measure of the amount of mixture, the entropy of entanglement for a given density matrix $\rho_{AB} = |\psi_{AB}\rangle\langle\psi_{AB}|$ is defined as the von Neumann entropy of the traced subsystems:

$$\mathrm{E}_E(|\psi_{AB}\rangle) \equiv S_{vN}(\rho_A) = S_{vN}(\rho_B) \tag{2.20}$$

with $\rho_A = \mathrm{Tr}_B(\rho_{AB})$ and $\rho_B = \mathrm{Tr}_A(\rho_{AB})$. A generalisation of this expression for mixed states is given by the entanglement of formation:

$$\mathrm{E}_f(\rho) = \min_{\mathcal{E}} p_i \mathrm{E}_E(|\psi_i\rangle) \tag{2.21}$$

which minimises over all ensembles of pure states $\mathcal{E} = \{p_i, |\psi_i\rangle\}$ that fulfil $\rho = \sum_i p_i |\psi_i\rangle\langle\psi_i|$ [31].

An alternative parameter that is strongly related to the entanglement of formation is the concurrence: For a two-qubit system, consider the concurrence matrix [31]

$$R(\rho) = \sqrt{\sqrt{\rho}\,(\sigma_y \otimes \sigma_y)\,\rho^*\,(\sigma_y \otimes \sigma_y)\,\sqrt{\rho}} \tag{2.22}$$

The concurrence $\mathcal{C}$ is then defined as:

$$\mathcal{C}(\rho) = \max\{0, \lambda_1 - \lambda_2 - \lambda_3 - \lambda_4\} \tag{2.23}$$

where λ_i are the eigenvalues of the concurrence matrix $R(\rho)$ in decreasing order. Finding the concurrence to be zero corresponds to having no entanglement in the system under investigation. It is possible to directly calculate the entanglement of formation from a given concurrence [31] via

$$\mathrm{E}_f(\rho) = s\left(\frac{1 + \sqrt{1 - C(\rho)^2}}{2}\right) \tag{2.24}$$

with

$$s(x) = -x \log_2 x - (1 - x) \log_2 (1 - x). \tag{2.25}$$

Other measures such as tangle [32] exist and allow the detection of entanglement. However, many of these measures are only able to investigate bipartite systems and, with that background, are sometimes strongly related to each other. For instance, the tangle is often defined as the squared concurrence, with the concurrence being related to the entanglement of formation as described above.

Entanglement can also be investigated from a geometric point of view by asking the question, "What is the minimal distance from the state under investigation to any unentangled state?" [30] The set $\mathcal{U}$ of all unentangled states represents a convex hyperplane: fully separable states are per definition not entangled, and their incoherent mixture does not create entanglement (for a graphical representation see Fig. 2.2). From this follows that the entanglement of a density-matrix ρ can be defined as a geometric measure by:

$$E_D(\rho) = \min_{\mathcal{U}} D(\rho||\sigma) \tag{2.26}$$

where $D(\rho||\sigma)$ is a norm for the distance between the state under investigation ρ and a state σ. Here, $E_D(\rho)$ returns the smallest distance between ρ and all separable states (defined as elements σ from the set $\mathcal{U}$). However not every norm between quantum states fulfils the entanglement measure criteria defined above. One distance measure $D(\rho||\sigma)$ that leads to E_D fulfilling the entanglement measure criteria is the von-Neumann relative entropy [33], which will be introduced in the following.

2.1.2 Relative measures

Absolute measures are independent of any basis and provide the same result for locally equivalent quantum states. While this is advantageous in many cases, it is often only necessary to characterise the deviation (or distance) of a generated state relative to a desired quantum state. In this work these measures are going to be referred to as *relative measures*, with an incomplete selection of them being introduced in the following.

Initially a set of natural axioms is defined that, ideally, a relative measure $\mathcal{M}(\rho_1, \rho_2)$ between quantum states ρ_1 and ρ_2 ought to fulfil[4] [35]:

a) Normalisation: $0 \leq \mathcal{M}(\rho_1, \rho_2) \leq 1$

b) Symmetry: $\mathcal{M}(\rho_1, \rho_2) = \mathcal{M}(\rho_2, \rho_1)$

c) Convexity: $\mathcal{M}(\rho_1, a\rho_2 + (a-1)\rho_3) \geq a\mathcal{M}(\rho_1, \rho_2) + (a-1)\mathcal{M}(\rho_1, \rho_3)$

d) Multiplicativity: $\mathcal{M}(\rho_1 \otimes \rho_2, \rho_3 \otimes \rho_4) = \mathcal{M}(\rho_1, \rho_3) \cdot \mathcal{M}(\rho_2, \rho_4)$

e) Unitary invariance: $\mathcal{M}(\rho_1, \rho_2) = \mathcal{M}(U\rho_1 U^\dagger, U\rho_2 U^\dagger)$

f) Monotonicity: $\mathcal{M}(\Psi(\rho_1), \Psi(\rho_2)) \geq \mathcal{M}(\rho_1, \rho_2)$, with a quantum operation Ψ (see Sec. 2.2)

g) Definitivity: $\mathcal{M}(\rho, \rho) = 1 \; \forall \; \rho \in \mathcal{H}$

Although several measures are employed to describe how well a quantum state has been realised with regards to a desired one, the following discussion will show that only a few fulfil the above axioms.

The basis of a Hilbert space can be described as a set of orthonormal quantum states. The associated scalar product can be used as a distance measure between two states. The fidelity $\mathcal{F}$ is defined as the probability[5] of finding the desired quantum state $|\phi\rangle$ compared with the actual state $|\psi\rangle$ and directly follows Born's rule:

$$\mathcal{F}(\rho, \sigma) = \mathrm{tr}(\rho\sigma). \tag{2.27}$$

[4] Together with positivity from the normalisation criterion, definitivity and the symmetry criterion, the additional requirement of the triangle inequality would necessarily make any distance measure a metric. However, commonly used distance measures such as the fidelity are not a metric and would thus be ruled out as a distance measure [34].

[5] Some publications prefer the fidelity to be defined as the "overlap" $\langle\phi|\psi\rangle$ between quantum states, which is the square-root of the probability of observing the desired quantum state. This suggests notably better values and makes it mandatory to thoroughly check which fidelity definition is applied.

For $\rho = |\psi\rangle\langle\psi|$ and $\sigma = |\phi\rangle\langle\phi|$ being pure states, one directly obtains $\mathcal{F}(\rho, \sigma) = |\langle\phi|\psi\rangle|^2$. The extension for the case of either of the two density matrices being mixed is straight forward.

If the fidelity of a quantum state ρ is calculated with regards to itself, this fidelity definition is equivalent to the purity. From this follows, however, that the definitivity criterion is not fulfilled for mixed quantum states as the purity of a mixed state is smaller than one, while the definititivity criterion would require a fidelity of 1 of a quantum state with regards to itself - regardless of the state being pure or not. Therefore, for the remainder of this thesis, the above fidelity definition will be replaced by the Uhlmann fidelity [35, 36]

$$\mathcal{F}(\rho_1, \rho_2) = (\mathrm{Tr}(\sqrt{\sqrt{\rho_1}\rho_2\sqrt{\rho_1}}))^2 \tag{2.28}$$

which coincides with the fidelity in Eq. (2.27) (if at least one of the two quantum states is pure) but fulfils the definitivity criterion as well as all the other required criteria - as shown in Ref. 35 .

Instead of looking at the overlap between states, it is possible to investigate the distinguishability between two density matrices. Consider the following classical motivation: For a finite set of events, the ideal probability distribution p_j is expected, but q_j has been detected. The amount of information about the event is given by $-\log(q_j)$ and the total (averaged) uncertainty follows as $-\sum_j p_j \log(q_j)$. On the other hand, the uncertainty prior to any observation of p_j itself is given by $-\sum_j p_j \log(p_j)$ (also referred to as Shannon entropy). It follows that the difference $\sum_j p_j(\log(p_j) - \log(q_j)$ is a measure for the distinguishability between the two distributions defined by p_j and q_j. This measure is known as classical relative entropy. The classical relative entropy can be extended for quantum information theory as distinguishability between a density matrix ρ and a density matrix σ by

$$S(\rho||\phi) = \mathrm{Tr}(\rho \log \rho) - \mathrm{Tr}(\rho \log \phi) \tag{2.29}$$

and is called the von-Neumann relative entropy. It is important to note that this measure does not fulfil all desired properties for relative measures between quantum states, e.g. it is not symmetric $S(\rho||\phi) \neq S(\phi||\rho)$.

A distinguishability measure between quantum states that is also symmetric is provided by

$$D(\rho, \phi) = \frac{1}{2}||\rho - \phi||_{\mathrm{tr}} \tag{2.30}$$

where $||X||_{\mathrm{tr}} \equiv \mathrm{Tr}(\sqrt{X^\dagger X})$ denotes the trace norm and is equivalent to the sum of singular values of X. This measure directly corresponds to the probability of being able to distinguish between the two quantum states and is called trace distance [34]. For pure single-qubit states, the trace distance has the intuitive interpretation of half the Euclidian distance between the two quantum states on Bloch sphere. Besides being symmetric, this measure also fulfils contractivity, $D(\mathcal{E}(\rho), \mathcal{E}(\phi)) \leq D(\rho, \phi)$, in a sense that a quantum process acting on two quantum states can not increase the distinguishability between the states [34]. With respect to the tensor product, the trace distance is subadditive $D(\rho_1 \otimes \rho_2, \rho_3 \otimes \rho_4) \leq D(\rho_1, \rho_3) + D(\rho_2, \rho_4)$, whereas the fidelity is multiplicative. The trace distance also fulfils the triangle-inequality $D(\rho, \phi) \leq D(\rho, \theta) + D(\theta, \phi)$. Combined with its other properties, the trace distance therefor forms a metric[6].

[6]Metrics can be defined based on the fidelity, for instance the Bures metric $B(\sigma, \rho) = \sqrt{2 - 2\sqrt{F(\sigma, \rho)}}$ or the angle $A(\sigma, \rho) = \arccos\sqrt{F(\sigma, \rho)}$, but then the fidelity loses its original interpretation [34].

Whether a quantum state is entangled or not is a question in absolute terms which can be answered with "yes" or "no". However, because entanglement is a feature between distinct subsets of the complete Hilbert space, these subsets need to be explicitly specified. In this sense, entanglement will be referred to as a relative measure seeing that specific subsystems may be entangled "compared to" other subsystems. While it is hard to verify entanglement between several subsystems, there exists an efficient method to verify entanglement in bipartite systems: Consider a system $\mathcal{H}_{AB}$ consisting of the subsystems $\mathcal{H}_A$ and $\mathcal{H}_B$. By definition, any density matrix ρ_{AB} in system $\mathcal{H}_{AB}$ has eigenvalues $\lambda_i \geq 0$. State ρ_{AB} can be partially transposed with regards to system $\mathcal{H}_A$ using the form

$$\langle i_A, j_B|\rho^{T_A}|k_A, l_B\rangle = \langle k_A, j_B|\rho|i_A, l_B\rangle \tag{2.31}$$

with the partially transposed state referred to as ρ^{T_A}. However, in contrast to ρ_{AB}, ρ^{T_A} may show negative eigenvalues. These negative eigenvalues are a distinct feature of entanglement between subsystem $\mathcal{H}_A$ and $\mathcal{H}_B$ [37]. The sum of absolute values of negative eigenvalues

$$\mathcal{N}(\rho) = \frac{||\rho^{T_A}||_{\mathrm{tr}} - 1}{2} \tag{2.32}$$

corresponds to an entanglement criterion and is called negativity. Systems $\mathcal{H}_A$ and $\mathcal{H}_B$ are entangled, if and only if the negativity is larger than zero. In addition to being applicable to mixed states and its calculation requiring little computational overhead, this measure is also an entanglement monotone, meaning that $\mathcal{N}(\rho)$ does not increase under LOCC [37].

An alternative measure with regards to entanglement follows a geometric argument and is introduced in the following: Separable states form a convex set with a distinct border (see Fig. 2.2). The question whether a quantum state is entangled or not can be rephrased - "On which side of the border is the quantum state?" or "How far away from the entanglement border is the quantum state?" The border, and by that the distinction between entangled or fully separable quantum states, can be defined as a set of observables, or witnesses, W. For fully separable quantum states, the observables are engineered to return a positive expectation value, and negative expectation values otherwise. If at least one expectation value is found to be negative, the quantum state is entangled (but not necessarily fully entangled). In that regard, the complete set of witnesses (and by that, a complete definition of the convex set of separable quantum states) is an absolute measure for the entanglement of the quantum state. However, this figurative explanation directly shows one of the drawbacks of this approach - the number of witnesses can be very large and all of them would need to be investigated to conclude whether the quantum state is entangled or not.

In an experimental realisation, prior knowledge about the desired entangled quantum state can be used to derive a witness that specifically tests for the desired entangled quantum state. This witness, however, may fail for several other (yet still entangled) states as shown in Fig. 2.2. Here, ρ_1 is entangled, which can be detected by W_1 while W_4 may fail at detecting it. In this context, a *single* witness will be referred to as "relative measure" of entanglement (for a specific witness), while the complete set of witnesses is an "absolute measure" of entanglement.

One would hope that different measures, absolute and relative, would behave similarly. A high overlap between two states ought to result in approximately the same entanglement properties. This, however, especially in the presence of mixed states, is not the case [26]. Looking at a single parameter such as the fidelity alone, hardly allows one to draw any conclusions concerning other properties, such as the entanglement, of the system.

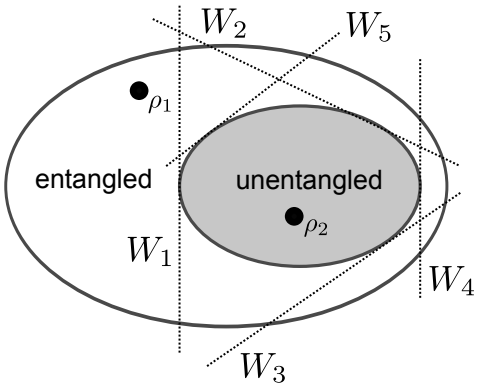

Figure 2.2: Entanglement witnesses: Unentangled states form a convex set. Defining intersections through the Hilbert space $\mathcal{H}$ with witnesses W_i, it is possible to completely define the border of the convex set. ρ_1 will return negative expectation values for W_1 and W_5 and positive expectation values for witnesses W_2, W_3 and W_5. Nevertheless finding at least one negative expectation values is sufficient to prove entanglement in the quantum state ρ_1. In contrast to ρ_1, ρ_2 will provide positive expectation values for all witnesses.

2.2 Quantum operations

For quantum information processing we consider a Hilbert space $\mathcal{H}$ and unitary operations U that map a quantum state $|\psi\rangle$ onto another state $|\psi'\rangle$

$$\begin{aligned} &U : \mathcal{H} \to \mathcal{H} \\ &\psi \mapsto \psi' = U|\psi\rangle. \end{aligned} \tag{2.33}$$

These unitary processes are reversible. In general, however, real implementations of quantum information processing are prone to errors and the operations are not necessarily unitary. A description that is able to take non-unitary processes into account is provided by the operator-sum representation [29]:

$$\rho_{\text{out}} = \mathcal{E}(\rho_{\text{in}}) = \sum_i E_i \, \rho_{\text{in}} \, E_i^\dagger \tag{2.34}$$

Here, the process $\mathcal{E}$ acts on the input quantum state ρ_{in} and returns the output state ρ_{out}. The process is decomposed into a set of operators E_i. The drawback of such a description for a quantum process is that it is not unique, meaning that the very same process can be decomposed into several different sets of operators.

Mathematically equivalent to Eq. (2.34) is

$$\rho_{\text{out}} = \mathcal{E}(\rho_{\text{in}}) = \sum_i E_i \, \rho_{\text{in}} \, E_i^\dagger = \sum_{i,j} \chi_{i,j} \, A_i \, \rho_{\text{in}} \, A_j^\dagger \tag{2.35}$$

where the operators A_i represent an orthogonal set (for instance the Pauli operators). Choosing a fixed basis of operators A_i, the description of a process via its χ-matrix becomes unique, in contrast to a decomposition into operators E_i [34].

χ matrices have similar properties to density matrices, yet their interpretation requires careful considerations: For a density matrix, finding only a single non-zero eigenvalue is equivalent to the statement that the quantum state is pure. If more than one non-zero eigenvalue is found,

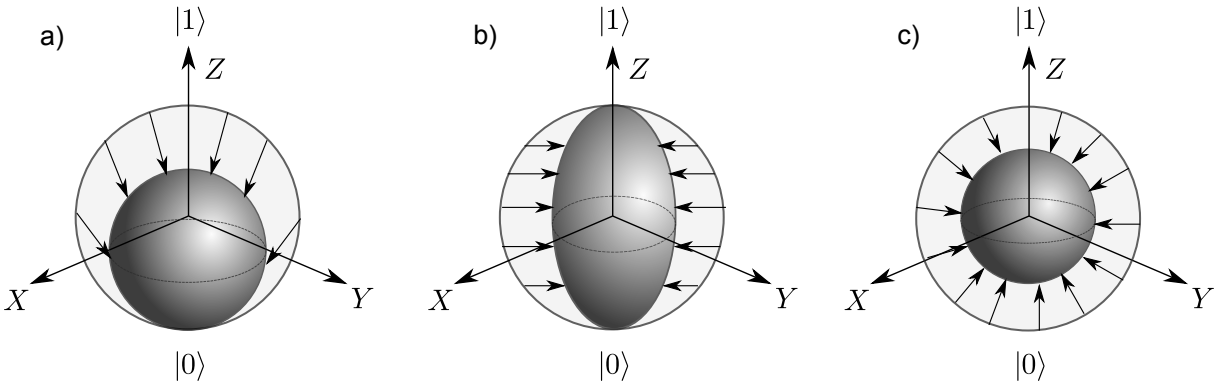

Figure 2.3: Quantum channels acting on a single qubit: a) Amplitude damping, like spontaneous decay acting on a atom, results in the Bloch sphere shrinking towards the ground state; b) Dephasing is equivalent to a loss of phase information and contracts the Bloch sphere around its corresponding Z axis; c) Depolarizing channel acting on a single qubit can also be interpreted as, with some probability, exchanging the qubit with a completely mixed state, which is equivalent to the Bloch sphere shrinking towards the completely mixed state.

the state is mixed and therefore has more entropy. In a similar way an entropy measure may be applicable for processes. If a χ matrix exhibits only a single non-zero eigenvalue, the process can be represented by a unitary operation and the purity of any input state remains unchanged during the process. Now consider a non-unitary process described by the following operator-sum-representation:

$$\rho_{\text{out}} = E_0 \, \rho_{\text{in}} \, E_0 + E_1 \, \rho_{\text{in}} \, E_1 \tag{2.36}$$

with

$$E_0 = \begin{pmatrix} 1 & 0 \\ 0 & \sqrt{1-p} \end{pmatrix} \; E_1 = \begin{pmatrix} 0 & \sqrt{p} \\ 0 & 0 \end{pmatrix}. \tag{2.37}$$

This process is referred to as amplitude damping [29] and describes, for instance, spontaneous decay acting on an atomic qubit. Here, p is the damping parameter and corresponds to the decay probability. A graphical representation of this process acting on a single qubit is shown in Fig. 2.3 a). While this process is not unitary, complete amplitude damping maps any state into a pure quantum state (the ground state of the system) and, as a cooling or state initialisation process, effectively removes entropy from the system. From this follows that a non-unitary process does not necessarily add entropy to the system.

Another prominent example for a non-unitary process is dephasing or phase damping [29]: The phase information of a qubit is gradually lost, which can be rewritten as a phase bit-flip acting on the qubit with a certain probability p:

$$\mathcal{E}(\rho) = (1-p) \, \rho + p \, Z \, \rho \, Z. \tag{2.38}$$

For a probability of $p = 0.5$, all phase information of the qubit is lost. A visualisation of this process acting on the Bloch sphere of a qubit is presented in Fig. 2.3 b): dephasing effectively shrinks the Bloch sphere around the corresponding Z-axis of the qubit.

A similar, homogeneous effect along all principal axis of the Bloch sphere is called depolarisation [29]: instead of shrinking the Bloch sphere only along the Z axis, depolarisation

shrinks the Bloch-sphere homogeneously towards the completely mixed state. This process is can therefore be represented by

$$\mathcal{E}(\rho) = (1-p)\,\rho + p\,\mathbb{1}/2 \tag{2.39}$$

which, using $\frac{\mathbb{1}}{2} = \frac{\rho + X\,\rho\,X + Y\,\rho\,Y + Z\,\rho\,Z}{4}$, is equivalent to [29]

$$\mathcal{E}(\rho) = (1 - \frac{3p}{4})\,\rho + \frac{p}{4}\,(X\,\rho\,X + Y\,\rho\,Y + Z\,\rho\,Z) \tag{2.40}$$

and is graphically illustrated in Fig. 2.3 c).

Quantifying a process with regards to other processes requires a distance measure that is able to effectively distinguish between processes. A distance measure Δ between quantum processes $\mathcal{E}$ and $\mathcal{F}$ ought to fulfil the following criteria [34]:

(a) Metric: Δ should fulfil three metric properties: (i) $\Delta(\mathcal{E},\mathcal{F}) \geq 0$ with $\Delta(\mathcal{E},\mathcal{F}) = 0$ iff $\mathcal{E} = \mathcal{F}$; (ii) Symmetry: $\Delta(\mathcal{E},\mathcal{F}) = \Delta(\mathcal{F},\mathcal{E})$; and (iii) triangle inequality $\Delta(\mathcal{E},\mathcal{G}) \leq \Delta(\mathcal{E},\mathcal{F}) + \Delta(\mathcal{F},\mathcal{G})$

(b) It should be easy to calculate.

(c) There should be a clear and experimentally accessible procedure to determine the value of Δ.

(d) A physical interpretation should be well motivated.

(e) Stability: Attaching an ancilla system $\mathcal{H}_a$ to the investigated system $\mathcal{H}_s$ without performing any operation on $\mathcal{H}_a$ should not affect the distance in system $\mathcal{H}_s$: $\Delta(\mathbb{1}_a \otimes \mathcal{E}, \mathbb{1}_a \otimes \mathcal{F}) = \Delta(\mathcal{E},\mathcal{F})$, where $\mathbb{1}_a$ represents the identity operation on the ancilla system $\mathcal{H}_a$.

f) Chaining: $\Delta(\mathcal{E}_2 \circ \mathcal{E}_1, \mathcal{F}_2 \circ \mathcal{F}_1) \leq \Delta(\mathcal{E}_1,\mathcal{F}_1) + \Delta(\mathcal{E}_2,\mathcal{F}_2)$. Thus for a process composed of many smaller steps, the total error will be equal to or smaller than the sum of the individual errors.

The process fidelity $\mathcal{F}_{\text{proc}}$ between two processes $\mathcal{E}$ and $\mathcal{F}$ (and their respective descriptions via the χ matrices $\chi_\mathcal{E}$, $\chi_\mathcal{F}$) is often defined in a similar way as the fidelity between quantum states (see Eq. (2.27)) via

$$\mathcal{F}_{\text{proc}}(\chi_\mathcal{E}, \chi_\mathcal{F}) = \text{tr}(\chi_\mathcal{E}\,\chi_\mathcal{F}) \tag{2.41}$$

However, the process fidelity does not fulfil the metric criterion: for non-unitary processes described by $\chi_\mathcal{G}$ (with more than one eigenvalue being non-zero) $\mathcal{F}_{\text{proc}}(\chi_\mathcal{G}, \chi_\mathcal{G}) < 1$, in the very same way that the fidelity definition in Eq. (2.27) does not return 1 for the fidelity of a mixed quantum state with itself. In principle, the requirements for process distance measures mentioned above strongly overlap with previously discussed requirements for distance measures between density matrices [35]. From that point of view it may be beneficial to find a map from quantum processes to (higher dimensional) quantum states. Distance measures initially derived for quantum states would then be directly applicable to quantum processes via their density matrix equivalents. This map, from a quantum process to a higher-dimensional density matrix,

is possible via the Choi-Jamiolkowski (CJ) isomorphism [38, 39]. It maps any process $\mathcal{E}$ to a unique higher-dimensional density matrix $\rho_{\mathcal{E}}$. The effective system size of the CJ matrices is twice the number of qubits of the described processes. This can be seen by looking at a single qubit: A qubit has two dimensions, but the corresponding operator space is defined by 4 operators (for instance: identity and the 3 Pauli operators) - dimensionally equivalent to the 2 qubits. A physical interpretation of the Choi-Jamiolkowski isomorphism is the following: Consider a system $\mathcal{H}_a$ consisting of N qubits. Complement the complete system $\mathcal{H}_{ab}$ by adding another system $\mathcal{H}_b$ of again N qubits. As a next step, create a maximally entangled state between systems $\mathcal{H}_a$ and $\mathcal{H}_b$. The process $\mathcal{E} \otimes \mathbb{1}_b$ acting on system $\mathcal{H}_{ab}$ will return a quantum state $\rho_{\mathcal{E}} \in \mathcal{H}_{ab}$ that completely describes the process $\mathcal{E}$.

The Choi-Jamiolkowski isomorphism maps quantum processes onto quantum states. With regards to distance measures between processes, distance measures between quantum states are now applicable. The Uhlmann fidelity (see Eq. (2.28)) can now be employed as a distance measure between processes $\mathcal{E}$ and $\mathcal{F}$ via their respective CJ matrices $\rho_{\mathcal{E}}$, $\rho_{\mathcal{F}}$. Here, the application of the Uhlmann fidelity on CJ matrices $\mathcal{F}_{\mathrm{CJ}}$

$$\mathcal{F}_{\mathrm{CJ}}(\mathcal{E}, \mathcal{F}) = (\mathrm{Tr}(\sqrt{\sqrt{\rho_{\mathcal{E}}}\rho_{\mathcal{F}}\sqrt{\rho_{\mathcal{E}}}}))^2 \tag{2.42}$$

fulfils all the requirements for quantum process distance measures. The same applies for the trace distance (see Eq. (2.30)) when applied to CJ matrices - referred to as D_{CJ}:

$$D_{\mathrm{CJ}}(\mathcal{E}, \mathcal{F}) = \frac{1}{2}||\rho_{\mathcal{E}} - \rho_{\mathcal{F}}||_{\mathrm{tr}} \tag{2.43}$$

Both measures, $\mathcal{F}_{\mathrm{CJ}}$ and D_{CJ}, can be interpreted as average performance of the investigated quantum process with regards to a desired process [34].

The average performance, or so-called mean process fidelity $\bar{\mathcal{F}}_{\mathrm{proc}}$, of a quantum process $\mathcal{E}_{\mathrm{exp}}$ with respect to a desired process $\mathcal{E}_{\mathrm{ideal}}$ can also be obtained directly

$$\bar{\mathcal{F}}_{\mathrm{proc}}(\mathcal{E}_{\mathrm{ideal}}, \mathcal{E}_{\mathrm{exp}}) = \underset{\rho_{\mathrm{in}}}{\mathrm{mean}}\, \mathcal{F}(\mathcal{E}_{\mathrm{ideal}}(\rho_{\mathrm{in}}), \mathcal{E}_{\mathrm{exp}}(\rho_{\mathrm{in}})) \tag{2.44}$$

and describes the mean overlap of the predicted output state with the ideally expected output state averaged over a sample of states ρ_{in}. This measure, however, only fulfils the metric and chaining criteria for quantum processes [34]. Usually pure quantum states are randomly chosen according to the Haar measure [40] and applied for mean process fidelities. Interestingly the mean process fidelity based on Haar-measure distributed quantum states for a desired unitary process is directly linked to the process fidelity via [41]

$$\bar{\mathcal{F}}_{\mathrm{proc}} = \frac{d\, F_{proc} + 1}{d + 1} \tag{2.45}$$

with $d = 2^N$ being the number of dimensions in the N-qubit system. This allows to map between mean process fidelity and process fidelity without the intense numerical overhead of calculating the average performance.

However, if the idea behind the mean process fidelity is to provide a number for the mean fidelity of the output states obtained with respect to the output states expected, it is not clear why Haar-measure distributed quantum states are preferable to other distributions. Alternative distributions of quantum states show different distributions with regards to eigenvalues,

$\mathcal{F}_{\text{proc}}$	Haar measure $\bar{\mathcal{F}}_{\text{proc}}$	Hilbert-Schmidt $\bar{\mathcal{F}}_{\text{proc}}$	traced subsystem $\bar{\mathcal{F}}_{\text{proc}}$ ($\text{Tr}_2(4 \text{ x } 2)$)
0.81	84.8(30)	97.1(14)	89.6(24)

Table 2.1: The description of a quantum channel of two qubits as described in Eq. (2.46) compared to an ideal quantum channel describing the unity process. The process fidelity $\mathcal{F}_{\text{proc}}$ of 81% is compared to the mean process fidelity $\bar{\mathcal{F}}_{\text{proc}}$ for different distributions of quantum states as defined in Ref. [40]: Haar measure- pure states equally distributed according to the Haar measures. The mean fidelity could also be obtained via Eq. (2.45); Hilbert-Schmidt - randomly drawn density matrices according to the Hilbert-Schmidt distribution; traced subsystem: $\text{Tr}_2(n \text{ x } 2)$ - density matrices obtained by creating pure states in a $\mathcal{H}_{n\otimes 2}$ Hilbert space, followed by tracing out the 2-dimensional subspace. In each case 10^6 density matrices have been randomly drawn.

entanglement, purity and other parameters. It is therefore clear that the informative value of parameters such as the mean process fidelity is limited and depends strongly on the distribution employed. Randomly chosen density matrices with higher probabilities of including mixed states, for instance from a Hilbert-Schmidt distribution [40], result in apparently higher process fidelities as the overlap between mixed states is usually higher than for pure states. For an example look at the following investigation.

Consider a process with a 10% probability to flip the phase of one qubit, acting independently on the two qubits in the system. The two-qubit process can be described by

$$\begin{aligned}\mathcal{E}(\rho) = \quad & 0.81\ \mathbb{1}\ \rho\ \mathbb{1} \\ & +0.09\ \sigma_z^{(1)}\ \rho\ \sigma_z^{(1)} \\ & +0.09\ \sigma_z^{(2)}\ \rho\ \sigma_z^{(2)} \\ & +0.01\ \sigma_z^{(1)} \cdot \sigma_z^{(2)}\ \rho\ \sigma_z^{(1)} \cdot \sigma_z^{(2)}\end{aligned} \tag{2.46}$$

with $\sigma_z^{(i)}$ describing the phase bit-flip on qubit i. An investigation via a mean process fidelity for different distributions of quantum states is presented in Tab. 2.1. The mean process fidelity, for the very same process, is between 85% and 97%, solely depending on the chosen distribution - while by looking at the operator representation the identity operation is only present in 81% of the realisations. With that knowledge, one might want to refrain from using the mean process fidelity to describe how well a desired quantum process has been implemented.

While the mean process fidelity only fulfils the metric and chaining criteria for quantum processes, a worst-case investigation of an implemented process with regards to a desired one can fulfil all criteria for process distance measures. One of the motivations behind a worst-case investigation is given by the Grover search algorithm [11]: for finding a specific entry in an unsorted database one might be less interested in the average performance of the process compared to the worst-case performance – a direct measure for the trust that one can put into any returned result.

Following a convex optimisation, one obtains the worst distance for a pure input state $|\psi\rangle$ between an implemented process $\mathcal{E}$ and the desired process $\mathcal{F}$. For the Uhlmann fidelity this can be rewritten as

$$F_{\text{CJ}}^{\min} = \min_{|\psi\rangle} F(\mathcal{E}(|\psi\rangle), \mathcal{F}(|\psi\rangle)) \tag{2.47}$$

whereas for the trace distance it is

$$D_{\mathrm{CJ}}^{\max} = \max_{|\psi\rangle} D(\mathcal{E}(|\psi\rangle), \mathcal{F}(|\psi\rangle)) \tag{2.48}$$

Additional work allows these measures to be stable (process distance criteria (e)), fulfilling all criteria for process distance measures [34].

To conclude, this chapter has briefly introduced the description of quantum states and quantum processes. Different measures have been presented, with the Uhlmann fidelity and trace distance being especially suited to compare density matrices as well as quantum processes. This, however, requires an already-present description of quantum states (quantum processes) via a density matrices (χ matrices). The following chapter will explain how such a description can be obtained via state tomography (process tomography).

Chapter 3

Quantifying quantum states and processes

Quantum states and processes can be described by their respective density or χ matrix. Any characterisation therefore requires an experimental procedure to obtain these matrices. With respect to the exponentially growing parameter space these characterisations, however, are experimentally highly demanding. The following chapter will explain the origin of these challenges in detail as well as present possible solutions.

3.1 State tomography

In the following, different means will be introduced to determine the quantum state of a system, provided that several copies of the same quantum state are available. This differs slightly from the verification of a specific quantum state as no initial information about the system is required or assumed. In that sense the methods discussed can be regarded as a "black box" investigation of a quantum system which requires more resources than the verification of a specific state. Here, a simple verification may be performed up to exponentially faster than a full tomography [42–44].

The basic idea behind quantum state tomography was shown in Eq. (2.7): Any quantum state can be decomposed into a set of operators and their respective expectation values. Vice versa, measuring these expectation values allows one to infer the investigated quantum state. The only requirement is that the set of quantum operators forms a basis of the Hilbert-space. In the following, the set of operators is represented by the local Pauli-product-basis of the Hilbert-space. Focusing on trapped ions, all operations are assumed to be trace-preserving[1]. In addition, the detection method ought to allow one to distinguish between the different projectors into the eigenstates of the considered observables. For our particular case, observables $\mathcal{O}^i$ are chosen to be $\mathcal{O}^i \in \{\sigma_z, \sigma_x, \sigma_y\}$ with the corresponding projectors $\{(|0\rangle\langle 0|, |1\rangle\langle 1|), (|+_x\rangle\langle +_x|, |-_x\rangle\langle -_x|), (|+_y\rangle\langle +_y|, |-_y\rangle\langle -_y|)\}$. For a given number of experiments per setting, single-qubit state tomography returns a table as presented in Tab. 3.1.

Being able to distinguish the individual projectors (in contrast to only measuring the expectation values), state tomography of an N-qubit quantum state requires all possible permutations of $\prod_{i,j,\ldots} \mathcal{O}^i\mathcal{O}^j \ldots$ with $\mathcal{O}^i \in \{\sigma_z^{(i)}, \sigma_x^{(i)}, \sigma_y^{(i)}\}$ observables, resulting in 3^N measurement set-

[1] Storage times of ion-qubits are usually on the order of days while losing a single ion is easily detected. Should an ion be lost, the complete experimental data set (potentially several hour's of measurements) is discarded.

	P_1	P_2
σ_z	0	1
σ_x	0.5	0.5
σ_y	0.5	0.5

Table 3.1: Sample data of a single-qubit state tomography: Performing a projective measurement in the eigenstates of σ_z of P_1=$|0\rangle\langle 0|$ and P_2=$|1\rangle\langle 1|$ yield the information that the output state was always found in state $|1\rangle\langle 1|$. This directly allows to claim that the investigated state is (with high probability) an eigenstate of σ_z. Measurements along $\sigma_{\{x,y\}}$ (via the respective projectors $P_{(1,2)} = (|+_x\rangle\langle +_x|, |-_x\rangle\langle -_x|)$ and $P_{(1,2)} = (|+_y\rangle\langle +_y|, |-_y\rangle\langle -_y|)$ confirm conclusions taken from the measurement along σ_z: for each of the two measurement basis x,y the corresponding projectors are found with equal probability which can be interpreted as "The investigated quantum state is not an eigenstate of the measurement". This becomes also clear from a mathematical argument - if the two projectors show up with equal probability, the expectation value of the measurement is zero and therefore does not contribute in a linear reconstruction of the quantum state.

tings. Although this measurement basis is local (indicated by $\prod$ rather than $\bigotimes$) the projectors nevertheless form a basis of the complete Hilbert-space and are therefore sufficient for complete state tomography. In that respect, the local observations and classical communication nevertheless allow one to infer non-local entanglement in the system. This is illustrated by a two-qubit measurement of $\langle\sigma_z^{(2)}\rangle\langle\sigma_z^{(1)}\rangle$: the corresponding projectors for this measurement are $\{|00\rangle\langle 00|, |01\rangle\langle 01|, |10\rangle\langle 10|, |11\rangle\langle 11|\}$ from which the observables $\langle\mathbb{1}\mathbb{1}\rangle, \langle\mathbb{1}\sigma_z\rangle, \langle\sigma_z\mathbb{1}\rangle, \langle\sigma_z\sigma_z\rangle$ can be inferred. Extended to the complete set of measurements, a basis of the Hilbert-space (here in terms of Pauli operators) can be formed.

3.1.1 Linear reconstruction

The quantum state of a single qubit can be estimated by measuring the projectors of the eigenstates of $\sigma_{\{x,y,z\}}$ followed by a linear reconstruction of the quantum state given by the chosen basis:

$$\rho_{\text{lin}} = \frac{1}{2}(\mathbb{1} + \langle\sigma_x\rangle\sigma_x + \langle\sigma_y\rangle\sigma_y + \langle\sigma_z\rangle\sigma_z). \tag{3.1}$$

This can directly be extended to multiple qubits. While this equation is mathematically correct, an experiment will not be able to determine a quantum state with absolute precision from this procedure. Even without any experimental imperfections, precise determination of the expectation value of any observable (or the probability of detecting a certain eigenstate) requires an infinite number of measurements. Therefore expectation values and their errors can only be estimated. Consider N experiments taken for a particular setting, for example investigating σ_x, and finding the projector P_i f_i times. Then the probability $p_i = f_i/N$ is known with an uncertainty Δp_i of

$$\Delta p_i = \sqrt{\frac{p_i(1-p_i)}{N}}. \tag{3.2}$$

With these error bars of the individual measurements and quantum state reconstruction in mind, new raw data can be simulated following the ideas of a Monte-Carlo simulation, each resulting in a new density matrix. Within the error bars of the measurements, all these density matrices

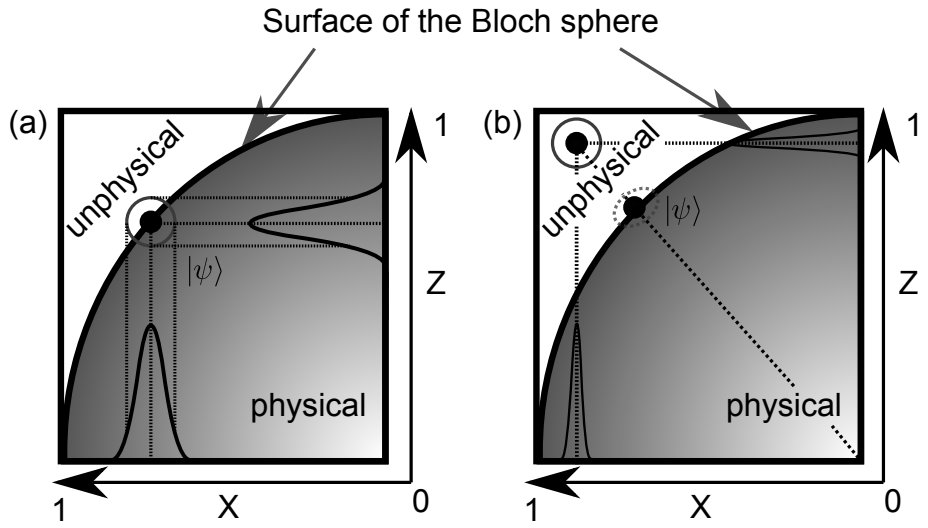

Figure 3.1: The effect of projection noise and imperfect experimental control an quantum state tomography depicted on the projection of the Bloch sphere: The quantum state of a qubit is, in its Bloch vector representation, confined to a point within the Bloch sphere. The coordinates of that point are equivalent to the expectation values of $\sigma_{(x,y,z)}$. (a) Due to insufficient sampling and experimental errors, tomography performed on a single-qubit pure quantum state (located on the surface of the Bloch sphere) may return data that, while each data point is valid on its own, in their completeness suggests a non-physical quantum state outside the Bloch sphere. (b) Restricting quantum state reconstructions to physical density matrices may return quantum states without proximity to the actual data.

are equally likely with regards to the original raw data. Given such a list of equivalent density matrices, mean values and standard deviations for any measure can be calculated.

Performing such an investigation on the raw data to infer error bars on different quantities is, however, limited. The Monte-Carlo simulation assumes the different probabilities p_i to be a statistical mean value. An actual tomography with a finite number of measurements can only provide the frequency f_j out of N measurements that projector P_j has been observed. For example, if the tomography yields the information that P_j has not been observed, this will be interpreted as a probability of $p_j = 0$. The description of discrete measurement results follows a multinomial distribution and leads to an error $\Delta p_j = 0$. This statement is equivalent to absolute knowledge about the quantum state with respect to a specific projector, meaning that the eigenstate of the projector P_j will never ever be observed. Such a claim can, however, not be made from a statistical point of view. Assume that an experiment yields d different outcomes o_i. The experiment is repeated N times and one is asked to determine the probability and its error of detecting outcome o_i. The minimal error for each probability is $\frac{1}{N+d}$, following Laplace's law of succession [45]. It is not clear how this issue ought to be taken into account for Monte-Carlo simulations. In the following, numbers derived from tomographies based on Monte-Carlo simulations will therefore have the percentage of presumably "error-less" raw data (where pseudo-probabilities equal to zero or one have been stored) attached as a hint on the validity of the error bars. A solution to this problem is to drop the assumption that finding a certain result f times within N experiments equals to a pseudo-probability $p = f/N$. One possible state reconstruction that takes both the frequencies f_i as well as the number of experiments N into account will be presented in this section.

Besides the validity of the error bars obtained, there exists another problem: a density matrix obtained from a linear reconstruction may not necessarily be physical. Especially pure states may, due to projection noise, indicate density matrices with negative eigenvalues or even $\mathrm{Tr}(\rho^2) > 1$. An intuitive picture is presented in Fig. 3.1 a): A pure single-qubit quantum state is located on the surface of the Bloch sphere. The derivation of the expectation values of $\sigma_{(x,y,z)}$ with a finite number of measurements is prone to errors and may therefore, combined in the reconstruction, return a quantum state that is (within the error bars of the individual measurements) located outside the Bloch sphere and by that, the physical space of single-qubit quantum states. One solution [46] to this problem is to calculate the spectral decomposition of the density matrix and set all negative eigenvalues to zero, followed by a renormalisation of the density matrix. For sufficiently good statistics on the raw data, this protocol allows one to perform numerically fast quantum state tomographies that yield physical density matrices. A similar procedure is currently investigated by Smolin et al. [47]: after a numerically linear reconstruction, negative eigenvalues will be redistributed in a specific way. Here, Smolin and coworkers show that this method is related to a least-squares optimisation yet is significantly more efficient. Their investigations show that this method is able to infer 8-qubit density matrices in less than 10 seconds.

3.1.2 Maximum likelihood reconstruction

In light of possible unphysical predictions from a straight-forward linear reconstruction a maximum-likelihood approach of physical quantum states with regards to the measured data appears appealing. In contrast to a linear reconstruction, the constraints on a physical density matrix are directly implemented in the evaluation:

$$\rho = \arg\max_{\rho}\{\mathcal{L}(\rho, X) \mid \rho \geq 0\} \tag{3.3}$$

Here $\mathcal{L}$ is a measure for the likelihood of ρ generating the observed data X, restricted to semi-positive density matrices. Renormalisation can be performed later on. Error estimates can be performed via Monte-Carlo simulations as described above. Whether the predictions are statistically sound remains questionable in light of the restriction that the above maximum-likelihood reconstruction will always return physical density matrices - even if the data may not support that claim. The following pages will discuss these mathematical and statistical challenges in more detail.

The physical realisation of quantum state tomography is limited by several aspects: a limited number of measurement time directly corresponds to limited knowledge. Even without any experimental errors, statistical errors - or so-called projection noise - based on a limited number of measurements is expected to affect the tomography. Here, projection noise becomes larger when the investigated quantum state is not an eigenstate of one of the applied observables. In this sense, prior knowledge about the investigated process may be applied to find a suitable basis to investigate the state. If this knowledge is not available, sometimes referred to as “black box tomography”, the mean performance of the tomography may degrade significantly. The effect of the measurement basis with respect to the investigated density matrix as well as on the projection noise is presented in Fig. 3.2: Tomography is performed on the principal axis $\sigma_{(x,y,z)}$ for quantum states of the form $\frac{1}{\sqrt{2}}(|0\rangle + \exp(i\phi)|1\rangle)$. For different ϕ, tomographies

are simulated and the quantum state is reconstructed using an iterative, maximum-likelihood method [48] commonly used in Innsbruck. As a measure for the overlap between reconstructed and original quantum state, the Uhlmann fidelity is employed. Measurements that happen to include eigenstates of the investigated density matrix are notably less prone to projection noise and result in high-fidelity predictions. However, if the chosen set of observables/projectors shows no strong overlap with the density matrix, the evaluation shows large fluctuations in the predicted quantum state with respect to the original state. Even though the density matrix and its analysis is performed without errors, projection noise from 100 experiments per setting are sufficient to result in an apparent average loss of fidelity of about 2% with a standard deviation of 2%. If average errors solely due to projection noise are desired to be smaller than 1% then at least 1000 measurements per setting ought to be performed.

Other estimations for the density matrix can be based on weighted least-square fitting such as

$$\rho = \arg\min_{\rho}\{\parallel \epsilon(\rho, X) \parallel_w^2 \mid \rho \geq 0\} \tag{3.4}$$

with $\parallel \epsilon(\rho, X) \parallel_w^2 = \sum_i \frac{(\mathrm{tr}(P_i\rho)-p_i)^2}{\sigma_i^2}$ and σ_i describing the error of each measurement setting i. Here it should be noted that least-squares fits are only applicable for parameter estimations where noise on the obtained data is dominated by Gaussian noise (for a brief introduction see Ref. 47). Depending on the experimental setup, this requirement may, or may not, be fulfilled. Such an approach, based on the number of parameters, is computationally demanding. A notably better approach, if warranted, is to allow the algorithm to optimise for presumably low rank density matrices [49]. In this "compressed sensing" technique, an additional term will put weight onto low-rank matrices provided by the term γ , effectively allowing for an exponential decrease in the number of necessary measurements:

$$\rho = \arg\min_{\rho}\{\gamma \parallel \rho \parallel_{\mathrm{tr}} + \parallel \epsilon(\rho, X) \parallel_2 \mid \rho \geq 0\} \tag{3.5}$$

In this procedure, the optimisation routine does not require normalisation of the quantum state right away, which will be done as a follow-up step. Minimising $\parallel \rho \parallel_{\mathrm{tr}} = \sum_i \lambda_i$ effectively removes small eigenvalues of the density matrix ρ - resulting in a density matrix that can effectively be described by a sparse matrix. Ongoing investigations show that this approach is able to infer density matrices from eight-qubit state tomography within a few minutes [50], notably faster than the iterative method [48] currently employed in Innsbruck.

The drawback of such restricted reconstructions is that the evaluation does not indicate whether the raw data used makes any physical sense. Consider the following example of raw data that, deliberately, is not physical: For state tomography a single qubit is investigated on the principal $\sigma_{(x,y,z)}$ axis. The measurement along the x axis always returned state $|+_x\rangle$, the measurement along the y axis always returned $|+_y\rangle$ while the measurement along z axis always returned $|0\rangle$. Each measurement on its own could directly be interpreted as "The quantum state has been found with high probability. It is $|+_x\rangle$ (or $|+_y\rangle$ or $|0\rangle$). In principle no further measurements are required." However, the three measurements contradict each other: Each measurement implies that the quantum state is an eigenstate of the measurement, but there is no physical quantum state that can be an eigenstate of all three measurements. An illustration of this example is shown in Fig. 3.1 (b). Although a separate investigation of the raw data may indicate that the complete set of data corresponds to a strongly non-physical quantum state (for

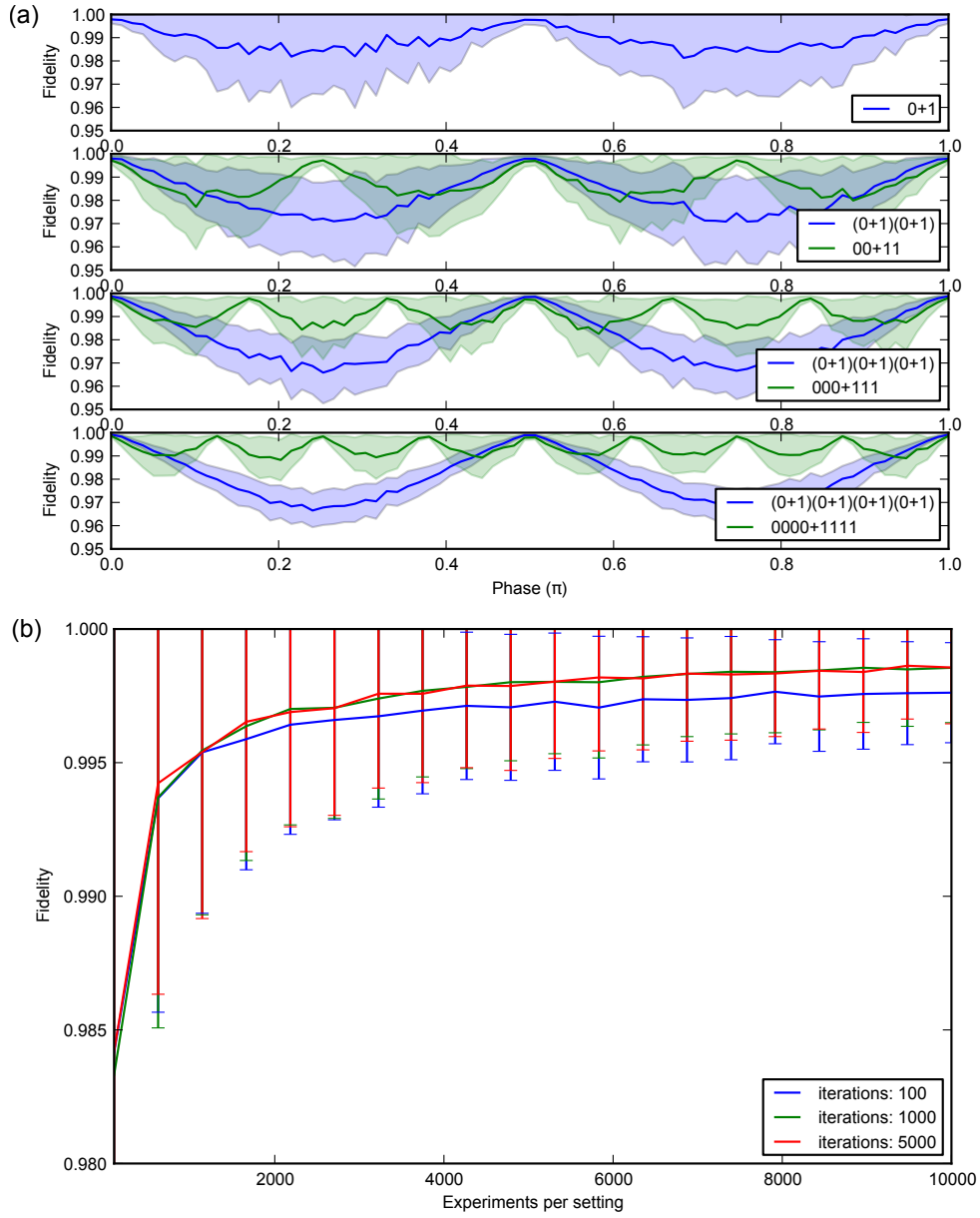

Figure 3.2: Monte-Carlo simulation of state reconstruction: (a) State tomography is sensitive to the chosen observables with respect to the investigated quantum state. Here, quantum states of the form $\frac{1}{\sqrt{2}}(|0\rangle + \exp(i\phi)|1\rangle)$ (and equivalents) were subjected to state tomography for a varying phase ϕ. If the quantum state is an eigenstate of the principal axis of the tomography (in this case σ_x or σ_y), reconstruction yields the quantum state with almost perfect fidelity. For quantum states that are not eigenstates projection noise starts to influence the derived fidelities. Simulations indicate that projection noise based on 100 experiments per setting results in an apparent loss of fidelity of up to 3%. GHZ states show a similar behaviour with slightly less sensitivity due to fewer states appearing during the investigation. Mean values and standard deviations have been derived from 100 Monte-Carlo simulations each using the iterative state reconstruction [48] and performing 1000 steps each. (b) The single-qubit quantum state $\frac{1}{\sqrt{2}}(|0\rangle + \exp(i\pi/4)|1\rangle)$ is sensitive to projection noise (see (a)). The simulations suggest that on the order of 1000 experiments per setting are required if fidelities in the 99% regime are to be investigated. In addition, the number of steps in the iterative state reconstruction [48] should be on the order of 1000 to ensure that the most-likely quantum state has been reached. Mean values and standard deviations of the Uhlmann-fidelity have been derived from 100 Monte-Carlo simulations each.

instance by a linear reconstruction and a subsequent investigation of the negative eigenvalues), a maximum-likelihood reconstruction with constraints to physical density matrices will hint at a pure density matrix. The problem whether the obtained data is consistent with a physical density matrix is not addressed by any of these reconstruction methods. One detailed investigation of state tomography where a detailed analysis of the raw data indicated a flaw in an experimental setup can be found in Ref. 51. Therefore additional investigations concerning the question of whether the obtained data is physical (in a sense that within the error estimations it supports a matrix with non-negative eigenvalues and their sum being equal to one) are recommended.

A maximum likelihood reconstruction is able to deal with projection noise close to the border of physical and unphysical density matrices. While this is an advantage compared to the linear reconstruction, obtaining a density matrix of rank 1, a pure state, represents a statistical problem on its own. Stating that an experimentally realised quantum state is pure is equivalent to saying that one and only one quantum state has been created - with a probability of 100% and no error. Besides experimental imperfections, such a claim is not possible with a finite set of measurements. Inferring a quantum state from a limited number of measurements does not warrant one to fully exclude certain states. This results in the statistical requirement that state tomography of any quantum state ought to result in a density matrix of full rank. The spectral decomposition may have small elements, but they ought to never be zero for a finite amount of data.

A recent publication [52] tries to address this statistical problem along the lines of the compressed sensing approach: instead of finding the most likely quantum state with minimum rank, investigate the most likely quantum state with a maximum on entropy. This condition effectively provides full rank density matrices. Mathematically, this problem is described by

$$\rho = \arg\max_{\rho}\{\gamma\ S_{vN}(\rho) + \log \mathcal{L}(\rho) \mid \rho \geq 0\} \tag{3.6}$$

with S_{vN} the von-Neumann entropy of the quantum state and $\mathcal{L}(\rho)$ describing the likelihood of the quantum state with regards to the obtained data. Eq (3.6) can efficiently be maximised using an iterative method described in Ref. 52. While this routine has been implemented in Innsbruck, there is no clear answer for how γ needs to be chosen. As long as this aspect has not been answered, we will therefore refrain from using this routine.

An alternative way of dealing with the finite number of measurements, and subsequently low-rank density matrices, is presented in Ref. 53: During a tomography, results that are not observed and correspond to events of zero frequency are generally interpreted as a virtual probability of zero. It is possible to hedge against as-yet-unseen possibilities by adding a minimum probability to the observed virtual probabilities. The maximum likelihood estimation applied on this modified data is equivalent to maximising

$$\rho = \arg\max_{\rho}\{\det(\rho)^{\beta}\mathcal{L}(\rho) \mid \rho \geq 0\} \tag{3.7}$$

with β corresponding to the minimum probability added to the virtual probabilities of the data as described in Ref. 53. While appealing, by addressing the problem that a finite number of measurements never provides absolute information, it is not clear how the parameter β needs to be chosen. As long as this significant parameter for the tomography is not derived for a given experiment, this method, similar to the maximum-likelihood maximum-entropy method mentioned above, can not be applied to experimental data in order to address statistical shortcomings of a plain maximum-likelihood reconstruction.

3.1.3 Bayesian inference of quantum states

While linear and maximum-likelihood reconstructions are the dominant reconstruction techniques, they also have several flaws: linear reconstructions may infer non-physical quantum states, maximum-likelihood methods filter negative-eigenvalues to force physical density matrices. Finally, there is one statistical concern: the eigenvalues of a density matrix can be interpreted as the probability of observing the corresponding eigenstate. A finite number of measurements does not grant absolute knowledge, and from that point of view, reconstructed density matrices should not have eigenvalues equal to zero. In other terms, quantum state reconstruction for a finite amount of data should always return quantum states of full rank.

Another problem with the majority of these reconstruction methods is that only one density matrix is provided and no error estimates can be derived directly. Monte-Carlo simulations are numerically intensive and rely on the assumption that the provided probabilities are the true mean values of the projectors (indirectly assuming an infinite number of measurements). This, however, is usually not the case. Projective measurements provide frequencies of results for a certain number of experiments per setting. While 50 results out of 100 will be interpreted as a "virtual" probability of 0.5, an actual probability of 0.4 or 0.6 could also result in the observed frequencies. This consideration directly leads to a slightly different question - away from the single "most likely quantum" state that has generated the observed data, towards "how likely" is it that a specific quantum state has resulted in the data. Calculating these probabilities for a set of quantum states allows one, similar to a Monte-Carlo investigation, to obtain any measure of interest including mean values and standard deviations.

In the following this different approach to describing a system will first be explained by a classical analog - a coin and the question whether it is fair or not. This mathematical concept and description will then be extended to quantum states.

Consider a coin that has been flipped N times and head was found f times. What is the probability that the coin is fair, meaning that the coin has a 50/50 chance to return heads/tails? Heads and tails can be perfectly distinguished and there are only two possible results from flipping the coin. It follows that the statistics are governed by a binomial distribution. The function describing the probability that a certain "fairness" (or probability of returning heads) p can be contributed to the obtained data is referred to as probability distribution function β. For this binomial example, the probability distribution function β reads as [54]

$$\beta(p, f, N) = (N+1) \begin{pmatrix} N \\ f \end{pmatrix} p^f \, (1-p)^{N-f} \tag{3.8}$$

and returns the probability for obtaining f heads in N throws for a given fairness p. From this distribution function, all values of interest can be derived: the mean value of p is $\frac{1+f}{N+2}$, the most likely p (the maximum of β) can be found at $\frac{f}{N}$, and similar numbers such as standard deviation can be directly be calculated. It is important to note that the probability distribution function is likely not symmetric and the mean value will generally not coincide with the most likely value. The above description for coin-flips and the evaluation regarding the fairness of the coin is referred to as Bayesian analysis. In the following, this approach will first be extended to counting events, such as is generally done in photon experiments governed by Poisson distributions, and then be applied to quantum state reconstruction.

If an experiment is based on detecting count rates c_j, combined in a list c, from sources that

show a Poisson distribution, the corresponding probability distribution function is

$$\beta(p,c,N) = \prod_j \frac{p * \mathrm{pois}(c_j, m_k) + (1-p) * \mathrm{pois}(c_j, m_l)}{\mathrm{pois}(c_j, m_k) + \mathrm{pois}(c_j, m_l)} \tag{3.9}$$

with $\mathrm{pois}(c_j, m_{\{k,l\}}) = \frac{m_{\{k,l\}}^{c_j} \exp(-m_{\{k,l\}})}{c_j!}$ representing the normalised probabilities of detecting c_j counts for a given Poisson distribution centred around mean values $m_{\{k,l\}}$. Equation (3.8) can be directly obtained from Eq. (3.9) by assuming perfect distinguishability and considering all possibilities to draw f_i results from N possibilities.

The coin-flipping example was inferring the probability for a specific "fairness" p to generate the observed data. This can now directly be extended for a qubit: While the number of coin flips is replaced by the number of measurements, the number f describing how often head has been detected now corresponds to how often a specific projector has been detected. Finally, the "fairness" p will be replaced by the probability connected to projector P_i acting on a density matrix ρ. If several projectors are used, for instance when measuring $\sigma_{(x,y,z)}$, the total probability p_ρ of a quantum state ρ returning the observed data in the measurement process is given by the product of all probabilities[2]:

$$p_\rho = \frac{\prod_i \beta(\mathrm{tr}(P_i\rho), f_i, N)}{\sum_\rho \prod_i \beta(\mathrm{tr}(P_i\rho), f_i, N)} \tag{3.10}$$

At this stage, the question can be answered regarding the likeliness of a specific quantum state resulting in the observed data. It is important to note here that full state tomography is not required to assign a probability to a quantum state. A single measurement is already sufficient for that.

For a set of quantum states, the probability of generating the observed data can be assigned to each state. After the normalisation of all probabilities, they can be used to infer any measure of interest. For instance, the fidelity F and its error ΔF of an obtained set of state tomography data with respect to a desired state ϕ would then be

$$F(\phi) = \sum_\rho p_\rho F(\rho, \phi) \tag{3.11}$$

$$\Delta F(\phi) = \sqrt{\sum_\rho p_\rho (F(\rho,\phi) - F(\phi))^2} \tag{3.12}$$

The distribution of the probabilities p_ρ has an influence on the calculated measures. Although a maximum-likelihood evaluation may suggest a pure quantum state on the border of the Bloch sphere with a purity of one, a Bayesian inference procedure may yield: the most likely quantum state has a purity of one (in agreement with the maximum-likelihood evaluation) but the average does not necessarily coincide with the maximum for unsymmetric distributions of p_ρ. As an example, linear reconstruction, maximum-likelihood reconstruction, and Bayesian inference are applied on the data provided in Table 3.1 and evaluated assuming 100 measurements per tomography setting. The results can be found in Table 3.2. At first glance, all reconstructions

[2]Numerically it is notably more efficient to calculate $\log(\beta)$ instead and to replace all products with sums accordingly.

	Linear	MaxLik	Bayesian (HilSch)	Bayesian (Haar)
fidelity	98.7(10)	99.2(10)	99(1)	99(1)
purity	1.01(1)	1 ($\Delta = 10^{-16}$)	0.987(10)	0.987(10)

Table 3.2: The very same data of a state tomography may yield notably different values and error estimations based on a Monte-Carlo simulation (assuming 100 measurements per tomography setting) depending on the applied reconstruction method: (Linear) Linear reconstructions of pure quantum state may indicate non-physical states as indicated by a mean purity larger than one, while a maximum likelihood estimation (MaxLik) only yields pure quantum states. Bayesian reconstruction yields plausible error bars of approximately 1%. For the Hilbert Schmidt (HilSch) distribution, 3×10^6 randomly drawn mixed quantum states have been employed while for the Haar distributed mixed quantum states 6×10^6 density matrices have been employed. In the Bayesian case, despite using different prior distributions, sufficient sampling in the proximity of the generated state return the same parameters.

yield about the same fidelity and similar error bars. However, looking at different parameters such as the purity, one can see that the linear reconstruction also suggests non-physical results (purity > 1), while the Monte-Carlo simulation based on maximum likelihood reconstructions only yields pure quantum states. The Bayesian investigations yield mean values and errors consistent with statistical error estimations of about 1%.

An additional advantage of a Bayesian inference can be found in including experimental imperfections in the probability distribution function [55]. For example, experimentally employed operators are likely not identical for all experiments and their distribution may be described by a certain model. These additional error sources may be included in the Bayesian evaluation and answer the question, "Considering these experimental imperfections, which is the most likely quantum state consistent with the observed data?" Including errors in linear or maximum-likelihood functions is more demanding. In these approaches one commonly compares the ideal quantum states, subjected to dominant errors in the experiment, and compares this state with the inferred quantum state from the tomography. This investigation, that a quantum state is realised within expectations of the experimental precision, is however notably different to a Bayesian investigation that includes error sources and experimental imperfections directly.

While a Bayesian investigation may be appealing, there is one considerable drawback: the probability assigned to a quantum state via the Bayesian analysis is normalised over the chosen set of quantum states. In return, the assigned probabilities depend on the chosen set of quantum states. In addition, different distributions of quantum states have different distributions of parameters, which may additionally affect parameters derived from a Bayesian investigation. For example, consider a Bayesian analysis of the purity connected to a state tomography when pure Haar-measure distributed quantum states [40] are employed: considering the normalised probability distribution function and a purity of 1 for all states, a Bayesian analysis of this particular example would yield a mean purity of 1 with a standard deviation of zero - regardless of the actual tomography data. This issue about the dependency of parameters on the chosen quantum state distribution is currently not resolved and is the main argument against Bayesian tomography.

In conclusion, Bayesian inference shows some significant advantages compared to linear and maximum likelihood reconstructions:

a) Compared to linear reconstructions, the Bayesian investigation is restricted to physical

quantum states.

b) The statistical errors of the obtained data are directly included in the inference without assuming the frequencies f_i to correspond to virtual probabilities $p_i = f_i/N$.

c) Both linear and maximum-likelihood reconstruction require full tomography, while Bayesian inference allows one to draw conclusions starting from the very first data point - which become more and more certain with a growing number of measurements.

Especially c) may be important for upcoming large-scale tomographies. Up to now the largest state that has ever been investigated by quantum state tomography is an eight-qubit W-state [20], requiring $3^8 = 6561$ different observables. One of the main challenges of performing state tomography of even larger quantum states is the exponentially growing number of observables that is required to infer the state. Here, Bayesian inference may allow one to guide the tomography in real time: in contrast to a normal tomography, the probabilities assigned to quantum states during a Bayesian analysis indicate which states are more likely responsible for the observed data and allows one to specifically test these states with more precision, effectively reducing the resources required to draw conclusions about the investigated quantum state.

This approach can be even further optimised if the individual binomial distributions can be approximated by normal distributions. Normal distributions are well understood and their behaviour in Bayesian analysis can be described by the so-called Kalman-filter [56]. Here, the computationally demanding investigation over a large sample of density matrices can then be replaced by simple update-equations that are calculated for each additional data point. These update-equations, compared to the evaluation of the probability distribution function for the complete set of states, significantly lower the required computational resources [51].

3.2 Tomography of quantum channels

The techniques used to infer a quantum process are similar to the techniques employed for quantum state reconstruction and are only mentioned briefly here. Linear reconstructions may suggest non-physical processes, a short-coming that maximum likelihood reconstructions do not have. Maximum-likelihood, however, may have a limited validity of error bar estimations. Seeing that for a Bayesian analysis it is not clear which distribution of quantum operations to use, the following investigations about quantum processes will follow a maximum-likelihood reconstruction following an iterative procedure [48].

In Sec. 2.2 unitary operations as well as non-unitary operations have been introduced in the operator-sum representation. Especially the examples of non-unitary processes, such as dephasing (see Fig. 2.3), illustrate that a process may affect only a small number of quantum states and not alter other states. With this background it becomes clear that during the tomography of a quantum process, the entire Hilbert space needs to be sampled as an input into the process, with state tomography being applied to the output state. From this knowledge about how the input Hilbert space is mapped onto the output Hilbert space, the investigated quantum process can then be inferred. The required number of measurement settings can be concluded from the single-qubit Bloch sphere. A naive view may suggest that one eigenstate of each of the axis X, Y, Z might seem to be sufficient to describe the input Hilbert-space. This, however, is not

true as the process may also include interactions such as amplitude damping, requiring $|0\rangle$ as well as $|1\rangle$ in the set of input states. This leads to 4 input states for a sufficient sampling of the input Hilbert-space[3], followed by state tomography of each output state via 3 measurements. In total it is possible to infer the quantum process from $(4 * 3)^N$ different measurement settings, with N being the number of qubits. This scales unfavourably with the number of qubits and currently represents one of the main reasons why process tomography involving more than 3 qubits has not yet been realised.

There exist different solutions that may allow for less demanding process tomographies: Considering the Choi-Jamiolkowski (CJ) isomorphism [38, 39], process tomography of an N-qubit process is equivalent to a state tomography of an $2N$-qubit maximally entangled quantum state, where one half of the qubits was subject to the process of interest. In that respect, the required resources are slightly smaller seeing that N-qubit process tomography requires 12^N measurement settings, while the CJ approach only requires $3^{2N} = 9^N$ settings. This entanglement-assisted tomography [57] is especially suitable for one and two-qubit systems. Currently such an approach is being investigated, with special focus on direct characterisation of quantum dynamics [58]. Here, parameters of the system such as spontaneous decay rates can be inferred from a single measurement setting. For larger systems, however, creation of high-fidelity maximally entangled quantum states becomes significantly more challenging [59] and may represent an experimental limitation favouring a direct process tomography compared to an entanglement-assisted process tomography.

It is important to note that 12^N measurement settings are only necessary if there is no prior knowledge about process and especially its rank. If the process is close to a unitary process, it is described by a few parameters. Subsequently, tomography can be performed with significantly fewer settings following a compressed-sensing approach [49] similar to the ideas discussed in Sec. 3.1.2.

At the moment the most promising approach, however, is likely to be guided tomographies of states and processes that are able to suggest, in real time, observables to improve the overall precision of the tomography, combined with numerically efficient methods to work with more than 10 qubits. This is not only a challenging task from an algorithm point of view - simply storing the information about a quantum process becomes exceedingly challenging on classical computers: Even supercomputers are currently limited to storing the quantum information of about 43 qubits - which is equivalent to being able to describe a 21-qubit quantum process [60].

All the above possible investigation techniques will be susceptible to noise. For a tomography based on 4^N linear independent input states followed by full state tomography, the influence of projection noise should return similar results as the investigation of projection noise affecting state tomography, as discussed in Sec. 3.1.2 and Fig. 3.2: When the quantum process returns a state that happens to be an eigenstate of one of the investigating operations during the state tomography, the projection noise effectively vanishes, resulting in high-fidelity predictions about the investigated process. As a particular example the operation $\exp(i\pi\sigma_\phi)$ acting on a single qubit as well as $\exp(i\pi\sigma_\phi^{(1)}) \cdot \exp(i\pi\sigma_\phi^{(2)})$ and $\exp(i\frac{\pi}{4}\sigma_\phi \otimes \sigma_\phi)$ acting on 2 qubits are investigated in a numerical situation with projection noise being the only error source. Here, $\sigma_\phi^{(i)} = \cos(\phi)\sigma_x^{(i)} + \sin(\phi)\sigma_y^{(i)}$ represents a rotation around an axis in the equator plane of

[3]This can also be understood from a dimensional point of view via the 4 parameters required to describe a Hermitian 2x2 matrix.

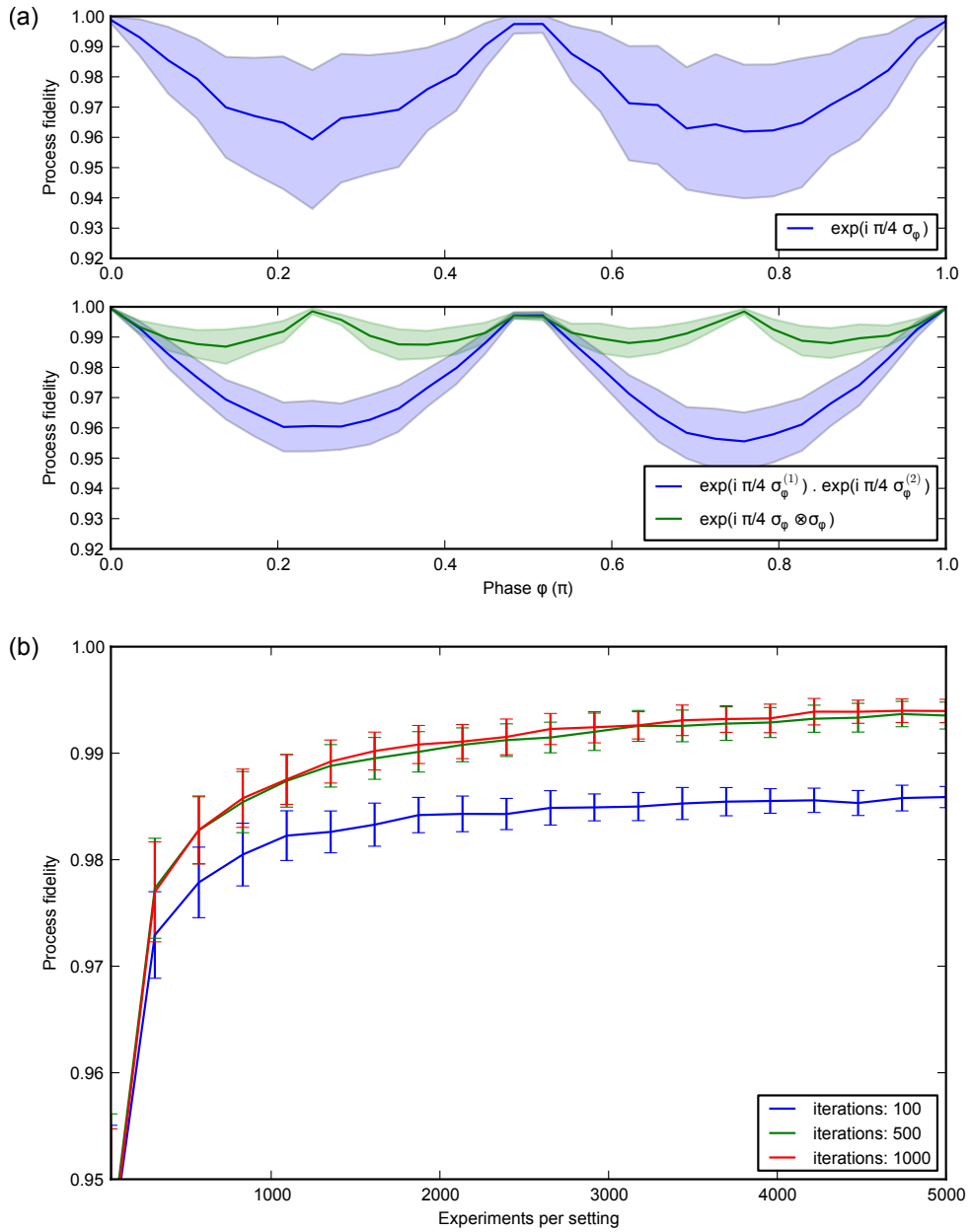

Figure 3.3: Monte-Carlo simulation of process tomographies with respect to projection noise: (a) Mean process fidelity depending on the measurement basis assuming 100 experiments per tomography setting. In the absence of projection noise, the fidelity would be 1. Processes with a Hamiltonian of the form $\sigma_\phi^{(i)} = \cos(\phi)\sigma_x^{(i)} + \sin(\phi)\sigma_y^{(i)}$ acting on qubit i may generate quantum states that are eigenstates of the principal axis $\sigma_{(x,y,z)}$ of the subsequent state tomography. If this is the case, the influence of projection noise basically vanishes, whereas processes that do not yield quantum states that are eigenstates of any operations employed in the state tomography may return an apparent average loss of 4% fidelity solely to projection noise. Here, mean value and standard deviation of the CJ-fidelity are derived from a Monte-Carlo analysis with 100 simulations per point. The iterative process reconstruction [48] was based on 500 iteration steps. (b) Mean process fidelity and its dependence on projection noise. Single qubit process tomography of the operation $\exp(i\pi/4\sigma_\phi)$ with $\sigma_\phi^{(i)} = \cos(\phi)\sigma_x^{(i)} + \sin(\phi)\sigma_y^{(i)}$ and $\phi = \pi/4$ is challenging due to its strong dependence on projection noise (see (a)). An investigation of the iterative reconstruction method employed [48] as a function of the number of iteration steps shows that after 500 steps the reconstruction has converged and more steps (such as the presented values for 1000 steps) do not yield different process fidelities.

the qubits Bloch sphere. Fig. 3.3 a) shows that for phases of $\{0, \pi/2, \pi\}$ (effectively creating eigenstates $\sigma_{\pm(x,y)}$, the operations that are employed during the state tomography) the effect of projection noise vanishes. For other operations, however, projection noise significantly affects tomography: for a single qubit mean deviations between an ideal tomography and the projection noise limited tomography of up to 4% at a standard deviation of about 3% are possible; for two qubits similar effects are found.

If average errors solely due to projection noise are desired to be smaller than 1% then more than 1000 measurements per setting are recommended: A numerical investigation of the operation $\exp(i\pi\sigma_\phi)$ with $\phi = \pi/4$ (the operation that shows the largest susceptibility in Fig. 3.3 a)) for an increasing number of measurements per setting is presented in Fig. 3.3 b). After about 1000 measurements per setting, only marginal improvements can be made. However, performing fewer than 1000 measurements per setting can easily result in deviations of 2% and more.

Considering that the employed reconstruction method is based on an iterative procedure [48], this investigation was, in parallel, employed to investigate a recommended minimum number of iteration steps. Fig. 3.3 b) shows the effect of performing 100, 500 and 1000 iteration steps on equivalent data. For 100 iteration steps the reconstruction method has not converged on the final state yet and shows a deviation of 2%. 500 iteration steps push that deviation to only 1%. An investigation with 1000 iteration steps shows, within the error bars, the same deviations as for 500 iterations - indicating that the procedure has already converged after about 500 iterations.

In conclusion, this chapter has presented currently employed methods of inferring quantum states and process via tomography and in particular pointed out different aspects of linear reconstruction, maximum likelihood investigations and Bayesian analysis of the data obtained. The method which is currently commonly used in Innsbruck is an iterative reconstruction method [48] employed for both quantum states and processes. A numerical evaluation indicates that, without prior knowledge about the process or quantum state, and subsequent optimisation of the measurement procedure, 1000 measurements per tomography setting are recommended to suppress infidelities solely due to projection noise to below 1%. Considering the iterative nature of the reconstruction procedure, 1000 iteration steps are recommended for quantum states while quantum process only require about 500 iteration steps. The methods and ideas described above are not tied to any specific experimental setup. As a next step, the following chapter will introduce the apparatus located at the university of Innsbruck where the above methods and procedures have been successfully employed to investigate quantum states and processes.

Chapter 4

Experimental setup

This chapter provides a brief introduction to ion-trap-based quantum computation in Innsbruck. The setup consists of a linear Paul trap [61] to store a string of Ca^+ ions. Single-ion operations are realised by illuminating individual ions with a tightly focused laser. The centre-of-mass mode is employed to mediate interaction between different qubits. Although a general introduction can be found in Ref. 62, more details are provided in the thesis of my predecessors working on the same apparatus: Descriptions of trap design, trap parameters and vacuum vessel can be found in Stephan Gulde's thesis [63]. The thesis of Mark Riebe [64] focuses on quantum information processing in our ion-trap, and the thesis of Michael Chwalla [65] investigates aspects of quantum metrology with trapped ions. Most of the recent experiments rely on high level control of radio frequency (RF) pulses, which is described in detail in the master thesis of Philipp Schindler [66]. Given these numerous detailed publications on the setup employed, only significant recent changes to the apparatus are presented below.

4.1 $^{40}Ca^+$ for ion-trap-based quantum computation

Multiple ions confined in a linear ion trap form a register of qubits sharing a harmonic oscillation. Generally, internal states of the ions encode quantum information. The shared oscillator mode may also store information and is usually employed as a data-bus in the system, allowing interaction between qubits independent of their location in the register [67].

The qubit register is realised by storing $^{40}Ca^+$ ions in a linear Paul trap. Thermal calcium vapour in the centre of the trap is isotope-selectively ionised by a two-stage photo-ionisation process [72, 73]. The trap parameters are characterised by an axial confinement of $\omega_z \approx 1$ MHz and a radial confinement of $w_r \approx 4$ MHz. The level scheme of $^{40}Ca^+$ (as illustrated in Fig. 4.1) makes it an ideal candidate for quantum computation:

a) The degeneracy of the Zeeman manifold is lifted by applying a homogeneous magnetic field of approximately 3 G with a pair of Helmholtz coils. The precision of the magnetic field is currently limited by current fluctuations of $\frac{\Delta I}{I} \approx 10^{-5}$.

b) Doppler cooling [74, 75] can be performed on the $S_{1/2} \leftrightarrow P_{1/2}$ transition, aided by a repumper on the $P_{1/2} \leftrightarrow D_{3/2}$ transition. The ion string is cooled to about 15 phonons axially and approximately 4 phonons radially after 3.5 ms.

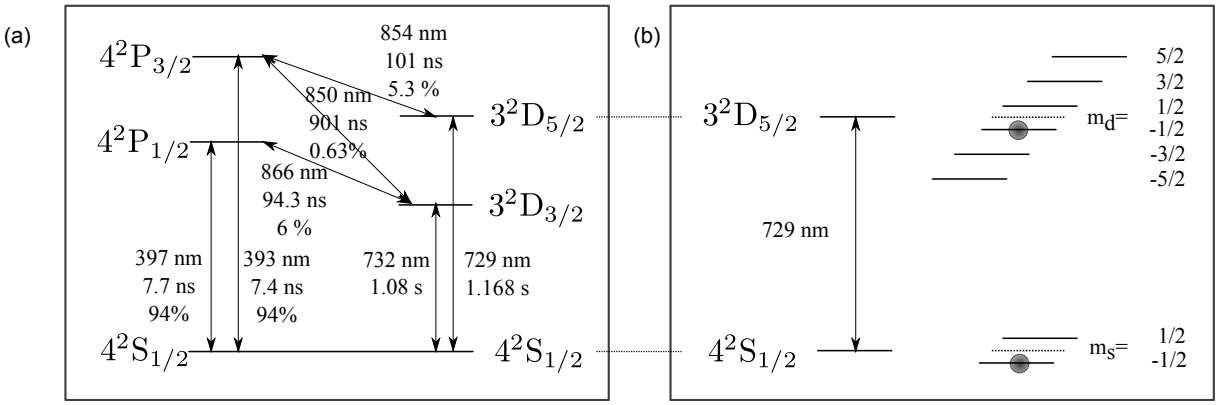

Figure 4.1: Currently employed transitions in $^{40}Ca^+$ (a) The $S_{1/2} \leftrightarrow P_{1/2}$ transition at 397 nm is used for Doppler cooling (aided by resonant 866 nm light on the $P_{1/2} \leftrightarrow D_{3/2}$ transition as a repumper from the metastable $D_{3/2}$ state) as well as state detection of the $S_{1/2} \leftrightarrow D_{5/2}$ manifold via electron shelving. Quantum information processing is performed on the $S_{1/2} \leftrightarrow D_{5/2}$ transition at 729 nm. Lifetimes have been taken from Ref. 68 with the lifetime of the $D_{5/2}$ updated from Refs. 69, 70, branching ratios from Ref. 71. (b) A magnetic field lifts the degeneracy of the Zeeman-sublevels. Quantum information is generally encoded in $|1\rangle = |S\rangle = S_{1/2}(m = -1/2)$ and $|0\rangle = |D\rangle = D_{5/2}(m = -1/2)$, indicated by the filled circles.

c) State initialisation: σ polarised light along the magnetic field axis prepares the ions in $S_{1/2}(m = -1/2)$ with a probability of success of >99.1% [Data07b] .

d) The $D_{5/2}$ state manifold has a lifetime of 1.168 s due to spontaneous decay [69, 70] which directly determines the lifetime of the qubit (apart from dephasing due to laser and magnetic field fluctuations). This is significantly longer than qubit operations that take place on a timescale of 10-100 μs.

e) Excitation on the sideband transition $S_{1/2}(m = -1/2) \leftrightarrow D_{5/2}(m = -5/2)$ is quenched by a laser light field on the $D_{5/2} \leftrightarrow P_{3/2}$ transition which results in sideband cooling [76]. The centre-of-mass mode of the ion string is initialised in the axial ground state with a probability of about 99% [77, 78] after 8 ms.

The qubit is encoded in the states $|1\rangle = |S\rangle = |4^2S_{1/2}(m = -1/2)\rangle$ and $|0\rangle = |D\rangle = |3^2D_{5/2}(m = -1/2)\rangle$ of a single ion. Electron shelving [17] is employed on the $S_{1/2} \leftrightarrow P_{1/2}$ transition to distinguish between the two levels with a precision >99% for a single ion. Scattered photons at 397 nm are detected with a photo-multiplier tube (PMT) and, if required, by a CCD camera. The PMT is employed as a fast quantum register readout, requiring about 2-4 ms of detection time, with the disadvantage that only the number of $|D\rangle$ and $|S\rangle$ states in the register can be detected without knowing which ions are excited. The CCD camera is able to detect the individual populations of a quantum state but requires about 8-10 ms detection time. This technique projects qubits on either $|S\rangle = |1\rangle$ or $|D\rangle = |0\rangle$ and can therefore be interpreted as a measurement along $\sigma_z^{(i)}$ of the individual qubits. Additional operations prior to the measurement allow one to perform measurements in an arbitrary basis: considering that $\sigma_x \equiv \sigma_y\sigma_z\sigma_y$, the quantum state $|\psi\rangle$ can be investigated along σ_z directly via electron shelving while an investigation along σ_x requires the additional application of operation $U_y = \exp(i\frac{\pi}{4}\sigma_y)$

on $|\psi\rangle$:

$$\langle\psi|\sigma_x|\psi\rangle \equiv (\langle\psi|U_y^\dagger)\sigma_z(U_y|\psi\rangle) \tag{4.1}$$

Trap frequencies of about 1 MHz result in a spread of the single qubit wave packet of about 11 nm which is notably smaller than the transition wavelength of 729 nm and allow us to describe the system in the Lamb-Dicke approximation [79]. The narrow-linewidth 729 nm laser (≈5 Hz [Data10a]) enables discrete excitation of individual levels in the system. Fig. 4.2 shows the spectrum of a Ca ion in our linear ion trap: The different carrier transitions coupling $S_{1/2}(m = -1/2)$ to $D_{5/2}(m = \{-5/2, -1/2, +3/2\})$ are well distinguished. Their width corresponds to the respective coupling strength. Sidebands show up symmetrically around the carrier transitions and correspond to the centre-of-mass mode, the radial mode, micromotion and other higher-order modes.

Restricting the computational Hilbert space to $|S\rangle = |1\rangle$, $|D\rangle = |0\rangle$ and the centre-of-mass mode, the reduced level scheme of a single $^{40}Ca^{+}$ ion is depicted in Fig. 4.3. The quantum state of an ion string with 5 ions, for example, is described by

$$|\psi\rangle = |01001\rangle \otimes |n\rangle = |01001, n\rangle. \tag{4.2}$$

$|01001\rangle$ represents an exemplary electronic state of the ion string in the binary representation and n represents the number of phonons in the centre-of-mass mode. Resonant laser light couples $|S, n\rangle \leftrightarrow |D, n\rangle$ which corresponds to a unitary operation [29]

$$\mathrm{R}_{\mathrm{car}}(\theta, \phi, k) = \exp(-i\frac{\theta}{2}\sigma_\phi^{(i)}) = \cos(\frac{\theta}{2})\ \mathbb{1} - i\sin(\frac{\theta}{2})(\sigma^+\exp(i\phi) + \sigma^-\exp(-i\phi)). \tag{4.3}$$

Here, $\sigma^{+(-)}$ are (de)excitation operators or atomic flip operators on ion k, θ represents the equivalent of a rotation angle around a certain axis in the Bloch sphere and is given by $\theta = \Omega_{\mathrm{car}}^{(k)}\, t$, with Ω_{car} being the Rabi frequency on ion k on the carrier transition and t being the time that the resonant light field illuminates ion k. $\sigma_\phi = \cos(\phi)\sigma_x + \sin(\phi)\sigma_y$ defines the rotation axis. The phase ϕ of the rotation angle is defined by the phase of the light field illuminating the ion.

The same mathematical description applies to atom-light interactions resonant with the blue sideband $|S, n\rangle \leftrightarrow |D, n+1\rangle$

$$\mathrm{R}_{\mathrm{blue}}(\theta, \phi, k) = \cos(\frac{\theta}{2})\ \mathbb{1} - i\sin(\frac{\theta}{2})(\sigma^+a^\dagger\exp(i\phi) + \sigma^-a\exp(-i\phi)) \tag{4.4}$$

and the red sideband $|S, n\rangle \leftrightarrow |D, n-1\rangle$

$$\mathrm{R}_{\mathrm{red}}(\theta, \phi, k) = \cos(\frac{\theta}{2})\ \mathbb{1} - i\sin(\frac{\theta}{2})(\sigma^+a\exp(i\phi) + \sigma^-a^\dagger\exp(-i\phi)) \tag{4.5}$$

with $a^\dagger(a)$ being the raising (lowering) operator of the harmonic oscillator and the rotation angle $\theta = \Omega_{\mathrm{sb}}t$, depending on the Rabi frequency Ω_{sb} on the sideband and illumination time t. On the blue sideband the Rabi frequency is $\Omega_{\mathrm{blue}} = \sqrt{n+1}\ \eta\ \Omega_{\mathrm{car}}$ (in first order of the Lamb-Dicke regime [80]), while on the red sideband it is $\Omega_{\mathrm{red}} = \sqrt{n}\ \eta\ \Omega_{\mathrm{car}}$. In both cases the coupling strength to the sideband is characterised by the Lamb-Dicke parameter $\eta = \sqrt{\frac{\hbar}{2m\omega}}\vec{k}\vec{e}_{\mathrm{ax}}$ [81] , where m is the mass of the ion, ω is the trap frequency for the chosen mode along the direction

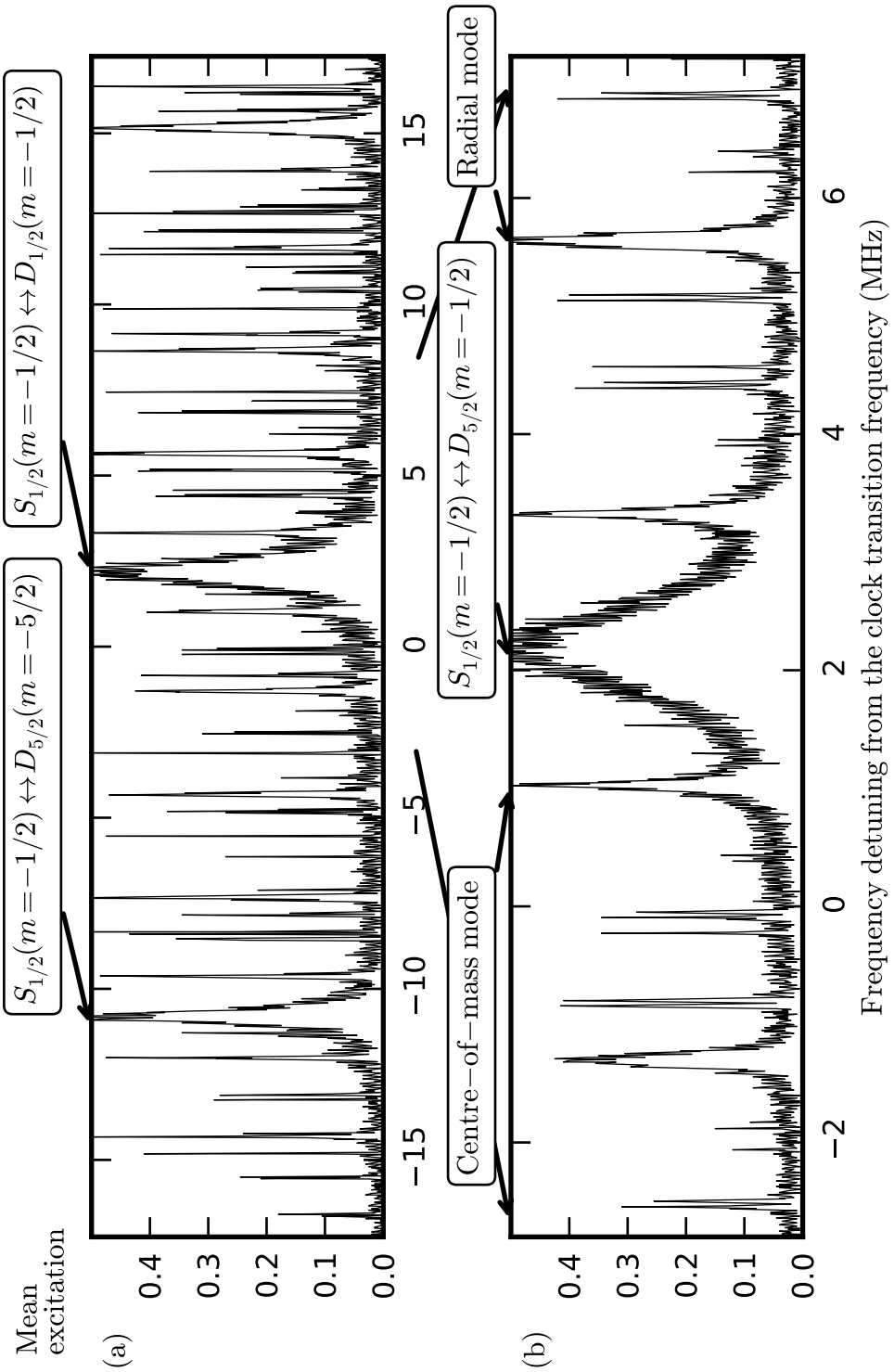

Figure 4.2: Excitation spectrum of a single $^{40}Ca^{+}$ in a harmonic potential after illumination with a detuned 729 nm laser. (a) The plot shows a spectrum for a Zeeman splitting at about 3 G (see also Fig. 4.1 b)). Transitions correspond to the different carrier transitions accompanied by their sidebands. (b) Focusing on the qubit transition $|S\rangle \leftrightarrow |D\rangle$ (located at about 2 MHz), the centre-of-mass mode sidebands at 1 MHz, the radial mode sidebands at approx. 4 MHz and higher order modes are well distinguished [Data10g].

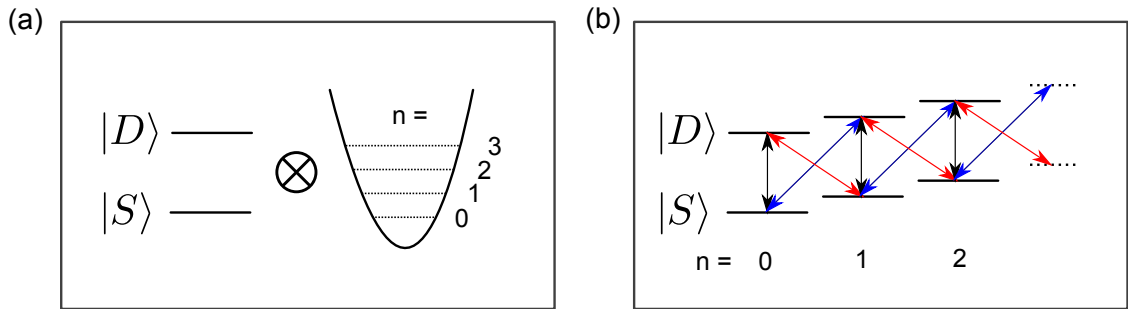

Figure 4.3: Effective level scheme of a two-level atom coupled to a harmonic oscillator: (a) A two-level system is coupled to a harmonic oscillator. (b) The carrier transition couples $|S,n\rangle$ and $|D,n\rangle$. Light resonant with the motional sidebands (usually to the centre-of-mass mode) couples $|S,n\rangle \leftrightarrow |D,n+1\rangle$ (blue) or $|S,n\rangle \leftrightarrow |D,n-1\rangle$ (red) and may add or remove excitations from the harmonic oscillator.

$\vec{e}_{\mathrm{ax}}$ compared to the wave vector of the incident laser-beam defined by $\vec{k}$. For our geometry, stored $^{40}Ca^{+}$ ions and the wavelength of the qubit transition λ =729 nm, the Lamb-Dicke parameters are usually about 2.7% and 4.1% for addressed and global illumination, respectively.

A light-field detuned far detuned from resonant transitions does not change populations, yet induces an AC-Stark shift [82, 83]. Its mathematical description follows

$$R_{\mathrm{zred}}(\theta,k) = \exp(i\frac{\theta}{2}\sigma_z^{(k)}) \tag{4.6}$$

with $\theta = \frac{\Omega^2}{4\Delta}t$ the accumulated phase, Ω the Rabi frequency of the light field and Δ the detuning. The detuning is usually about -20 MHz. For these settings, the phase of the light-field is can be neglected.

4.2 Magnetic shield

The above description on atom-light interactions assumes a resonant excitation on the transitions of interest and no spontaneous emission. Considering atoms with a Zeeman-structure illuminated by laser light, this ideally requires:

a) a negligible linewidth of the laser light field,

b) and a stable magnetic field with fluctuations causing an effective linewidth smaller than the atomic-transition linewidth.

Neither requirement is met at the current stage in our laboratory. Compared to laser frequency fluctuations, magnetic-field fluctuations are dominant. Both effects can be observed as a dephasing of the quantum register, i.e. the apparent phase of the quantum register becomes less defined with increasing noise influence from the environment. An experimental procedure to investigate dephasing is provided by Ramsey experiments [84]: At time $t = 0$ a single qubit is initialised in an equal superposition of $|0\rangle$ and $|1\rangle$ with a predefined phase with respect to a reference - usually the resonant laser (see Fig. 4.4). In an ideal case, the phase of the qubit compared to the reference would not change over time. However, relative energy fluctuations

of the qubit with respect to the reference will cause undetermined phase changes of the qubit. After averaging over these fluctuations the length of the Bloch vector is reduced, i.e., the state becomes partially mixed. This effect is equivalent to a loss of quantum phase information. A direct way of quantifying the remaining information is to probe the quantum state via an operation $R(\pi/2, \phi)$ after waiting for a time t_{R}. A varying phase ϕ will map the remaining quantum state onto a set of new states. Ideally the populations would vary between $|0\rangle\langle 0|$ and $|1\rangle\langle 1|$ (Fig. 4.4). If phase information has been lost during the waiting time t_{R}, the contrast of the oscillations will be reduced. The remaining contrast, usually referred to as Ramsey contrast, directly corresponds to the remaining phase information. Investigating the contrast as a function of time provides information about how long quantum information can be stored in a given apparatus. Even more information about the apparatus and its environment can be gained from a similar investigation performed on transitions with different sensitivities to the magnetic field. Laser-frequency fluctuations affect transitions with different magnetic-field sensitivities equally, while magnetic-field fluctuations result in a loss of contrast with time constants depending on the respective magnetic-field sensitivities. Combining the measured Ramsey contrast decays allows one to infer estimates on the amplitude of laser frequency and magnetic field fluctuations.

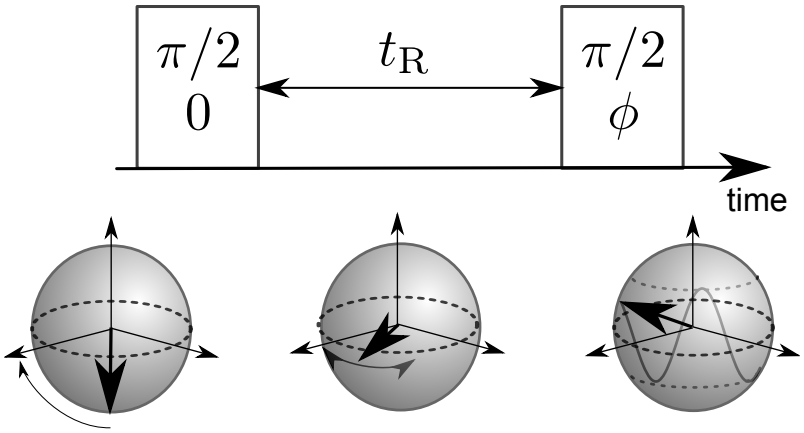

Figure 4.4: Schematic of a Ramsey experiment: A qubit is initialised in an equal superposition of $|0\rangle$ and $|1\rangle$ by the first Ramsey pulse and evolves for a time t_{R}. During that time, relative frequency fluctuations between the qubit and the phase reference may cause the averaged Bloch vector to shrink in length. The second pulse allows the investigation of the remaining coherence, equivalent to measuring the purity of the quantum state, by inducing oscillations of the populations with varying ϕ. Only a pure state will show oscillations with full contrast, while a loss of quantum information results in a reduced amplitude of the oscillations.

Previously, coherence times in our apparatus could be gradually improved from about 1 to 10 ms [64, p.65][65]. This time scale limits the length and therefore the possible complexity of quantum algorithms in the given setup. In 2007, a μ-metal shield[1] was installed (see Fig. 4.5), enclosing the complete vacuum chamber including most of the optical setup necessary for illuminating the ions. Spurious magnetic fields due to ground loops in the experimental setup have been reduced. In total, these changes resulted in an improved setup yielding a coherence

[1] Imedco, Proj.Nr.: 3310.68; characterisation in May 25$^{\mathrm{th}}$ and 26$^{\mathrm{th}}$, 2009; Attenuation: >28dB @ 0.01-1Hz, >40dB @ 10Hz, >61dB @ 100Hz, >67dB @ 1000Hz

decay as a function of time as shown in Fig. 4.6: Here, the decay is modelled via $\exp(-t/T_2^*)$ with $\frac{1}{T_2^*} = \frac{1}{2T_1} + \frac{1}{\tau}$. T_1 corresponds to the lifetime of the excited state with $T_1 = 1.168$ s and, apart from a factor of 2, represents an upper bound on the possible coherence time [29, 85]. Note that the Ramsey experiments have been performed without spin-echo pulses as indicated by the label T_2^*. The decay described by τ can be solely contributed to laser frequency and magnetic field fluctuations and yields on transition $m_S = -1/2 \leftrightarrow m_D = -1/2$ yields $\tau(m_S = -1/2 \leftrightarrow m_D = -1/2) = 95(7)$ ms while transition $m_S = -1/2 \leftrightarrow m_D = -5/2$ shows $\tau(m_S = -1/2 \leftrightarrow m_D = -5/2) = 15(2)$ ms.

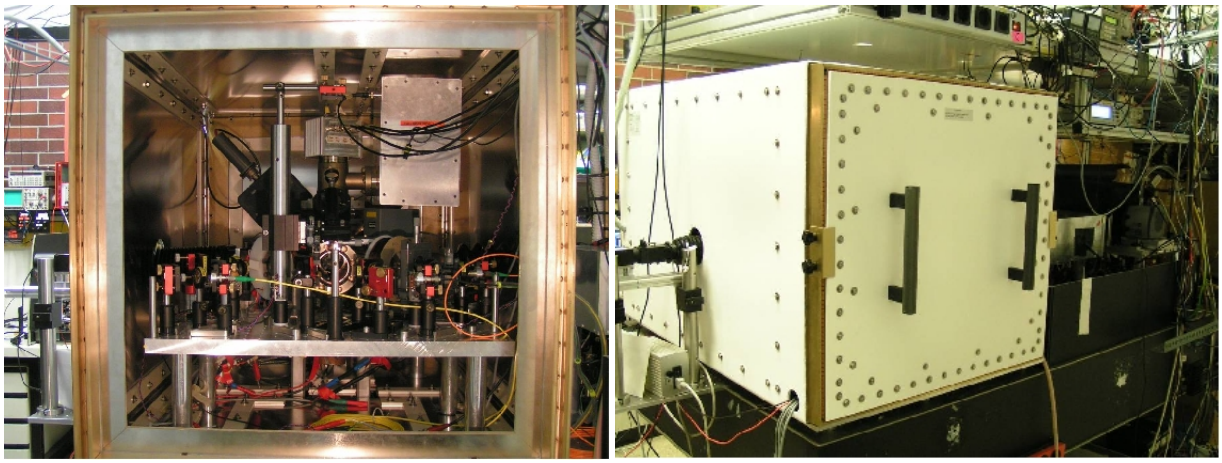

Figure 4.5: View of the vacuum chamber enclosed by the magnetic shield in 2007. Doors at the front and back allow access to optics but are usually kept closed. Additional holes in the shield are used for electronic connections as well as optical access.

Assuming only magnetic field fluctuations and considering a relative magnetic field sensitivity of the two transitions of 5, the expected ratio between the coherence times ought to be $5^2 = 25$ (for details see Appendix A). On the other hand, assuming laser frequency fluctuations only, the ratio between the two coherence times ought to be equal to 1. With the coherence time investigated on two transitions of different sensitivity to magnetic field fluctuations, we can calculate the coherence times that we ought to observe in the presence of either only magnetic field fluctuations or only laser frequency fluctuations. The coherence time only due to magnetic field fluctuations, denoted by τ_B, is $\tau_B = 427(68)$ ms (for the $m_S = -1/2 \leftrightarrow m_D = -1/2$ transition), while laser frequency fluctuations alone yield a coherence time τ_L of $\tau_L = 128(15)$ ms. In this respect we are currently mainly limited by laser frequency fluctuations.

It ought to be noted that the University of Innsbruck made significant changes to the power distribution within the lab area in 2010/11. Investigations have shown that power cables with no devices attached carry currents of up to 2 A. It is presently not clear whether these currents are the result of ground loops combined with the high conductance of the cables or directly induced by unshielded cables running next to each other in the basement of the building. Regardless, the induced magnetic fields affect the experimental setup and result in coherence times of only about 30 ms, compared to the previous $\approx$ 100 ms.

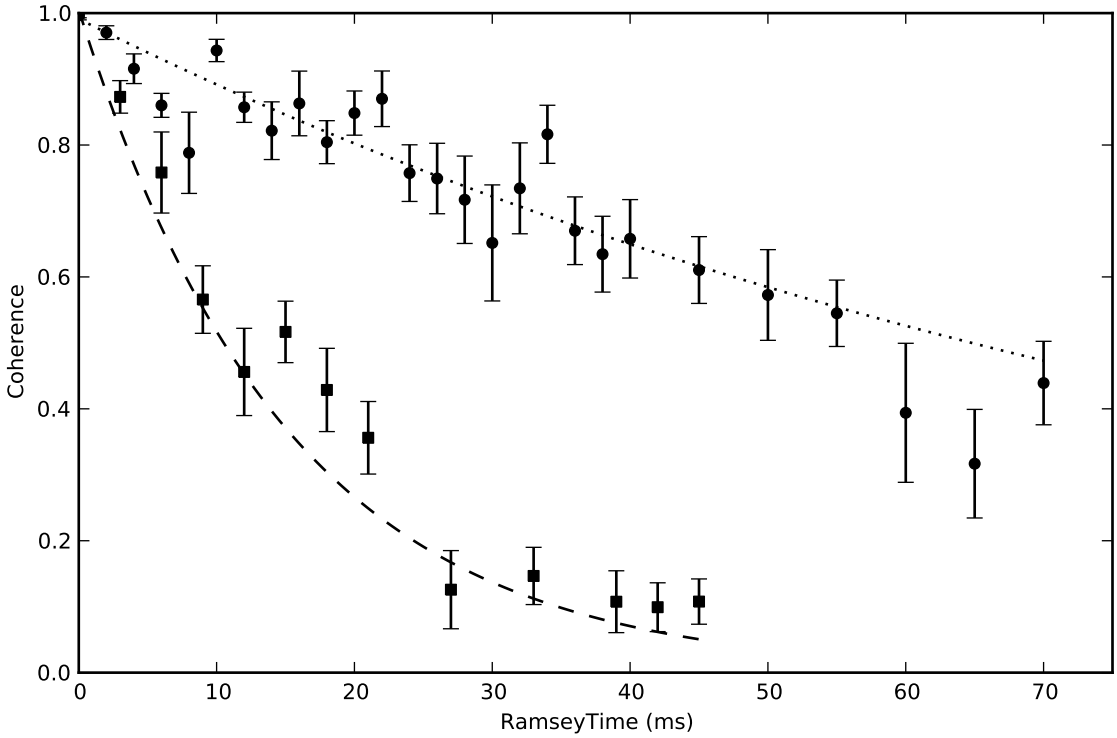

Figure 4.6: Coherence decay of a single qubit: Ramsey experiments on the $S(m = -1/2) \leftrightarrow D(m = -1/2)$ transition (circles) shows a loss of contrast versus time in good agreement with an exponential decay with a time constant of about 100 ms. A similar investigation on the $S_{m_S=-1/2} \leftrightarrow D_{m_D=-5/2}$ transition (squares), which is by a factor 5 more sensitive to magnetic field fluctuations, yields a time constant of about 15 ms [Data10f].

4.3 Collective operations on the quantum register

The original setup was capable of illuminating individual ions up to a string of 8 Ca^+ qubits [62]. Performing the same quantum operation on each qubit of the quantum register consisting of N qubits therefore required N individual operations. The general idea was to speed up these operations by globally illuminating the complete ion string with equal intensity, thus performing N single-qubit operations on the quantum string at once.

This enhancement has been implemented in the apparatus by increasing the intensity of the 729 nm laser sent to the experiment to about 220 mW, which is split into about 20 mW for the addressed beam and 200 mW for the global beam (see Fig. 4.7 a)). Similar to the optical setup of the addressed beam [65], intensity and frequency of the global beam can be changed via a double-pass configuration followed by a subsequent single-pass acousto-optical modulator (AOM). Usually, 80.05 MHz RF is applied to this single-pass AOM. However, should bichromatic light fields be required, these can be generated by applying two radio-frequencies simultaneously on the single-pass AOM. After the single-pass AOM, the light fields of the addressed as well as global beam are coupled into individual fibres which lead into the magnetic shield towards the vacuum chamber.

Homogeneous illumination of an ion string would dictate a broad beam shape while, on the other hand, fast operations require high Rabi frequencies and favour a well focused beam. The addressing optics for the global beam has therefore been chosen similar to the optics of the addressed beam [64]: a telescope increases the beam diameter (see upper platform in Fig. 4.7 b)) before it is focused down onto the ion string via an objective lens on the lower platform. Here, an improved overlap of the beam profile with the ion string is reached by using cylindrical lenses in the telescope in contrast to spherical lenses. The objective lens in front of the vacuum chamber is mounted on a motorised XYZ translation stage[2] which allows one to compensate for slow beam-pointing drifts. Depending on the size of the ion string, the beam diameter can be increased at the cost of a reduced Rabi frequency. This can be compensated for by the RF power on the double-pass AOM.

Different optical paths, especially the individual fibres, cause a loss of coherence between the global and addressed light field. This, however, only marginally affects quantum computation in the presented experiment: The qubits can not successfully be driven on resonance and phase stably using the global as well as the addressed beam due to the loss of phase coherence between the two beam paths. However, it is possible to drive all qubits resonantly via the global beam and employ local AC-shifts on individual qubits via the addressed beam. Using this approach of collective operations on the entire string combined with local phase-shift operations on individual qubits one can still perform all single-qubit quantum operations employing refocusing techniques [86].

The approach based on collective operations on all qubits combined with individual phase shifts yields one significant advantage compared to the previous approach of resonantly driving individual qubits: The ion distance in the string is about 4 μm, while the beam waist is about 2 μm. When a single ion is addressed, there is a residual light field illuminating the neighbouring ions and causes undesired operations on these. This effect can be quantified by the ratio of the Rabi frequency of neighbouring ions compared to the addressed ion. This quantity is referred to as addressing error and is usually about 3%. One ought to keep in mind that this is referring to an effect where one ion is driven resonantly and neighbouring ions see the attenuated, yet resonant light field. It follows that the undesired effect on neighbouring qubits is proportional to the field. In the case of addressed phase shifts based on the AC-Stark effect, the operation does not depend on the field but on the intensity. From that point of view, undesired operations on neighbouring ions are not proportional to the addressing error but its square. This results in an effective addressing error for AC-Stark operations of below 0.1%. It follows that collective operations combined with single-qubit phase shifts ought to return significantly higher fidelities compared to resonantly driven single-qubit operations via the addressed beam only. On the other hand, the need to apply refocusing pulses when using collective operations combined with single-qubit phase shifts increases the susceptibility to phase noise. In light of the coherence time in the presented apparatus of about 30 ms and novel techniques to effectively implement quantum algorithms as presented in Sec. 5.3, collective operations via the global beam combined with addressed phase shifts outperform previously employed techniques.

The final geometry of the ion trap with regards to the magnetic field and additional lasers such as the σ-beam for state initialisation or photoionisation is shown in Fig. 4.7 c). Besides the additional global beam, this remains the same as presented in Ref. 63–65.

[2]Newport: M-460A-XYZ, NSC200-KT, NSA12, NSC200

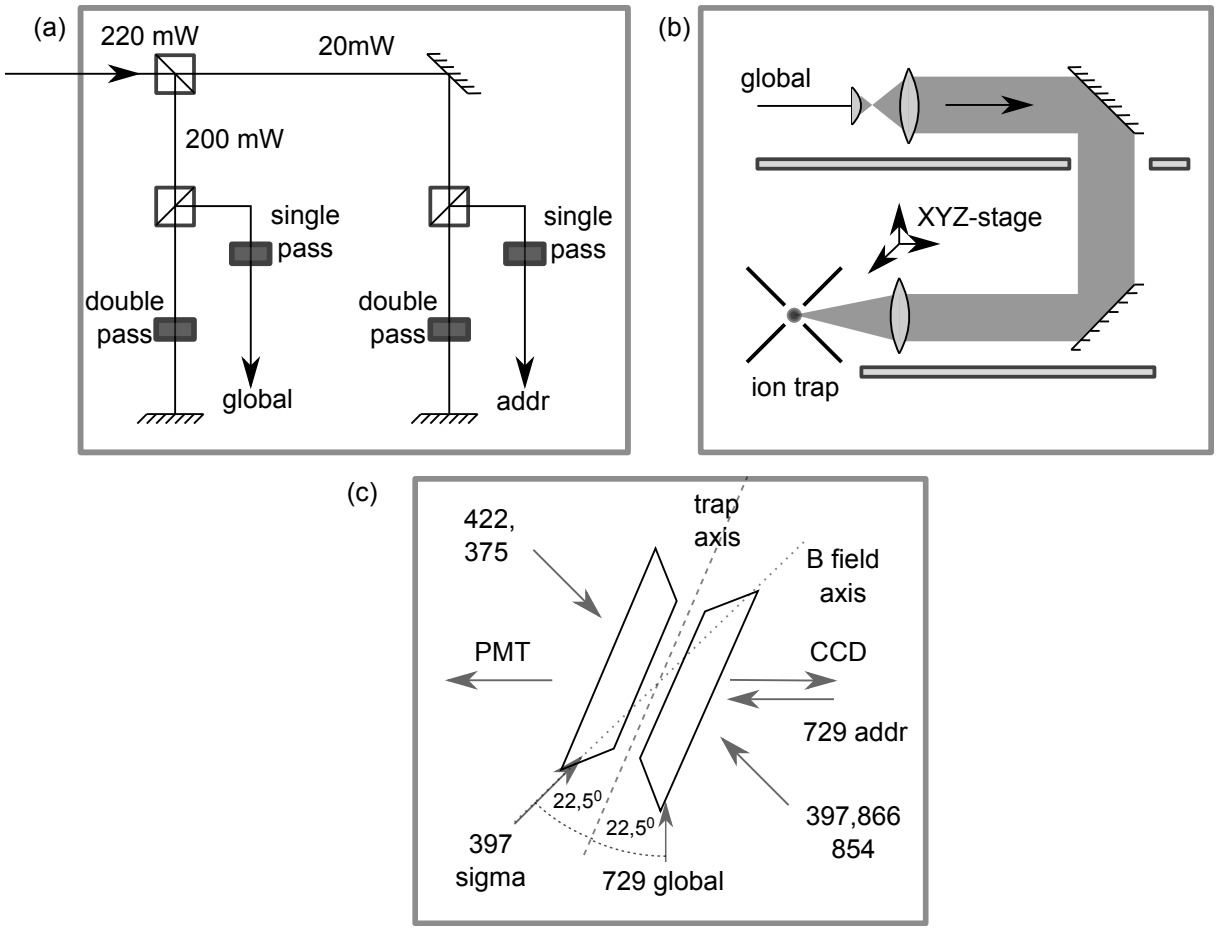

Figure 4.7: Optical setup including global addressing of the quantum register: (a) Roughly 220 mW of light are required in total and split into two branches, one with about 200 mW and one with 20 mW. The optical setup for the addressed beam as presented in Ref. 64 has been equipped with an additional single-pass AOM to realise bichromatic light fields, if required. The optical setup for the global addressing is identical in functionality to the addressed-beam setup. (b) Due to space constraints a second platform had to be installed within the magnetic shielding, with the top platform providing the proper beam shape. The lower platform holds a $\lambda/2$ waveplate (not shown) and a lens mounted on a motorised, computer controlled XYZ translation stage. The translation stage is usually disconnected from its power source to lower magnetic field noise. (c) Photo-ionisation and detection beams are counterpropagating to facilitate beam alignment with stored ions. 397 nm light in σ-polarisation along the magnetic-field axis initialises the qubits. 729 nm light on the qubit transition can either address the entire quantum register (global) or individual qubits (addressed). Detection is performed via a PMT or, additionally, a CCD camera. An angle of 22.5° between trap axis and magnetic field or alternatively of (90-22.5)° between trap axis and addressed beam allows one to drive sideband transitions.

This chapter has briefly introduced the experimental setup employed to perform quantum information processing with trapped ions. The basic operations have been introduced yet a detailed analysis with regards to universal quantum computation in the presented apparatus is still missing. The following chapter will address this point and show how universal quantum computation with trapped ions can be implemented and characterised with the tools presented in this and the previous chapters.

Chapter 5

Experimental implementation of quantum operations

The majority of manipulations of the ion string are carried out on the carrier and the blue-sideband transitions. Experiments are performed by illuminating the ion string as described in Sec. 4.1. Rotation angle as well as phase of the light-field in the following pulse sequences are defined in units of π. Preparation sequences, such as Doppler cooling, sideband cooling or state initialisation for process tomography, as well as special detection sequences, such as electron shelving or additional state tomography pulses, are not included in the pulse sequences. The terminology for the majority of laser-ion interactions is provided in Seq. 5.1. Experimentally obtained datasets are referenced in Appendix E while an overview of some of the implemented operations can be found at the end of this section in Tab. 5.1.

Sequence 5.1 Table of pulse conventions

	# everything after a # will denote comments in pulse sequences
Rcar(θ, ϕ, k)	# corresponds to a rotation on ion k of angle θ
	# on the carrier transition $S_{1/2}$(m=-1/2) $\leftrightarrow$ $D_{5/2}$(m=-1/2)
	# around σ_ϕ as defined in Eq. (4.3)
	# if n is g, the interaction is applied globally to the complete
	# quantum register
Pause(1000)	# a waiting time between pulses, provided in microseconds
Rcar2(θ, ϕ, k)	# interaction on the transition $S_{1/2}$(m=-1/2) $\leftrightarrow$ $D_{5/2}$(m=-5/2)
Rzred(θ, k)	# AC stark shift pulse on ion $k \equiv \exp(-i\,\theta\,\sigma_z^{(k)})$ (see Eq. (4.6))
Rblue(θ, ϕ, k)	# the blue sideband transition follows the definition in Eq. (4.4)

5.1 Single-qubit operations

Single-qubit operations were introduced in Eq. (4.3) and Eq. (4.4). Experimentally, these operations are often considered with a focus on rotation angles and phases. This approach, however, makes it more difficult to directly compare the functionality of gate implementations with regards to various setups that may be based on different physical systems. Here, we consider

a more general description in terms of operations in the Pauli basis which may allow for a faster understanding of implemented algorithms for a broader audience. The equivalence table between chosen light fields and logical operations is:

$$\begin{array}{ll} R_x(\theta) = R(\theta, \pi) & R_{\bar{x}}(\theta) = R(\theta, 0) \\ R_y(\theta) = R(\theta, \pi/2) & R_{\bar{y}}(\theta) = R(\theta, 3\pi/2) \end{array} \tag{5.1}$$

with $R_{x(y)}(\theta)$ describing rotations around the $x(y)$ axis of the qubit's Bloch sphere with a rotation angle θ. Rotations in the opposite direction are denoted by $\bar{x}(\bar{y})$ and only require an additional phase shift of π. It is important to point out that there is a critical argument concerning the convention. The Schrödinger equation [2] $i\hbar\partial_t|\psi\rangle = \hat{H}|\psi\rangle$, with $|\psi\rangle$ being a quantum state and $\hat{H}$ being a time-independent Hamiltonian of the system, describes the time evolution of the state $|\psi\rangle$. From it follows that $|\psi(t)\rangle = \exp(-\frac{i}{\hbar}\hat{H}t)|\psi(t=0)\rangle$. It is important to note the negative sign of the exponent in this equation. Considering that a rotation around the x-axis is often described as $R_x(\theta) = \exp(i\frac{\theta}{2}\sigma_x)$, this operation is implemented via $-\sigma_x$ to correct for the additional sign. This explains the definition of $R_x(\theta) = R(\theta, \pi)$, although the related Hamiltonian corresponds to $\bar{x}$.

Single-qubit operations are performed by tightly focusing a tight laser beam onto a single ion, ideally illuminating only the targeted atom. However, the Gaussian beam profile extends to the neighbouring ions and induces a similar operation[1], although significantly weaker. The parameter to describe this unitary, yet undesired, interaction is provided by the addressing error α. It is defined by the ratio of the Rabi frequency of the neighbouring ion to the target ion and is usually about 3%. This undesired effect can, however, be reduced at the cost of more operations. The general idea is based on refocusing techniques [87, p.88][86]: An operation

$$R(\theta, \phi, k) = \mathrm{Rzred}(1, k)\ R(\theta/2, \phi - 1, k)\ \mathrm{Rzred}(1, k)\ R(\theta/2, \phi, k) \tag{5.2}$$

is split into two equal yet counteracting parts with an additional phase-flip, implemented via an AC-Stark shift, in between. Aside from an additional phase factor, the composite pulse sequence implements the desired operation. On neighbouring ions the effective operation is notably different. While field-dependent operations affect neighbouring ions with a ratio of α, the intensity-depending AC-Stark effect only affects neighbouring ions proportional to α^2 - which is negligible for usual settings. The counter-acting operations on neighbouring ions are

$$R(\alpha\theta/2, \phi - 1, k)\ \mathrm{Rzred}(\alpha^2, k)\ R(\alpha\theta/2, \phi, k) \simeq R(\alpha\theta/2, \phi - 1, k)\ R(\alpha\theta/2, \phi, k) \simeq \mathbb{1}$$

and therefore effectively suppressed.

This approach can be generalised for global interactions. Employing collective carrier interactions using the global beam introduced in Sec 4.3 combined with addressed single-qubit Stark shifts, any local operation can be implemented on the quantum register with the advantage of intrinsic addressing-error correction. This, however, comes at the cost of a higher sensitivity to intensity fluctuations in the AC-Stark shift pulses.

[1] Note that the k-vector of the light field affecting neighbouring ions is slightly different compared to direct addressing. Thus the phase of the light field, and subsequently the operation, on the neighbouring ion is not identical: an operation $\exp(i\theta\sigma_\phi)$ on one qubit will induce an operation $\exp(i\alpha\theta\sigma_{\phi'})$ on the neighbouring qubit with ϕ not necessarily equal to ϕ'.

The laser employed on the quadrupole transition is compensated for frequency drifts [65, p.82]. In addition, the magnetic field is tracked via Ramsey experiments [65], with all transition frequencies constantly updated on the timescale of seconds. Quantum operations on the blue sideband require the additional information about the current centre-of-mass mode frequency. An efficient way of determining the sideband frequency is to initially probe the sideband with weak excitation for a rough determination and subsequently perform a high-resolution Ramsey experiment on the motional sideband.

The basic scheme is similar to a normal Ramsey experiment as described in Sec. 4.2. Here the initial superposition is created via the carrier transition, leading to $|S,0\rangle$ and $|D,0\rangle$. An additional mapping pulse on the blue sideband transfers the state $|S,0\rangle$ into $|D,1\rangle$, effectively realising the desired starting superposition $|\psi\rangle = |D,0+1\rangle$. This state is insensitive to laser and magnetic field fluctuations and only susceptible to heating and frequency changes of the motion. Thus the present technique allows for interrogation times of more than 100 ms. It is only limited by the lifetime of the $|D\rangle$ state and the coherence of the motional mode. After the Ramsey waiting time, the rest of the pulse sequence in Seq. 5.2 maps the remaining state back into its initial state $|S,0\rangle + |D,0\rangle$ which is an eigenstate of the operation Rblue(1/2, 0.5, 1) and is therefore unchanged. However, if there is a detuning Δ_{sb} of the employed blue sideband frequency on the laser with respect to the actual COM-mode frequency, the output state will depend on the Ramsey time. Scanning this Ramsey time, the excitation of the output state will oscillate with the frequency of the detuning Δ_{sb} between laser and actual COM-mode. These long Ramsey times allow determination of the sideband frequency with a precision of a few Hz which is mandatory for some of the experiments presented in the following.

Sequence 5.2 Ramsey experiment on the motional sideband

Rcar(1/2,0,1)	# $\|S,0\rangle \rightarrow \frac{1}{\sqrt{2}}(\|S\rangle + \|D\rangle) \otimes \|n=0\rangle$
Rblue(1/2, 0, 1)	# create superposition on the motion: $\rightarrow \frac{1}{\sqrt{2}}\|D,0+1\rangle$
Pause(τ)	# Ramsey waiting time
Rblue(1,1,1)	# undo map into motion: $\rightarrow \frac{1}{\sqrt{2}}(\|S\rangle + \exp(i\Delta_{\mathrm{sb}}\tau)\|D\rangle) \otimes \|n=0\rangle$
Rcar(1/2, 0.5, 1)	# second Ramsey pulse

Once the trap frequency is determined, the blue sideband[2] can be used to map the electronic state of a single qubit onto the motion. Performing an Rblue(π) on a qubit of state $(\alpha|S\rangle + \beta|D\rangle) \otimes |n=0\rangle$ maps the qubit information onto the motional superposition $|D\rangle \otimes (\alpha|n=1\rangle + \beta|n=0\rangle)$. This information is now shared by all ions. At that stage, motional-state dependent quantum operations can be performed on any qubit in the quantum register with the quantised motion of the ion string acting as a data bus.

5.2 Multi-qubit quantum gates

While arbitrary single-qubit operations are relatively easy to implement in the apparatus given, quantum computation on the complete quantum register requires entangling operations between

[2]When an ion is illuminated resonantly on the blue sideband, Stark shifts occur via coupling of the light field to other transitions. An additional beam of appropriate power and detuned by 40 MHz to the red is employed to compensate for this effect [83].

multiple qubits [88, 89]. In the following, different techniques will be discussed for implementing multi-qubit operations in an ion-trap-based quantum computer.

5.2.1 Cirac-Zoller based two-qubit phase gate

A controlled-NOT (CNOT) gate applies a bit-flip operation on a target qubit depending on the state of a control qubit. Its functionality is well known from classical information processing yet generates new effects in the field of quantum mechanics. Consider the control qubit to be in a superposition, $|c\rangle = \frac{1}{\sqrt{2}}(|0\rangle + |1\rangle)$ and the target state to be in $|t\rangle = |0\rangle$. From this particular input the CNOT will generate a maximally entangled state. Replacing the initial superposition by a Hadamard operation

$$H = \frac{1}{\sqrt{2}} \begin{pmatrix} 1 & 1 \\ 1 & -1 \end{pmatrix}, \tag{5.3}$$

equivalent to a R($\pi/2$,ϕ) pulse, acting on either $|0\rangle$ or $|1\rangle$, the two-qubit product basis will be mapped onto the Bell basis:

$$\begin{array}{lllll} |c\rangle \otimes |t\rangle : & |0\rangle \otimes |0\rangle & \overset{\mathrm{H}}{\longleftrightarrow} & \frac{1}{\sqrt{2}}(|0\rangle + |1\rangle) \otimes |0\rangle & \overset{\mathrm{CNOT}}{\longleftrightarrow} \quad \frac{1}{\sqrt{2}}(|00\rangle + |11\rangle) \\ & |0\rangle \otimes |1\rangle & \overset{\mathrm{H}}{\longleftrightarrow} & \frac{1}{\sqrt{2}}(|0\rangle + |1\rangle) \otimes |1\rangle & \overset{\mathrm{CNOT}}{\longleftrightarrow} \quad \frac{1}{\sqrt{2}}(|01\rangle + |10\rangle) \\ & |1\rangle \otimes |0\rangle & \overset{\mathrm{H}}{\longleftrightarrow} & \frac{1}{\sqrt{2}}(|0\rangle - |1\rangle) \otimes |0\rangle & \overset{\mathrm{CNOT}}{\longleftrightarrow} \quad \frac{1}{\sqrt{2}}(|00\rangle - |11\rangle) \\ & |1\rangle \otimes |1\rangle & \overset{\mathrm{H}}{\longleftrightarrow} & \frac{1}{\sqrt{2}}(|0\rangle - |1\rangle) \otimes |1\rangle & \overset{\mathrm{CNOT}}{\longleftrightarrow} \quad \frac{1}{\sqrt{2}}(|01\rangle - |10\rangle) \end{array} \tag{5.4}$$

Here, all operations are unitary and can be inverted. Vice versa, the above sequence maps from entangled states onto product states. This technique can be employed to perform measurements in the entangled basis. Measurements in the presented ion-trap quantum computer employ electron-shelving which is equivalent to projections along $\sigma_z^{(i)}$ on the involved qubits. Adding the unitary map from Bell- to product-basis before the measurement, the projective measurements can now be interpreted as measurements in the entangled Bell basis.

Note that the CNOT operation not only represents a basic building block to create entanglement in a quantum register. Together with arbitrary single-qubit operations it forms a universal set of gates that allows for arbitrary quantum computation on the complete quantum register [88, 89].

One of the first realisations of a CNOT gate operation in an ion-trap based quantum computer was based on the idea of Cirac and Zoller (C&Z) [67]. A CNOT gate is equivalent to a phase gate that is enclosed by two Ramsey pulses. The phase gate is described by a matrix of diagonal form with all but one element having the same sign. An example is shown in Eq. (5.5). An intuitive picture of how such an operation can be implemented in an ion-trap quantum computer is presented in Fig. 5.1. Neglecting different coupling strengths for the moment, a 2π pulse on the blue sideband will add a minus sign to all quantum states but $|D, 0\rangle$, which does not couple to the blue sideband. The corresponding operation, a controlled phase gate, in the basis $\{|D, 0\rangle, |D, 1\rangle, |S, 0\rangle, |S, 1\rangle\}$ is

$$\mathrm{C-Phase} = \begin{pmatrix} 1 & 0 & 0 & 0 \\ 0 & -1 & 0 & 0 \\ 0 & 0 & -1 & 0 \\ 0 & 0 & 0 & -1 \end{pmatrix} \tag{5.5}$$

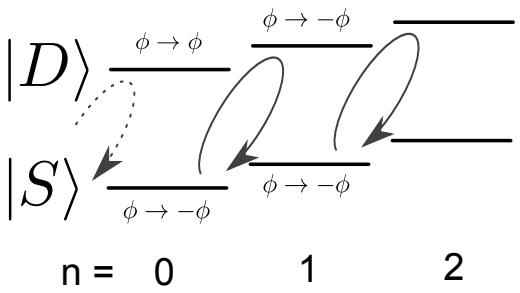

Figure 5.1: Basic idea behind a phase gate following the idea of Cirac and Zoller. The blue sideband does not couple to the state $|D,0\rangle$. When a 2π pulse is implemented on the blue sideband on all involved transitions (compensated for the different coupling strengths), all populations will remain the same. However, all states except $|D,0\rangle$, will additionally obtain a phase $\exp(i\frac{2\pi}{2}) = -1$.

If this phase gate is enclosed by two Ramsey pulses, the additional phase is effectively mapped into a controlled bit-flip. Here, the phase of the first Ramsey pulse defines whether the unitary operation corresponds to a controlled-X or a controlled-Y operation. Although the implementation of such a CNOT gate seems to be straight forward at first glance, the coupling strength on the motional blue sideband, proportional to $\sqrt{n+1}$, does not allow one to implement a 2π pulse on all transitions with a single interaction without leaving the computational subspace of $|S,D\rangle \otimes |n=0,1\rangle$. This problem concerning different coupling strengths can be solved by employing a composite pulse sequence that implements an effective 2π pulse on the blue sideband for all quantum states involved. A pulse sequence fulfilling this requirement is presented in Seq. 5.3 [18, 90]. The implementation of this pulse sequence, with its unitary map shown in Eq. (5.6), yields a process fidelity of $\mathcal{F}_{\mathrm{CJ}}(U^{\mathrm{long}}_{\mathrm{CNOT}}, \mathcal{E}_{\mathrm{exp}}) = 88.8(7)\%$ and a mean process fidelity of $\bar{\mathcal{F}}(U^{\mathrm{long}}_{\mathrm{CNOT}}, \mathcal{E}_{\mathrm{exp}}) = 91.0(6)\%$ for pure quantum states randomly drawn according to the Haar measure [90].

Sequence 5.3 Controlled NOT operation – long version

Rblue(1, 0, 1)	# map electronic state of qubit 1 on the motion
Rcar(0.5, 0, 2)	# first Ramsey pulse on the target qubit 2
Rblue(1, 0, 2)	# composite phase gate [63, 64]
Rblue($1/\sqrt{2}$, 0.5, 2)	
Rblue(1, 0, 2)	
Rblue($1/\sqrt{2}$, 0.5, 2)	
Rcar(0.5, 1, 2)	# second Ramsey pulse on the target qubit 2
Rblue(1, 1, 1)	# mapping of the motion onto the control qubit

$$U_{\mathrm{CNOT}}^{\mathrm{long}} = \begin{pmatrix} 0 & -i & 0 & 0 \\ i & 0 & 0 & 0 \\ 0 & 0 & -1 & 0 \\ 0 & 0 & 0 & -1 \end{pmatrix} \tag{5.6}$$

The CNOT pulse sequence presented in Seq. 5.3 can be shortened as shown in Seq. 5.4 [90]: The phase gate can also be implemented via 3 pulses. Considering $n = 0$, the first $\frac{\pi}{2}$ pulse generates a superposition of the qubit in the equator plane. This state is an eigenstate of the second pulse and not affected by it, while the third pulse reverses the operation of the first phase gate pulse. If $n = 1$, the effective rotation angles are larger by a factor of $\sqrt{n+1} = \sqrt{2}$. Now the first pulse does not create an eigenstate of the second pulse anymore. However, the rotation angle of the second pulse $\theta = \sqrt{2}$ is chosen such that it now equals an effective $\sqrt{2} \cdot \sqrt{2}\pi = 2\pi$ pulse which maps the quantum state back onto itself. The third pulse, again, maps the quantum state back onto the original state. In total, this three-pulse sequence will not affect the populations, yet will return different phases. The unitary map corresponding to Seq. 5.4 is shown in Eq. (5.7). The additional phase rotations on target (1) and control (2) qubit $U_{\mathrm{Z}} = \exp(-i(1 - \frac{1}{\sqrt{8}})\pi\sigma_z^{(2)}) \exp(-i\frac{1}{\sqrt{8}}\pi\sigma_z^{(1)})$ can be compensated by changing the phase of all following laser pulses on the corresponding ions.

Sequence 5.4 Controlled NOT operation – short version

Rblue(1, 0, 1)	# map electronic state of qubit 1 on the motion
Rcar(0.5, 0, 2)	# first Ramsey pulse on the target qubit 2
Rblue(0.5, 1, 2) Rblue($\sqrt{2}$, 0.5, 2) Rblue(0.5, 0, 2)	# short phase gate [90]
Rcar(0.5, 1/$\sqrt{2}$-1, 2)	# second Ramsey pulse on the target qubit 2
Rblue(1, 1, 1)	

$$U_{\mathrm{CNOT}}^{\mathrm{short}} = U_{\mathrm{Z}} \cdot \begin{pmatrix} 1 & 0 & 0 & 0 \\ 0 & 1 & 0 & 0 \\ 0 & 0 & 0 & i \\ 0 & 0 & -i & 0 \end{pmatrix} \tag{5.7}$$

Under the same conditions as for the realisation of the standard CNOT gate from Seq. 5.3, the shortened implementation slightly outperforms the standard implementation with a process fidelity of $\mathcal{F}_{\mathrm{CJ}}(U_{\mathrm{CNOT}}^{\mathrm{short}}, \mathcal{E}_{\mathrm{exp}}) = 90.8(6)\%$ and a mean process fidelity of $\bar{\mathcal{F}}(U_{\mathrm{CNOT}}^{\mathrm{short}}, \mathcal{E}_{\mathrm{exp}}) = 92.6(6)\%$ [90]. The main limitations are [18]: laser intensity fluctuations ($\approx 3\%$), laser frequency fluctuations (≈ 50 Hz), laser frequency detuning (< 50 Hz), phonon state initialisation ($\approx 1\%$), addressing error on neighbouring ions ($\approx 3\%$), and off-resonant excitations. While these errors are not negligible, extensive simulations do not fully explain the remaining infidelity of the gate operations. The simulated infidelities are much lower than these observed in

the experiment. This discrepancy might be explained by shortcomings of the simulation program employed. Some of these shortcomings are: no laser frequency fluctuations or magnetic field fluctuations during the simulation of individual pulses and subsequently no well-defined correlation time of noise sources; spontaneous decay during the detection time has not been included (an error of about 1% per qubit); qubit initialisation (with an infidelity of about 0.3% per qubit) was not included. These additional error sources are addressed by an improved simulation program that is currently being written by Shannon Wang (MIT) and myself.

5.2.2 Stark-shift-induced phase gate

An alternative method for implementing a phase gate is based on the non-linear coupling strength of the sidebands depending on the phonon number [91]. In Eq. (4.4), the coupling strength on the blue sideband was introduced proportional to $\sqrt{n+1}$ with n being the phonon number. A beam detuned by Δ from the blue sideband will therefore introduce a phonon-state dependent AC-Stark shift $\frac{\Omega^2_{\mathrm{blue}}(n)}{4\Delta}$. In addition, that light field induces dominant Stark-shifts by coupling to dipole transitions as well as off-resonant coupling to the carrier transition. These Stark shifts, however, can be compensated for [83]. The remaining phase shift on the states of an ion qubit is then

$$\Delta\phi = \frac{\eta^2\Omega^2 t}{4\Delta} n \tag{5.8}$$

with the Lamb-Dicke parameter η, the corresponding Rabi frequency Ω on the carrier transition, the time t that the ion is illuminated by a light field detuned by Δ from the sideband, and the phonon number n of the quantum state [91].

Considering the Hilbert space $|S,0\rangle, |D,0\rangle, |S,1\rangle, |D,1\rangle$, detuning and interaction time can be chosen such that phase shift $\Delta\phi = \frac{\pi}{2}$. When this condition is fulfilled, $|S,1\rangle$ and $|D,1\rangle$ effectively acquire a phase $\pm i$, while $|S,0\rangle$ and $|D,0\rangle$ remain untouched:

$$U^{\mathrm{stark}}_{\mathrm{phase}} = \begin{pmatrix} 1 & 0 & 0 & 0 \\ 0 & 1 & 0 & 0 \\ 0 & 0 & i & 0 \\ 0 & 0 & 0 & -i \end{pmatrix} \tag{5.9}$$

Similar to the ideas of C&Z, a single pulse on the blue sideband maps the electronic information of the control qubit onto the motion and is reversed after the phase gate. Enclosing this AC-Stark-shift gate by two Ramsey pulses, a CNOT operation can be realised with its unitary map depicted in Eq. (5.10).

$$U^{\mathrm{stark}}_{\mathrm{CNOT}} = \begin{pmatrix} 1 & 0 & 0 & 0 \\ 0 & 1 & 0 & 0 \\ 0 & 0 & 0 & -1 \\ 0 & 0 & 1 & 0 \end{pmatrix} \tag{5.10}$$

In Ref. 91, the basic behaviour of the phase gate has been presented including a truth table of the operation. The elements correspond to a mean overlap in the truth table of 86(2)%. The main challenge of this CNOT-implementation is the calibration of the Stark-shift compensation on dipole and carrier transitions which is linearly sensitive to intensity fluctuations.

5.2.3 SWAP gate

Entanglement is a distinct feature of quantum mechanics. Arbitrary quantum computation therefore requires, besides single-qubit operations, also at least one entangling quantum operation. However, not all multi-qubit operations in a quantum algorithm need to be entangling. For example, exchanging the quantum information between two qubits does not create entanglement - it could be implemented in a purely classical way by exchanging, or swapping, the qubits themselves. This so-called SWAP operation, while not entangling, nevertheless shows up in algorithms.

One possibility to implement a SWAP gate is to consecutively apply 3 CNOT gates with alternating target and control qubits [29, p.23]. Considering process fidelities for the CNOT gate of about 90% (see above), such an implementation would very likely result in an unsatisfying performance. However, in an ion-trap based quantum computer a composite pulse sequence allows one to implement a SWAP gate significantly more efficiently [63, 92]. A composite pulse sequence (see Seq. 5.5) realises a SWAP gate operation between the electronic and motional state. Enclosing this operation by mapping pulses from the electronic onto the motional state of a second qubit, the quantum state between two arbitrary qubits in the quantum register can be exchanged. The unitary map that corresponds to the pulse sequence in Seq. 5.5 is presented in Eq. (5.11). The additional unitary operation $U_{\mathrm{Z}} = \exp(i\frac{\sqrt{2}}{4}\sigma_z^{(1)})\exp(-i\frac{\sqrt{2}}{4}\sigma_z^{(2)})$ corresponds to a phase rotation on the two qubits and can either be implemented as operations or be compensated for by changing the phase of all following pulses on said qubits.

Sequence 5.5 Swap gate operation

Rblue(1, 0, 1)	# map electronic state of qubit 1 on the motion
Rblue($1/\sqrt{2}$, 0, 2)	# exchange phonon state with electronic state
Rblue($2/\sqrt{2}$, $\arccos(\cot^2(\pi/\sqrt{2}))/\pi$, 2)	
Rblue($1/\sqrt{2}$, 0, 2)	
Rblue(1, 1, 1)	

$$U_{\mathrm{SWAP}} = U_{\mathrm{Z}} \cdot \begin{pmatrix} 1 & 0 & 0 & 0 \\ 0 & 0 & -1 & 0 \\ 0 & 1 & 0 & 0 \\ 0 & 0 & 0 & 1 \end{pmatrix} \tag{5.11}$$

5.2.4 The quantum Toffoli gate operation

Any quantum algorithm can be decomposed into single-qubit operations and CNOT gates acting on the quantum register. Algorithms, however, are often described in terms of functional units that may include more than two-qubit interactions. One popular functional element in logic algorithms that exceeds a two-qubit interaction is the Toffoli gate. Similar to its classical counterpart, this operation performs a bit flip on a target qubit if and only if both of the two control qubits are in a specific state (usually in the state $|1\rangle$). The Toffoli gate operation can be

found in numerous algorithms such as the three-qubit quantum error correction [29, p.425] or the seven-qubit Shor algorithm [93].

The Toffoli gate can be decomposed into a sequence consisting of single-qubit interactions combined with five two-qubit interactions [94], or if two-qubit interactions are restricted to CNOT operations, six CNOT gates [95]. For the latter approach based on CNOT operations the Toffoli gate is estimated to perform with a fidelity of approximately $0.91^6 \approx 0.56$, disregarding additional errors from other sources.

Considering this low estimated performance of a Toffoli gate based on CNOT operations, it may be advantageous to look for more efficient methods of implementing the desired three-qubit quantum gate. Based on the idea of Cirac and Zoller [67], the implementation of a Toffoli gate gives rise to two problems:

a) The computational phonon Hilbert-space restricted to at most one phonon is only able to store, from a dimensional consideration, the electronic state of a single control qubit. If the electronic state of more than one control qubit needs to be encoded in the motional space, higher phonon excitations will be necessary.

b) The composite phase gate employed in the C&Z-CNOT gate operation only performs correctly in the Hilbert space of the target qubit combined with at most one phonon excitation [18].

These two aspects contradict each other and suggest that there might not be a solution based on the ideas of Cirac and Zoller. Nevertheless three different experimental implementations of a Toffoli gate have been found, implemented and fully characterised in our setup. All implementations are based on the idea of encoding the information of the control qubits onto the phonon bus and performing a bit-flip operation on any target qubit in the quantum register.

For the moment an implementation based on the C&Z phase gate will be considered. It requires an encoding sequence that will generate one phonon if and only if both control qubits are in the same state $|1\rangle$, and zero phonons for all other cases. While this may seem to not be possible from a dimensional point of view, this turns out to be incorrect as the remaining quantum state of the control qubits is neglected. Consider the pulse sequence in Seq. 5.6. The first two pulses generate at most two phonons if the control qubits are in state $|SS\rangle$ and fewer phonons in all other cases:

$$\begin{aligned}
|c_1c_2\rangle = |SS,0\rangle &\quad\rightarrow\quad |DD,2\rangle \\
|c_1c_2\rangle = |SD,0\rangle &\quad\rightarrow\quad \sin\tfrac{\pi}{2\sqrt{2}}|DD,1\rangle + \cos\tfrac{\pi}{2\sqrt{2}}|DS,0\rangle \\
|c_1c_2\rangle = |DS,0\rangle &\quad\rightarrow\quad \cos\tfrac{\pi}{2\sqrt{2}}|DD,1\rangle - \sin\tfrac{\pi}{2\sqrt{2}}|DS,0\rangle \\
|c_1c_2\rangle = |DD,0\rangle &\quad\rightarrow\quad |DD,0\rangle
\end{aligned}$$

It is important to point out that the first control qubit will always be in the D state after mapping its electronic state onto the motion, regardless of its initial state. This allows one to employ the blue sideband to remove a phonon from the system using a composite pulse sequence (pulses 3-5 in Seq. 5.6) similar to the short phase gate employed in the C&Z CNOT operation (compare with Seq. 5.4). In conclusion, the encoding pulses 1-5 presented in Seq. 5.6 will encode the control qubits into the motional quantum bus, generating at most one phonon in the case that the control state was $|SS\rangle$ and no phonon for all other possible control states. The remainder of

Sequence 5.6 Quantum Toffoli gate based on the short CZ phase gate

1:	Rblue(1, 1.5, 1)	# map electronic state of qubit 1 on the motion
2:	Rcar($\frac{1}{\sqrt{2}}$, 1.5, 2)	# map electronic state of qubit 2 on motion
3:	Rblue($\frac{1}{2\sqrt{2}}$, 0.5, 1)	# remove one phonon from the system
4:	Rblue(1, 0, 1)	
5:	Rblue($\frac{1}{2\sqrt{2}}$, 0.5, 1)	
6:	Rcar(0.5, 0, 3)	# first Ramsey pulse on the target qubit 3
7:	Rblue(0.5, 1, 2)	# short phase gate on target qubit
8:	Rblue($\frac{1}{\sqrt{2}}$, 0.5, 2)	
9:	Rblue(0.5, 0, 2)	
10:	Rcar(0.5, $\frac{1}{\sqrt{2}}$-1, 3)	# second Ramsey pulse on the target qubit 3
11:	Rblue($\frac{1}{2\sqrt{2}}$, -0.5+$\frac{1}{\sqrt{2}}$, 1)	# undo encoding
12:	Rblue(1, -1+$\frac{1}{\sqrt{2}}$, 1)	
13:	Rblue($\frac{1}{2\sqrt{2}}$, -0.5+$\frac{1}{\sqrt{2}}$, 1)	
14:	Rblue($\frac{1}{\sqrt{2}}$, 0.5+$\frac{1}{\sqrt{2}}$, 2)	
15:	Rblue(1, 0.5+$\frac{1}{\sqrt{2}}$, 1)	

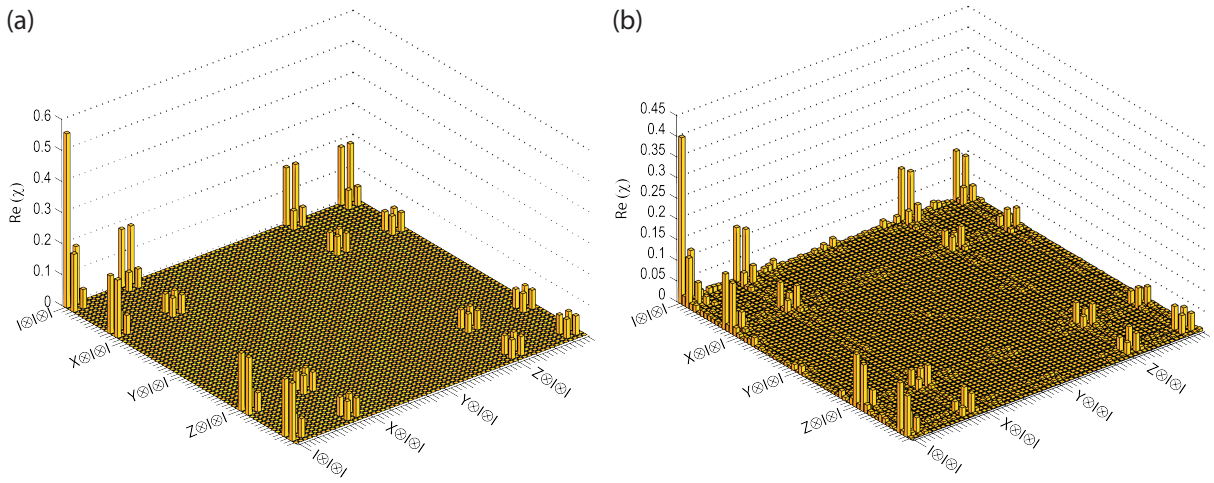

Figure 5.2: Ideal and experimentally obtained χ-matrix of a Toffoli gate implementation: a) Ideal χ-matrix corresponding to the unitary map from Eq. (5.12) implemented by Seq. 5.6. b) χ-matrix derived from full process tomography of an implementation of Seq. 5.6. The process-fidelity between the experimentally realised operation and the desired operation of a Toffoli gate is 66.6(5)%.

the pulse sequence is straightforward and follows the ideas of the short CNOT gate operation presented in Sec. 5.2.1 where Ramsey pulses enclose a composite phase gate acting on the target qubit. At this point the phase of the subsequent pulses needs to be matched with the operation of the short phase gate (see Seq. 5.4 and Eq. (5.7)). The phase shift on the control qubits is directly included in the phase of the blue sideband pulses, while the phase of the target qubit can either be corrected by local operations or be included in the phase definition of all following laser pulses acting on the target qubit. In total, the pulse sequence as shown in Seq. 5.6 corresponds to the unitary operation $U^{\text{short}}_{\text{Toffoli}}$ presented in Eq. (5.12). The performance of this pulse sequence has been investigated via process tomography and was found to operate at a process fidelity of 66.6(5)% [Data07j] equivalent to a mean gate fidelity of 70(3)% for states randomly drawn according to the Haar measure. It should be noted that 5% of the raw data consists of zeros and remain unchanged in the Monte-Carlo investigation for error bars (see Sec. 3). The observed infidelity follows our expectations. Considering that the encoding sequence consists of a composite pulse sequence very similar to the short phase gate (see Seq. 5.4), the overall fidelity of the Toffoli gate is expected to yield fidelities similar to 3 concatenated short CNOT operations of about $0.91^3 \approx 0.75$.

$$U^{\text{short}}_{\text{Toffoli}} = \exp(i\pi \frac{1}{2\sqrt{2}} \sigma_z^{(t)}) \cdot \begin{pmatrix} 1 & 0 & 0 & 0 & 0 & 0 & 0 & 0 \\ 0 & 1 & 0 & 0 & 0 & 0 & 0 & 0 \\ 0 & 0 & 1 & 0 & 0 & 0 & 0 & 0 \\ 0 & 0 & 0 & 1 & 0 & 0 & 0 & 0 \\ 0 & 0 & 0 & 0 & 1 & 0 & 0 & 0 \\ 0 & 0 & 0 & 0 & 0 & 1 & 0 & 0 \\ 0 & 0 & 0 & 0 & 0 & 0 & 0 & i \\ 0 & 0 & 0 & 0 & 0 & 0 & -i & 0 \end{pmatrix} \tag{5.12}$$

It is straightforward to see that the very same encoding can also be employed for a Toffoli

gate based on the four-pulse composite phase gate (see Seq. 5.3). Considering previous findings that the four-pulse composite phase gate performs worse [90], also the Toffoli gate based on the long phase gate is found to perform slightly worse [Data07k] than the Toffoli gate introduced above. A process fidelity of 58.8(4)% is obtained, corresponding to a mean process fidelity of 63(3)%. Here, 4% of the dataset are zeros and remain unchanged during the Monte-Carlo investigation.

One of the challenges of the above pulse sequences is the removal of one phonon during the encoding sequence. Its implementation is similar to the short phase gate and therefore operates at about 90% fidelity. If alternative phase gates were available, this challenging part of the encoding sequence could be simplified. Considering that the first qubit will always be in the state $|D\rangle$, an alternative approach is based on removing one phonon by a single π-flip pulse on the blue sideband. For $n = 2$, this operation will not remove one phonon completely as the effective rotation angle will be $\sqrt{2}\pi$. This undesired effect, however, can be compensated by a novel phase gate that also performs with two phonons present in the motional state.

The required phase gate needs to correspond to an effective 2π pulse on the blue sideband including up to two phonons in the input Hilbert space. Regarding the number of parameters (2 rotation angles and one phase), this problem is solvable with regards to 3 different coupling strengths. A composite phase gate relies on finding a set of at least two pulses that take any initial state from $|S, D\rangle \otimes |n = 0, 1, 2\rangle$ and map it onto an equal superposition of the corresponding Bloch sphere of the applied blue-sideband interaction. For the chosen Hilbert-space this corresponds to finding θ_1, θ_2 and ϕ such that any state $|S, n = 0, 1, 2\rangle$ is mapped onto $|S, n = 0, 1, 2\rangle + |D, n = 1, 2, 3\rangle$. This corresponds to three conditions that need to be fulfilled by three parameters of two blue-sideband pulses. These two pulses map any initial state onto the equator of the respective Bloch sphere. Adding the same pulses again will map S to D for $|n = 0, 1, 2\rangle$ and finally, if this entire sequence is repeated again, S will be mapped back onto itself - effectively realising a unitary operation of diagonal form. A numerical solution for the above approach has been obtained and is employed in Seq. 5.7. In total, a phase gate is obtained that works on the complete Hilbert-space including up to 2 phonons. Although the complexity of the new pulse sequence for the Toffoli gate seems to be smaller and the pulse sequence in general less demanding, the performance turned out to be worse than the initially discussed Toffoli gate sequence based on the short phase gate: the obtained process fidelity is 60.9(5)% with a mean gate fidelity of 65(4)% [Data07i]. Of the raw data, 4% are zeros and do not contribute to the Monte-Carlo simulation.

Regarding the error budget, the precision achieved on all experimental parameters has been equal to those discussed in Sec. 5.2.1. It follows that simulations including all error sources do not currently explain the observed infidelity in any of the investigated realisations.

As an alternative to the realisations discussed, the Toffoli operation has been implemented in a photon setup employing a so-called “shortcut through Hilbert-space”. Considering qudits, logical elements such as qubits, yet encoding several states instead of two, it is possible to contract quantum operations such as the Toffoli gate significantly [96]. The publication by Lanyon et al. [97] shows the implementation of a Toffoli gate operation based on photons, 2 CNOT and one phase-gate operation accompanied by single qubit operations. Encoding qudit information in a $^{40}Ca^{+}$ quantum register can be performed by storing additional information in $|D'\rangle = D_{5/2}(m = -5/2)$. The number of pulses (see Ref [96, 97] and Sec. 5.2.1) is very similar to that presented in Seq. 5.6 and requires 3 controlled-phase gate operations. The main deciding

Sequence 5.7 Quantum Toffoli gate based on a multi-phonon phase gate

Rblue(1, 1.5, 1)	# map electronic state of qubit 1 on the motion
Rcar($\frac{1}{\sqrt{2}}$, 1.5, 2)	# map electronic state of qubit 2 on motion
Rblue(1, 0.5, 1)	
Rcar(0.5, 0.5, 3)	# first Ramsey pulse on the target qubit 3
Rblue(1.44945,0,3)	# generalised phase gate on target qubit
Rblue(0.721198,0.630725,3)	
Rblue(1.44945,0,3)	
Rblue(0.721198,0.630725,3)	
Rcar(0.5, 0.5, 3)	# second Ramsey pulse on the target qubit 3
Rblue(1,-0.5,1)	# undo mapping onto the motion
Rblue($\frac{1}{\sqrt{2}}$,0.5,2)	
Rblue(1,0.5,1)	

factor for not implementing this alternative pulse sequence has been the required superposition including the $|D'\rangle$ state which makes the qudit very sensitive to magnetic field noise. With a coherence time of about 10 ms on the $|S\rangle \leftrightarrow |D\rangle$ transition, this would result in an estimated coherence time of about 2 ms on the $|S\rangle \leftrightarrow |D'\rangle$ transition which is only a factor of 2 longer than the full pulse sequence at usual experimental settings. This short coherence time would severely limit the performance of the "short-cut" Toffoli-gate operation which was therefore not implemented.

5.2.5 Mølmer-Sørensen gate

So far the employed techniques have been based on the ideas of Cirac and Zoller [67]: ideally exactly one ion is manipulated at a time while the motion of the ion string serves as a data-bus. In principle this approach allows the implementation of arbitrary quantum computations. However, the experiments presented above demonstrate the high sensitivity of this approach to experimental imperfections. Possible alternatives for entangling operations follow the ideas of Mølmer and Sørensen (MS) [98] which are less sensitive to some of the dominant error sources such as phonon-state initialisation or laser and magnetic field noise. The general idea is to consider the ion string as a harmonic oscillator. The ion string is homogeneously illuminated by a bichromatic light field consisting of $\nu \pm \omega \mp \Delta$, with ν being the $|S\rangle \leftrightarrow |D\rangle$ transition frequency, ω the trap frequency and Δ corresponding to a detuning from the sideband frequencies. The corresponding Hamiltonian describes an off-resonantly driven harmonic oscillator. Following the behaviour of a classical oscillator, the state will evolve along a circle in phase space and return to its initial state after $\tau = 1/\Delta$. In the quantum mechanical case, the motional state of the quantum system will return to its initial state. The logic operation on the quantum register, however, depends on the area enclosed in phase space. The Hamiltonian H is of the form $H \propto (a \exp(i\Delta t) + a^\dagger \exp(-i\Delta t))S_\phi$ where a and $a^\dagger$ represent the annihilation and creation

operator for motional quanta and $S_\phi = \sum_{k=1}^{N} \sigma_\phi^{(k)}$, with $\sigma_\phi^{(k)} = \sigma_x^{(k)} \cos(\phi) + \sigma_y^{(k)} \sin(\phi)$ defined by the corresponding Pauli operator acting on ion k and ϕ defined by the phase of the light field. After the interaction time $\tau = 1/\Delta$, the operation on the quantum register can be described by an effective unitary

$$U_{\mathrm{MS}} = \exp(-i\,\theta\,S_\phi^2) \tag{5.13}$$

with $\theta = \frac{\eta^2\Omega^2}{\Delta}\frac{1}{\Delta}$. Choosing detuning and light intensity appropriately, this operation can be used to map the initial ground state of the system $|S\ldots S\rangle$ with a single light pulse to a GHZ state of the form $|S\ldots S\rangle + |D\ldots D\rangle$ regardless of the size of the quantum register [59, 99].

The main advantage of the MS interaction compared to the phase gate based on C&Z is the insensitivity of the MS gate operation to the phonon state. The MS interaction performs a circle in phase space, independent of the initial phonon state. While the C&Z phase gate requires sideband cooling to the motional ground state, the MS interaction has been shown to perform adequately on a two-qubit quantum register that has only been Doppler cooled to a mean-phonon number of ≈20 [100]. Additionally the entangling gate operation is insensitive to a large number of experimental imperfections. Addressing the quantum register globally supersedes previous addressed pulses and their corresponding addressing errors; heating rates in the ion trap can be neglected as long as the probability for a heating event during the gate operation is sufficiently low. Additional error sources such as off-resonant excitation are suppressed by amplitude shaping [66, 101] of the laser pulses. For these reasons gate implementations based on the MS interaction are expected to operate at high fidelities. Choosing settings that generate maximally entangled states of the GHZ-class, fidelities of up to 99% have been achieved [59, 99] for two ions after a timescale of roughly 50-100μs, with the main error contribution estimated to be spontaneous decay of the excited state during the detection time. The same gate operation has been investigated with respect to its scalability in an ion-trap based quantum computer, and genuine multi-particle entanglement was shown involving up to 14 ions [59].

At the current stage, no process tomography has yet been performed on the MS interaction. The main reason is that process tomography is currently only feasible for two, at most three, qubits. Already for two qubits, quantum projection noise represents a main limitation should infidelities below 1% be investigated. In order to reduce this problem as much as possible, it would be necessary to perform state verifications by suitable measurements of the expected output state based on previously obtained knowledge (see Fig. 3.3). For three qubits, all relevant parameters of the experiment would need to be kept constant for several hours. Increasing the size of the quantum register up to 14 qubits, which has been performed experimentally, exceeds the possibility for a process tomography from a time-constrained point of view (with 3 seconds per tomography measurement setting, it would take roughly 120 million years to measure one complete dataset) as well as from a computational point of view - the corresponding Choi-Jamiolkowski matrix for the process would involve 28 qubits and thus exceed the possibilities of current computers besides a few, selected super-computers. Therefore the performance of the MS gate is described in terms of achieved parameters for genuinely multi-particle entangled quantum states (see Sec. 6.3.2).

5.2.6 Geometric phase-gate operation

So far the motional state of the ion string has been described by the phonon excitation. However, a description via position and momentum of the ions would also be possible. Considering position and momentum as the axes of a two-dimensional plot, the effect of an MS interaction (an off-resonantly driven oscillator) can be visualised as a circle - the string is excited but returns to its initial state after a time t equal to $1/\Delta$. This visualisation of an operation can be applied to several interactions, as will be shown in the following. Assume that a state depending force excited the ion string and drives the ions off-resonantly. After a certain time t, the ion string will return to its initial quantum state; electronic state as well as phonon state. The accumulated phase depends on the enclosed area in phase space. If the enclosed area differs depending on the state (for instance if a certain state is not affected at all by the interaction), a phase-gate operation has been implemented. Based on the argument of the enclosed area, or geometry, gates of this sort are often referred to as "geometric phase gates".

Given the similarities of the geometric phase gate with the MS interaction, a performance similar to the MS gate is expected. Originally considered for hyperfine qubits and employing a Raman transition [102], the geometric phase gate has been reported to operate at fidelities of up to 97% [102] with two main error sources: off-resonant excitation and magnetic field sensitivity. With a slightly changed approach [103] the same gate operation can also be implemented on a quadrupole transition. A narrow-linewidth laser combined with pulse-shaping [66] should be able to significantly reduce operational errors from off-resonant excitations, while a suitably chosen qubit can render quantum information insensitive to magnetic field fluctuations [104]. This leads to an expected performance considerably higher using quadrupole transitions than previously reported fidelities of 97% using Raman transitions.

Technically, the operation and implementation is very similar to the MS-gate: A bichromatic light field consisting of the two frequencies $\nu \pm \frac{\omega}{2} \mp \Delta$ illuminates the desired section of the quantum register. The off-resonant force returns the quantum state to its initial position in phase-space after $\tau = 1/\Delta$ with an effective unitary U_{geo} acting on the quantum register of the form

$$U_{\text{geo}} \approx \exp(-i\theta S_z^2) \tag{5.14}$$

with $S_z = \sum_{k=1}^{N} \sigma_z^{(k)}$, $\sigma_z^{(k)}$ being the corresponding Pauli operator on ion k and θ an effective rotation angle [103].

The performance of the geometric phase gate is investigated as building block in a CNOT gate operation. While applying the phase gate globally on a two-qubit quantum register, the bichromatic gate is enclosed by two Ramsey pulses acting on the target qubit. Process tomography is performed on the gate operation and a process fidelity of 92.4(8)% is obtained. From this follows a mean process fidelity for Haar-measure distributed quantum states of 94(1)% [41] [Data07g]. Here, 6% of the raw-data do not contribute to the Monte-Carlo simulation. In addition, the CNOT gate operation is employed to generate Bell states. Their fidelity is investigated in Ref. [105] and a state fidelity of 95(1)% [Data07a] is obtained, consistent with the previously mentioned process-tomography investigation.

The infidelity was unexpectedly high and cannot be sufficiently explained. The main error contributions are caused by the laser: With the carrier detuned by half the trap frequency of roughly 1 MHz/2 $\approx$ 500 kHz, the servo-bump of the laser stabilisation circuit happened to coincide with that detuning. Changing laser lock parameters had an effect on the performance of

the geometric gate of a few percent, but could not be investigated quantitatively. The remaining infidelity is contributed to projection noise and addressing errors applied during the Ramsey pulses.

5.3 Optimisation of quantum algorithms

With the availability of global interactions, a paradigm change has been considered: instead of realising logical blocks such as CNOT or Toffoli operations, it may be favourable to directly implement larger unitary blocks of a desired algorithm. With regards to all quantum operations realised so far and their performance, the universal set of quantum gates is chosen to consist of collective X and Y rotations, addressed AC-Stark rotations and the global MS interaction as entangling operation. The goal is to find pulse sequences that correspond to the desired algorithm yet are more efficient to realise. These pulse sequences are derived via techniques presented in the diploma thesis of Volckmar Nebendahl [87].

In analogy to the description in Ref. [87] the employed gates are defined by

$$\begin{array}{ll} \text{Collective local operations:} & X(\theta), Y(\theta) = \exp(i\frac{\theta}{2}S_{x,y}) \\ \text{Single qubit operations:} & Z_i(\theta) = \exp(i\frac{\theta}{2}\sigma_z^{(i)}) \\ \text{Global entangling operations:} & \mathrm{MS}(\theta) = \exp(i\frac{\theta}{4}S_x^2) \end{array}$$

following the implementations discussed in Sec. 4.3, Sec. 5.1, and Sec. 5.2.5. Here the global operation S_x is defined by $S_x = \sum_{i=1}^{N} \sigma_x^{(i)}$ which applies the operation $\sigma_x^{(i)}$ on the complete quantum register consisting of N qubits (and S_y accordingly with σ_y). From these gates logical operations can be realised such as an arbitrary phase gate

$$\begin{pmatrix} 1 & 0 & 0 & 0 \\ 0 & 1 & 0 & 0 \\ 0 & 0 & 1 & 0 \\ 0 & 0 & 0 & \exp(i\phi) \end{pmatrix} = Y(\pi/2).\mathrm{MS}(-\phi/2).Y(-\pi/2).Z_1(\phi/2).Z_2(\phi/2) \tag{5.15}$$

or a partial SWAP gate

$$\begin{pmatrix} 1 & 0 & 0 & 0 \\ 0 & \cos(\phi) & -\sin(\phi) & 0 \\ 0 & \sin(\phi) & \cos(\phi) & 0 \\ 0 & 0 & 0 & 1 \end{pmatrix} = \mathrm{MS}(\pi/2).Z_1(\phi).X(\pi).Z_2(\phi).\mathrm{MS}(\pi/2) \tag{5.16}$$

All necessary operations required in Eq.(5.15) and Eq.(5.16) have been shown to perform at fidelities of about 99% and should therefore result in overall gate fidelities notably higher than 90%.

These two-qubit examples are encouraging, yet do not demonstrate the full power of this approach. The compression possibility becomes more visible when considering three-qubit algorithms such as a recent implementation of a three-qubit quantum error correction algorithm [106]. While the details will be left to the thesis work of Philipp Schindler, the highlights with regards to gate compression will be mentioned here: A decomposition of the unitary operations into logical blocks would require 2 (encode) + 2 (decode) CNOT operations combined

with 1 Toffoli gate operation (error correction; would require another 6 CNOT operations). In contrast to these 10 CNOT operations, the compressed algorithm only requires 4 MS interactions. With regards to the number of pulses, an approach following the ideas of Cirac and Zoller would therefore require about 10×7 pulses (using the short CNOT implementation of Seq. 5.4) compared to 9 pulses in total based on the optimised method [106].

Gate:	Unitary map:	Application example:
H	$\exp(i\frac{\pi}{2}\sigma_x) = \frac{1}{\sqrt{2}}\begin{pmatrix} 1 & i \\ i & 1 \end{pmatrix}$	$\lvert 0\rangle \xrightarrow{\text{H}} \frac{1}{\sqrt{2}}(\lvert 0\rangle + i\lvert 1\rangle)$
CNOT	$\begin{pmatrix} 1 & 0 & 0 & 0 \\ 0 & 1 & 0 & 0 \\ 0 & 0 & 0 & -i \\ 0 & 0 & i & 0 \end{pmatrix}$	$\frac{1}{\sqrt{2}}(\lvert 0\rangle + \lvert 1\rangle) \otimes \lvert 0\rangle \xrightarrow{\text{CNOT}} \frac{1}{\sqrt{2}}(\lvert 00\rangle + i\lvert 11\rangle)$
SWAP	$\begin{pmatrix} 1 & 0 & 0 & 0 \\ 0 & 0 & -1 & 0 \\ 0 & 1 & 0 & 0 \\ 0 & 0 & 0 & 1 \end{pmatrix}$	$\lvert 01\rangle \xrightarrow{\text{SWAP}} \lvert 10\rangle$
Toffoli	$\begin{pmatrix} 1 & 0 & 0 & 0 & 0 & 0 & 0 & 0 \\ 0 & 1 & 0 & 0 & 0 & 0 & 0 & 0 \\ 0 & 0 & 1 & 0 & 0 & 0 & 0 & 0 \\ 0 & 0 & 0 & 1 & 0 & 0 & 0 & 0 \\ 0 & 0 & 0 & 0 & 1 & 0 & 0 & 0 \\ 0 & 0 & 0 & 0 & 0 & 1 & 0 & 0 \\ 0 & 0 & 0 & 0 & 0 & 0 & 0 & i \\ 0 & 0 & 0 & 0 & 0 & 0 & -i & 0 \end{pmatrix}$	$\frac{1}{\sqrt{2}}(\lvert 0\rangle + \lvert 1\rangle) \otimes \lvert 10\rangle \xrightarrow{\text{Toffoli}} \frac{1}{\sqrt{2}}(\lvert 010\rangle - i\lvert 111\rangle)$
MS_x	$\exp(i\frac{\pi}{2}S_x^2) = \frac{1}{\sqrt{2}}\begin{pmatrix} 1 & 0 & 0 & i \\ 0 & 1 & i & 0 \\ 0 & i & 1 & 0 \\ i & 0 & 0 & 1 \end{pmatrix}$	$\lvert 00\rangle \xrightarrow{\text{MS}} \frac{1}{\sqrt{2}}(\lvert 00\rangle + i\lvert 11\rangle)$

Table 5.1: Overview of quantum gates realised and their effects on example states: The Hadamard operation, implemented via a single-qubit $\pi/2$ pulse, is often used to generate an equal superposition between the two states of the qubit. With an additional qubit and the CNOT operation at hand, this superposition on the control qubit may trigger an entangled state. A Toffoli gate operation is similar to the CNOT. However, it only performs a bit-flip if the control qubits are in state $|11\rangle$. The Mølmer-Sørensen interaction acting on two qubits can also generate entanglement, with fidelities currently exceeding most other gate operations.

Chapter 6

Experimental realisation of quantum states

Universal set of quantum gates often only include unitary operations, such as single-qubit operations combined with a CNOT or single-qubit operations combined with the MS interaction. In the setup presented, the quantum register is initialised in the ground state with a fidelity of more than 99% per qubit. Considering the initialised, pure state as well as a universal set of unitary operations, any pure quantum state can be generated. However, creating a specific quantum state with a universal set of quantum operations only may not be the most efficient way for a given system. Considering that only a specific quantum state is to be created, algorithms can be employed that properly function only for a specific input, in our particular case for a register initialised in $|S \dots S, 0\rangle$.

6.1 Bell states

Bell states have been mentioned in Sec. 2 and they represent the archetype of two-qubit entangled quantum states, defined by

$$\begin{aligned} |\phi^{\pm}\rangle &= \tfrac{1}{\sqrt{2}}(|00\rangle \pm |11\rangle) \\ |\psi^{\pm}\rangle &= \tfrac{1}{\sqrt{2}}(|01\rangle \pm |10\rangle). \end{aligned} \tag{6.1}$$

Bell states may be realised by initialising one qubit in an equal superposition of $|0\rangle$ and $|1\rangle$ which serves as control qubit during a CNOT operation acting on a target qubit, initialised in either $|0\rangle$ or $|1\rangle$. Depending on the phase of the superposition of the control qubit as well as the state of the target qubit, any of the four Bell states can be generated (see also Sec. 5.2.1).

In an ion-trap based quantum computer there exists a faster algorithm to realise Bell states. The idea can be understood as follows: Consider the quantum state $|DD, 1\rangle$. Illuminating each ion equally strongly on the blue sideband, the phonon excitation will be used to flip either the first or the second qubit with equal probability. This leads to the quantum state $|SD, 0\rangle \pm |DS, 0\rangle$. Using an optional bit-flip operation on either of the two qubits allows one to realise any of the four Bell states. Considering only addressed single-qubit operations at the moment, this algorithm can be implemented as follows: The initial quantum state $|SS, 0\rangle$ can be mapped onto $|DD, 1\rangle$ via a π carrier-pulse on one ion combined with a subsequent π pulse on the blue

sideband of the other ion. A $\pi/2$ pulse on the blue sideband of the first qubit maps the state onto $\frac{1}{\sqrt{2}}(|DD,1\rangle + |DS,0\rangle)$. A follow-up π blue-sideband pulse on the second qubit maps the quantum state onto $\frac{1}{\sqrt{2}}(|SD,0\rangle + |DS,0\rangle)$. This sequence can be simplified by contracting the first π pulse on the blue sideband and the subsequent $\pi/2$ blue-sideband pulse into a single laser pulse as shown in Seq. 6.1. The phase of the third laser pulse allows one to decide whether to generate $|\psi^+\rangle$ or $|\psi^-\rangle$, while an optional addressed carrier π pulse on either of the ions can be used to map $|\psi^\pm\rangle \leftrightarrow |\phi^\pm\rangle$. This sequence has been used as a starting point to investigate quantum teleportation [19] and quantum entanglement swapping [107], yielding fidelities of about 96%.

Sequence 6.1 Bell state creation in an ion-trap quantum computer

Rcar(1,0,2)	# $\|SS,0\rangle \rightarrow |DS,0\rangle$
Rblue(1/2,0,1)	# $\rightarrow \frac{1}{\sqrt{2}}\|D\rangle \otimes (|S,0\rangle + |D,1\rangle) = \frac{1}{\sqrt{2}}(|DS,0\rangle + |DD,1\rangle)$
Rblue(1,1,2)	# $\rightarrow \frac{1}{\sqrt{2}}(|DS\rangle + |SD\rangle) \otimes |n=0\rangle$

6.2 W-states

The idea of distributing one phonon along a two-qubit register to induce bit flips for the generation of Bell states can be generalised to W-states. Again, the principle relies on generating the state $|D\ldots D,1\rangle$ followed by illumination of the blue sideband that, at most, should induce one bit flip. Not knowing where the bit flip has occurred, this will effectively generate a W-state. This procedure can be implemented in two ways: using addressed single-qubit blue sideband pulses, as explained in Sec. 6.2.1 [20], or by homogeneously illuminating the complete quantum register on the blue sideband, see Sec. 6.2.2.

6.2.1 Creation via single-qubit addressing

One possible way to create an N-qubit W-state of the form

$$|\psi_W^N\rangle = \frac{1}{\sqrt{N}}(|D\ldots DS\rangle + |D\ldots DSD\rangle + \ldots + |DSD\ldots D\rangle + |SD\ldots D\rangle) \tag{6.2}$$

follows the idea introduced in Sec. 6.1 by generating one phonon shared by all ions and subsequently perform phonon-controlled bit-flip operations. This can efficiently be implemented by creating the state $|SD\ldots D,0\rangle$ and subsequent blue sideband laser pulses on individual ions as shown in Seq. 6.2.

This sequence has been employed on up to 8 qubits. Using state tomography, the obtained data has been investigated and the fidelity between the generated and desired quantum state has been determined. Here, the overlap with the desired quantum state is improved by allowing for local phase rotations on each qubit, compensating for magnetic field gradients along the ion string. For {3,4,5,6,7,8} ions, the achieved phase-optimised fidelities (in %) have been reported to be {82.4, 84.6(11), 75.9(7), 78.8(5), 76.3(3), 72.2(1)} [20]. These fidelities in the 80% regime are encouraging, yet do not necessarily proof N-particle entanglement. Using a witness

Sequence 6.2 W-state generation based on single-qubit pulses

$\prod_{k=1}^{N-1}$ Rcar(1,0,k)	$\# \rightarrow \|SD\ldots D,0\rangle$
Rblue($\frac{2}{\pi}$ arccos($1/\sqrt{N}$),0,N)	$\# \rightarrow \frac{1}{\sqrt{N}}\|SD\ldots D,0\rangle + \frac{\sqrt{N-1}}{\sqrt{N}}\|DD\ldots D,1\rangle$
Rblue($\frac{2}{\pi}$ arcsin($1/\sqrt{N-1}$),0,N-1)	$\# \rightarrow \frac{1}{\sqrt{N}}(\|SD\ldots D,0\rangle + \|DSD\ldots D,0\rangle)$
	$\#\quad + \frac{\sqrt{N-2}}{\sqrt{N}}\|DD\ldots D,1\rangle$
Rblue($\frac{2}{\pi}$ arcsin($1/\sqrt{N-2}$),0,N-2)	
...	
Rblue($\frac{2}{\pi}$ arcsin($1/\sqrt{1}$),0,1)	$\# \rightarrow \|\psi_W^N\rangle \otimes \|n=0\rangle$

$\mathcal{W}$ optimised for the quantum state at hand [20, methods section], N-particle entanglement is investigated by determining the expectation value $\mathrm{Tr}(\mathcal{W}\rho)$ for the obtained density matrices. The values for {3,4,5,6,7,8} qubits are {-0.532, -0.460(31), -0.202(27), -0.271(31), -0.071(32), -0.029(8)} from which full N-particle entanglement within at least 2.2 standard deviations can be concluded, equivalent to a confidence in full N-particle entanglement of above 98.6%.

In contrast to previously discussed error sources such as off-resonant excitations, frequency, magnetic-field and intensity fluctuations, for this algorithm one of the main concerns is the state initialisation. The algorithm relies, besides ground-state initialisation of the centre-of-mass mode, on all qubits starting in $|S\rangle$ =$S_{1/2}$(m=-1/2). Pumping into this state works with a reliability of above 99% per qubit, yet its failure starts to contribute as a major error source for as many as eight qubits. The implemented quantum algorithm has therefore been slightly modified by two extra pulses in the beginning of Seq. 6.2. After ground-state cooling, the quantum register is mapped from $|S\ldots S,0\rangle$ into $|D\ldots D,0\rangle$. Probing the quantum state on the $S_{1/2} \leftrightarrow P_{1/2}$ at this point yields the information whether the quantum state has been correctly initialised iff no photons are scattered. An additional carrier π pulse on qubit N leads to the same quantum state as presented in the first line in Seq. 6.2. The additional probe on the state initialisation was used to preselect the obtained data and discarded up to 30% of the data [20]. This value is higher than an estimated initialisation error of about 9% due to an optical pumping efficiency into $S_{1/2}$(m=-1/2) of about 99% per ion [Data07b]. The remaining initialisation error is contributed by the fidelity of the employed π pulses and their addressing errors.

6.2.2 Realisation via the superposition principle

Following the idea of distributing the phonon excitation over the quantum register, the global beam can be used to directly generate W-states. A three-pulse sequence initialises the quantum register in state $|D\ldots DS,0\rangle$ (see Seq. 6.3). A single blue-sideband pulse on the first qubit maps the quantum register onto the required state $|D\ldots D,1\rangle$. Instead of subsequently distributing the phonon excitation along the quantum register as in Seq. 6.2.1, a global beam resonant with the blue sideband[1] directly generates a W-state. This can also be understood from the superposition principle: One phonon can at most result in one bit-flip from $|D,1\rangle \rightarrow |S,0\rangle$. Employing the global beam, it can not be predicted which qubit will be flipped. This results in a coherent superposition of all possible outcomes of a single bit flip acting on the state $|D\ldots D\rangle$

[1] Notice that the sideband Rabi time is smaller by a factor $\sqrt{N}$ for global addressing compared to single-qubit illumination.

- the desired W-state $|\psi_W^N\rangle$. The advantage of this procedure, compared to an implementation based on quantum gates such as CNOT operations, is its scalability towards larger systems. The pulse sequence presented in Seq. 6.3 remains constant regardless of the size of the quantum register.

Sequence 6.3 W-state generation employing the global beam

Rcar(1/2,0,g)	
Rzred(1,0,1)	
Rcar(1/2,0,g)	$\# \rightarrow |D \ldots DS, 0\rangle$
Rblue(1,0,1)	$\# \rightarrow |D \ldots D, 1\rangle$
Rblue(1,0,g)	$\# \rightarrow |\psi_W^N\rangle$

This pulse sequence has been implemented on two and four qubits, yielding fidelities of 90(2)% for two [Data08] and 88(1)% for four qubits [Data10c]. Of the investigated raw data 5% and 13% are zeros and do not contribute to the 1000 sample Monte-Carlo simulation for the derived error bars. A similar approach has been published by the group of David Wineland, yielding a fidelity of 77(2)% for two qubits [108].

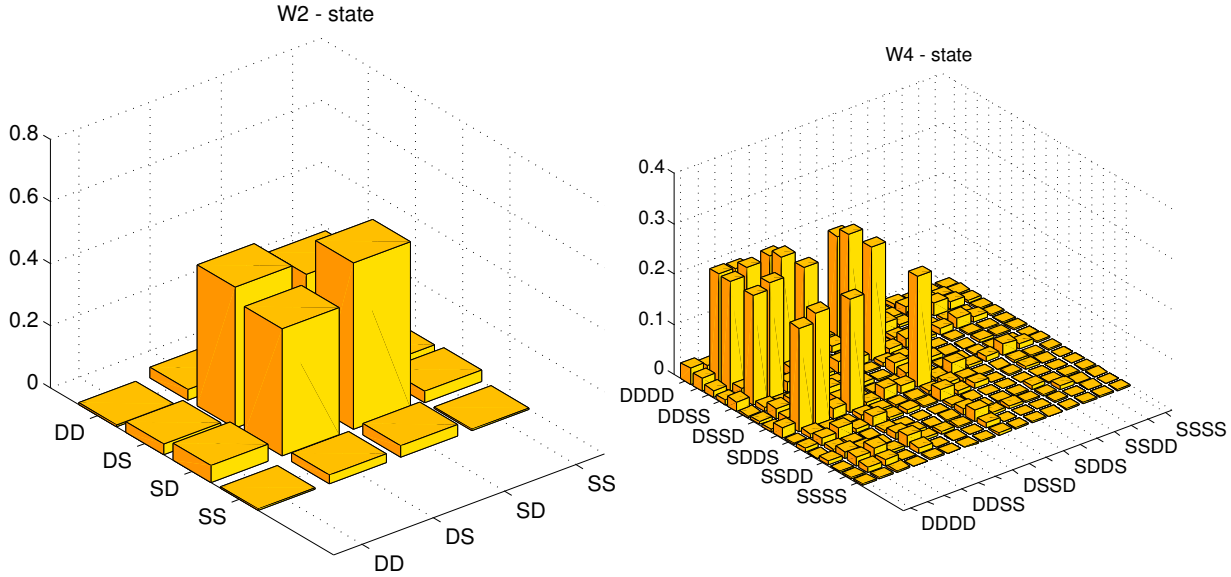

Figure 6.1: W-state of two and four qubits generated via global illumination: Employing Seq. 6.3 on two qubits a W- or Bell state is generated. State tomography yields a fidelity of 90(2)%, with the absolute values of the density matrix shown on the left. Applying the very same sequence on four qubits, a fidelity of 88(1)% has been achieved - the absolute values of the derived density matrix is shown on the right.

6.3 Greenberger-Horne-Zeilinger states

Besides W-states, Greenberger-Horne-Zeilinger (GHZ) states represent a prominent class of multi-particle entangled quantum states. The state

$$|\psi_{\mathrm{GHZ}}\rangle = \frac{1}{\sqrt{2}}(|S \ldots S\rangle + |D \ldots D\rangle) \tag{6.3}$$

is an exemplary state of the GHZ class. The form of this quantum state makes certain investigations particularly easy. The fidelity only depends on the achieved populations $P(\rho) = \langle S \dots S|\rho|S \dots S\rangle + \langle D \dots D|\rho|D \dots D\rangle$ as well as the coherence $C(\rho) = |\langle S \dots S|\rho|D \dots D\rangle| + |\langle D \dots D|\rho|S \dots S\rangle|$. The fidelity F directly follows as $F = \frac{1}{2}(P + C)$. In the following a procedure will be discussed to efficiently obtain these values independent of the size of the quantum register. In addition to the state fidelity, these values allow one to verify distillability and multiqubit-entanglement of the generated quantum state.

6.3.1 Multiqubit entanglement employing higher vibrational excitations

In Sec. 6.2.1 the initial quantum state $|D \dots D, 1\rangle$ has been considered for the generation of W-states. In a similar way, GHZ states may be generated. Consider an N-qubit quantum register initialised in the state $\frac{1}{\sqrt{2}}|D \dots D\rangle \otimes (|n = 0\rangle + |n' = N\rangle)$. Employing addressed blue sideband pulses as conditional bit-flip operations, the superposition in the phonon bus can be mapped into the GHZ state: the state $|D \dots D, n = 0\rangle$ does not couple at all to the blue sideband and remains unchanged by interactions on the blue sideband while the state $|D \dots D, n' = N\rangle$, for every addressed blue sideband pulse, performs a bit-flip operation accompanied by lowering the phonon number. At the end of the sequence, the N phonons have led to N bit-flip operations i.e. to the state $|S \dots S, n = 0\rangle$. In total, the GHZ state $\frac{1}{\sqrt{2}}(|S \dots S\rangle + |D \dots D\rangle) \otimes |n = 0\rangle$ is generated. The detailed pulse sequence is shown in Seq. 6.4. The performance of this pulse sequence is investigated via state tomography for three and four qubits. The obtained data supports a fidelity of 88.2(6)% for three [Data07h] and 88(1)% for four qubits [Data07e], with 18% or 16% of the respective data being zeros and therefore not contributing to the error estimation via a Monte-Carlo simulation.

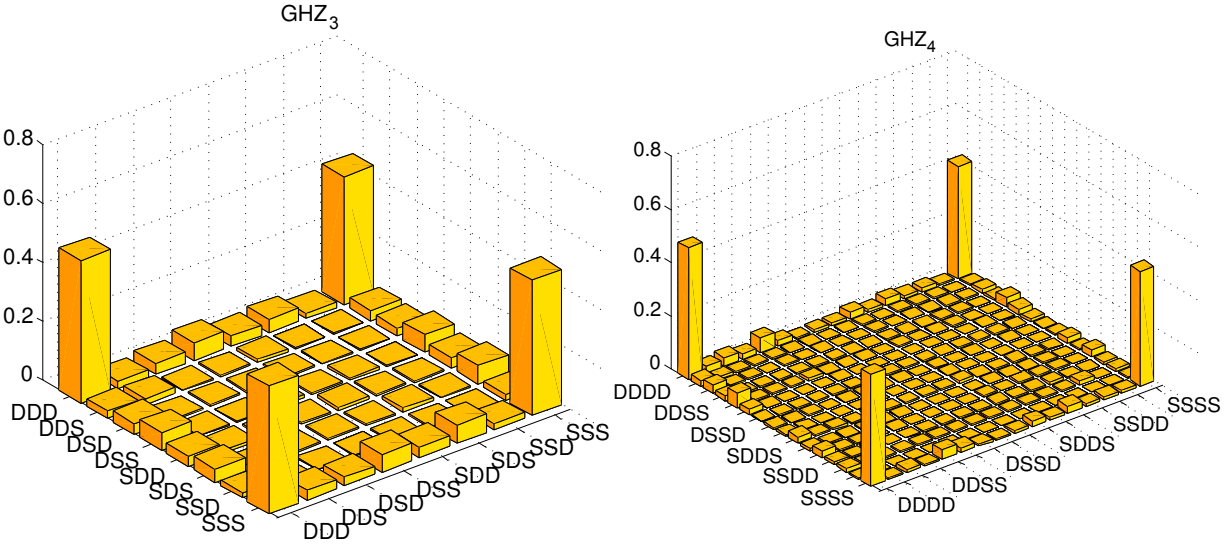

Figure 6.2: GHZ state generation employing higher vibrational modes: The performance of Seq. 6.4 has been investigated with three and four qubits. A fidelity of 88.2(6)% for three qubits and 88(1)% for four qubits has been found. The pictures show the absolute values of the obtained density matrices for three qubits (left) and four qubits (right).

Sequence 6.4 GHZ-state generation using higher vibrational excitations

$\prod_k^{N-1}$ Rcar(1,0.5,k)	# prepare all but one ion in state D
Rblue(0.5,0.5,N)	# create superposition |SD...DD,0>+|D...DD,1>
Rcar2(1,0.5,N)	# hide the state |SD...DDD,0> into |D' D...DD,0>
	# increase the number of motional quanta from 1 to N-1
Rcar(1,0.5,N)	# |D' D...DD,0> + |SD...DD,1>
Rblue(1/$\sqrt{2}$,-0.5,N)	# |D' D...DD,0> + |DD...DD,2>
...	
Rcar(1,-0.5,N)	
Rblue(1/$\sqrt{N-1}$,0.5,N)	# |D' D...DD,0> + |DD...DD,N-1>
$\prod_{k=N-1}^{2}$ Rblue(1/sqrt(k),-0.5,k)	# take out the quanta via the remaining ions
Rcar2(1,-0.5,N)	# unhide Nth ion
Rcar(1,0.5,N)	# create an |SS...S>+|DD...D> state from the above state

6.3.2 Single-step multiqubit entanglement

Sequence 6.4 is already notably more efficient than an application of several CNOT operations yet the number of pulses still scales linearly with the size of the quantum register. In contrast to this algorithm, the MS interaction allows the generation of GHZ states with a single laser pulse, an MS($\pi/2$) operation applied on the state $|S\ldots S\rangle$, independent of the size of the quantum register.

Reconstructing the full density matrix would be ideal for a detailed investigation of the generated quantum states. However, this becomes tedious for more than six or seven qubits. Without any optimisation for the task at hand, quantum state tomography requires 3^N measurement settings, with N being the number of qubits. Assuming 3 seconds for obtaining 100 measurements of the same settings, 8-qubit state tomography requires about 5.5 hours of total measurement time. The very same approach scaled up for 14 qubits would require 5.5 months of constant measurements and highlights the requirement for guided tomographies or tomographies optimised for a specific problem in upcoming experiments.

For GHZ states of the form presented in Eq. (6.3), there exists a procedure for obtaining all the required data necessary to determine the fidelity of the generated quantum state [109]. As mentioned above, the form of the GHZ state only requires one to experimentally determine the populations $P(\rho)$ and their relative coherence $C(\rho)$ of the generated state ρ. These two parameters can be determined with a PMT only and do not require the use of the CCD camera for state detection.

The populations $P(\rho)$ are equivalent to the sum of the probabilities of finding the quantum state either in $|S\ldots S\rangle$ or $|D\ldots D\rangle$. This parameter can directly be obtained by the electron shelving technique. The coherence $|S\ldots S\rangle\langle D\ldots D|$ and $|D\ldots D\rangle\langle S\ldots S|$ is investigated by an interference-type experiment known to as "parity oscillations" [109]. Here, an N-qubit

2 qubits (general):	$\mathcal{P}(\phi) = 2\,\{-a_{1,4}\ \cos(2\phi - \alpha_{1,4}) + a_{2,3}\ \cos(\alpha_{2,3})\}$
2 qubits (GHZ):	$\mathcal{P}(\phi) = -2\ a_{1,4}\ \cos(2\phi - \alpha_{1,4})$
3 qubits (general):	$\mathcal{P}(\phi) = 2\,\{-a_{1,8}\ \sin(3\phi - \alpha_{1,8}) + a_{2,7}\ \sin(\phi - \alpha_{2,7})$ $+a_{3,6}\ \sin(\phi - \alpha_{3,6}) + a_{4,5}\ \sin(\phi + \alpha_{4,5})\}$
3 qubits (GHZ):	$\mathcal{P}(\phi) = -2\ a_{1,8}\ \sin(3\phi - \alpha_{1,8})$
4 qubits (general):	$\mathcal{P}(\phi) = 2\,\{a_{1,16}\ \cos(4\phi - \alpha_{1,16}) - a_{2,15}\ \cos(2\phi - \alpha_{2,15})$ $-a_{3,14}\ \cos(2\phi - \alpha_{3,14}) + a_{4,13}\cos(\alpha_{4,13}) - a_{5,12}\ \cos(2\phi - \alpha_{5,12})$ $+a_{6,11}\cos(\alpha_{6,11}) + a_{7,10}\cos(\alpha_{7,10}) - a_{8,9}\ \cos(2\phi + \alpha_{8,9})\}$
4 qubits (GHZ):	$\mathcal{P}(\phi) = 2\,\{a_{1,16}\ \cos(4\phi - \alpha_{1,16})$

Table 6.1: Expected parity signals $\mathcal{P}$ as a function of ϕ for (general) N-qubit density matrices as defined in Eq. (6.4) as well as an N-qubit (GHZ) state.

density matrix of the form

$$\rho = \begin{pmatrix} a_{1,1} & e^{i\alpha_{1,2}}\ a_{1,2} & \dots & e^{i\alpha_{1,2^N-1}}\ a_{1,2^N-1} & e^{i\alpha_{1,2^N}}\ a_{1,2^N} \\ \vdots & & \ddots & & \vdots \\ e^{i\alpha_{2^N,1}}\ a_{2^N,1} & e^{i\alpha_{2^N,2}}\ a_{2^N,2} & \dots & e^{i\alpha_{2^N,2^N-1}}\ a_{2^N,2^N-1} & a_{2^N,2^N} \end{pmatrix} \tag{6.4}$$

is subject to a global rotation $\mathrm{Rcar}(1/2, \phi, g)$. The output state populations are combined in terms of its parity - the probability of finding populations with an even number of $|0\rangle$ minus the probability of observing an odd number of $|0\rangle$. In that regard, the parity is equal to the expectation value of the operator $\prod_{i=1}^{N} \sigma_z^{(i)}$. For varying ϕ the parity $\mathcal{P}$ of an N-qubit GHZ state ideally oscillates N-times faster than ϕ. This is shown for arbitrary density matrices of 2 to 4 qubits in Tab. 6.1. Tab. 6.1 also shows that, besides the coherence of the GHZ state, several additional elements of the density matrix can be derived from such a procedure. Fitting $C * \cos(N * \phi + \phi_0)$ to the observed parity oscillations directly returns the coherence of the quantum state. Combined with the previously obtained populations, the fidelity of the quantum state with respect to an N-qubit GHZ state can be calculated.

This approach to investigating GHZ states is advantageous in our apparatus compared to a complete state tomography:

- The GHZ-population $P(\rho)$ can directly be obtained from the PMT signal.
- The operation $\mathrm{Rcar}(1/2, \phi, g)$ is straightforward to implement using the global beam and consists of a single laser pulse regardless of the number of qubits.
- The phase of the probe light field can be effortlessly changed by the phase of the employed radio frequency.

- The parity signal can be directly inferred from the PMT data. The short detection time makes this measurement less prone to spontaneous decay happening during the measurement process and yields higher confidence in the obtained data. Calculations on the ideal detection time have been performed by Koenraad Audenaert and can be found in Appendix B.
- For a given total measurement time, these few parameters can be determined with higher precision than when using a full state tomography.
- In total, the effort required to investigate a GHZ state remains small compared to a full tomography and scales linearly for an increasing number of qubits.

All parameters are determined by photon counting with the PMT and interpreted as follows: The electron shelving technique [17] scatters photons from the atoms, which are detected and counted[2] with a rate R ($\approx$ 50 kcounts/s) for each ion in state $|S\rangle$ over a detection time τ ($\approx$ 3-5 ms) at the PMT. The detected counts follow a Poisson distributions for mean values of $\mu_n = n \cdot R \cdot \tau$ with $n \in 0, \ldots, N$ the number of qubits in state $|S\rangle$. Ideally, if all ions are found in state $|D \ldots D\rangle$, no photons are detected by the PMT. The dark count rate dk ($\approx$ 1 kcounts/s), however, adds an additional value to the mean values $\mu_n = n \cdot R \cdot \tau + dk \cdot \tau$.

For few qubits, such as the two qubits investigated in Ref. [99], the three Poisson distributions are well separated (see Fig. 6.3(a)). Under this condition, distinct discriminating values can be defined that separate the different excitations with almost unity precision. Consider the Poisson distribution

$$\mathrm{Pois}(x|\mu) = \frac{\mu^x \exp(-\mu)}{x!} \tag{6.5}$$

for mean values $\{\mu_0, \mu_1, \mu_2\}$ = {2,102,202} (corresponding to a count rate of 50 kcounts/s, a dark count rate of 1 kcounts/s, and a detection time of 2 ms). Consider furthermore that 87 counts were detected in a single experiment. The probability of obtaining the detected 87 counts for the above mean values is $\{7{\cdot}10^{-106}, 1, 2{\cdot}10^{-18}\}$ (already normalised to one). Considering thresholds set at 50 and 150 counts, the errors are given by the integral of the Poisson distribution outside the barriers, resulting in errors of approximately $\{1{\cdot}10^{-50}, 4{\cdot}10^{-6}, 6{\cdot}10^{-5}\}$.

This approach, while fully acceptable for few ions, results in non-negligible errors when more than 8 ions are investigated (see Fig. 6.3(b)). The Poisson distributions are overlapping and thresholds cannot be set without attributing a significant number of counts to an adjacent excitation. Increasing the detection time would separate the different Poisson distributions more clearly, yet make the measurement prone to spontaneous decay. Calculations show that for count rates of about 50 kc/s the ideal detection time is 3.5 ms for 8 ions and 5 ms for 16 ions (see Appendix B). In this approach, state discrimination between the overlapping Poisson distributions is not performed using the barrier approach presented above but directly follows a Bayesian analysis for Poisson distributions asking the question: How likely is it that a certain state of mean counts μ_i has resulted in the detected counts x? Mathematically, this is described as follows: From a single measurement x counts are obtained. The probability p for these counts to belong to a certain excitation i tied to a mean value of μ_i counts is (in vector form):

$$p(x) = \frac{(\mathrm{Pois}(x|\mu_0), \mathrm{Pois}(x|\mu_1), \ldots, \mathrm{Pois}(x|\mu_N))}{\sum_{i=0}^{N} \mathrm{Pois}(x|\mu_i)} \tag{6.6}$$

[2]National Instruments: NI-6733

which includes the normalisation over all possibilities. Considering M measurements for the same setting (and a list of detected counts x_m), the overall probability vector $p = \underset{M}{\text{mean}}\, p(x_m)$ is defined by the mean value of these probability vectors. Compared to the evaluation using discrete borders on the count rates, this approach acknowledges the probability for a certain number of counts to be generated by any of the possible Poisson distributions.

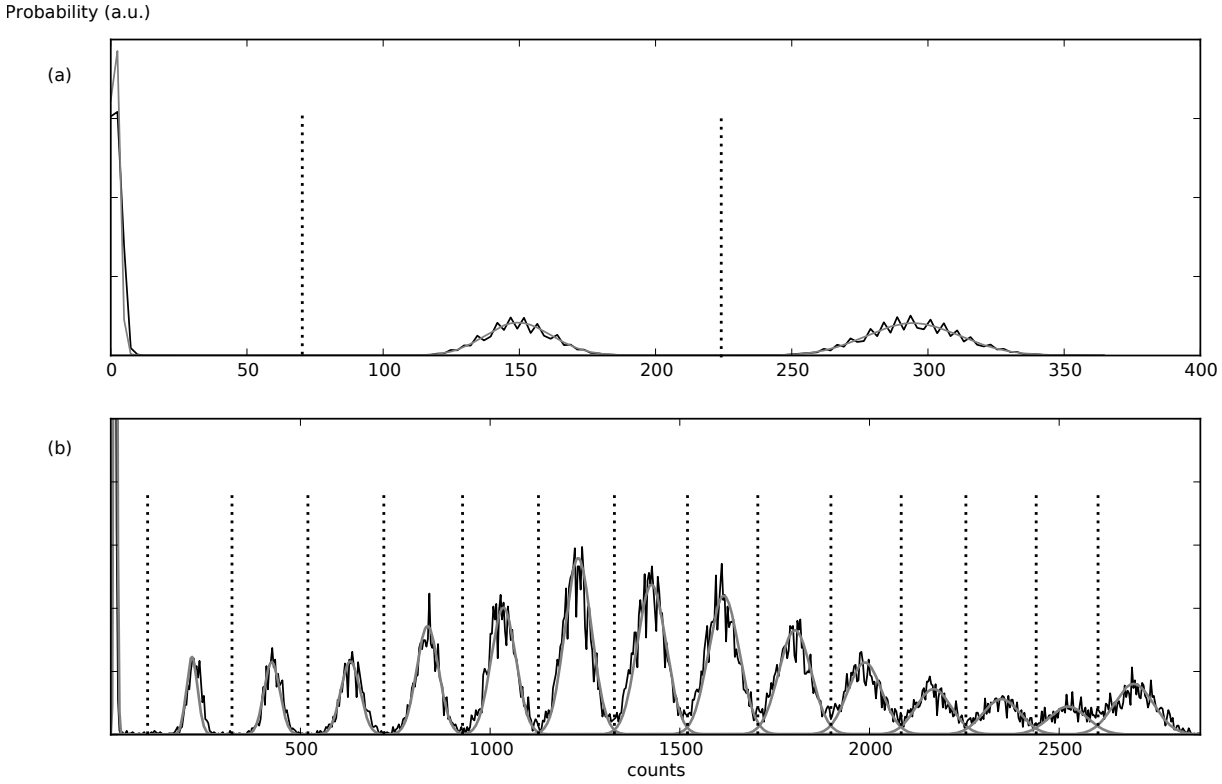

Figure 6.3: Histogram illustrating the distinguishability of detecting the ion string in different quantum states: (a) For two qubits (count rate $\approx$ 50 kc/s, detection time of 3 ms), the Poisson distributions are well separated. This allows us to employ discrete values that distinguish between the different excitations with almost unity precision. (b) For an increasing number of ions - as the presented histogram of counts from 14 ions (count rate $\approx$ 50 kc/s, detection time of 4 ms) - two effects become apparent. Firstly, Poisson distributions (for 8 ions and more) begin to overlap significantly. This could be compensated by increasing the detection time which would lead yet to another problem: For an increased detection time, spontaneous emission during the detection may become non-negligible. As a second effect, the mean values of the Poisson distributions are not equally separated due to saturation effects caused by the PMT dead time. The possible location of discriminating values are shown in both cases. Here, (b) illustrates that the discrimination approach will incorrectly assign a non-negligible number of measurements to a higher or lower excitation.

Using this approach, GHZ-populations are obtained the following way: After the GHZ-state is generated using a MS($\pi/2$) pulse, the populations are investigated via electron shelving. The GHZ-populations follow as

$$P(\rho) = \langle S \dots S|\rho|S \dots S\rangle + \langle D \dots D|\rho|D \dots D\rangle = \underset{x}{\text{mean}} \frac{\text{Pois}(x|\mu_0) + \text{Pois}(x|\mu_N)}{\sum_{i=0}^{N} \text{Pois}(x|\mu_i)} \quad (6.7)$$

with x representing all measurements taken.

The coherence of the quantum state is inferred from parity oscillations. Here, the parity

$$\mathcal{P} = \underset{x}{\text{mean}} \frac{\sum_{i\in\text{even parity}} \text{Pois}(x|\mu_i) - \sum_{i\in\text{odd parity}} \text{Pois}(x|\mu_i)}{\sum_{i=0}^{N} \text{Pois}(x|\mu_i)} \tag{6.8}$$

as a function of a set of counts x and the mean values for an even/odd number of excitations/parity μ_i of a N-qubit GHZ-state of the form in Eq. (6.3) oscillates N-times faster compared to the one-qubit case (see Tab. 6.1). The obtained data is therefore investigated with regards to

$$\mathcal{P}(\phi, \{C, \phi_0\}) = C * \cos(N * \phi + \phi_0) \tag{6.9}$$

where $\{\ldots\}$ denotes free parameters and ϕ is set in the experiment. C corresponds to the coherence of the GHZ-state and ϕ_0 represents the phase of the quantum state with respect to the probe light field.

There are several different possibilities to derive estimates of the parameters $\{C, \phi_0\}$ and their corresponding errors. In the following, four evaluation techniques will be discussed: least-squares fitting, weighted-least squares fitting, Bayesian inference based on the assumption of perfect distinguishability of experimental data, and Bayesian inference which takes the Poisson nature of the count rates into account.

An initial attempt to calculate the coherence may be based on a naive *least-squares fit* of $\mathcal{P}(\phi, \{C, \phi_0\})$ with respect to the experimental *mean* parity data $\mathcal{P}(\phi_i)$ (derived from averaging a set of measurements) obtained for the chosen phases ϕ_i

$$C^f, \phi_0^f = \arg\min_{C,\phi_0} \sum_i |\mathcal{P}(\phi_i, \{C, \phi_0\}) - \mathcal{P}(\phi_i)|^2 \tag{6.10}$$

with C^f, ϕ_0^f representing the fitted, most-likely coherence and relative phase. This approach, however, has one shortcoming. The error, or variance, of parameters C and ϕ_0 are obtained from the main diagonal of the covariance matrix. The covariance matrix estimates the change of fitted parameters depending on the uncertainty of the data points. If no weight is defined, the uncertainty is determined by the variance of the residuals between the fit and the data points. Therefore, should the data points happen to be very close or directly on the fitted function, the predicted error will vanish. Additionally, all points are considered to have similar errors and therefore equally contribute to the parameter estimation. With the background of binomially distributed parameters, certain data points may have notably smaller errors which ought to be included in a parameter estimation.

In order to obtain reasonable parameters and error bounds, it is necessary to pursue a *weighted fit* of the data points, with the weights determined by the underlying statistics of the measurement process. Considering the bimodal results (either positive or negative parity), the parity $\mathcal{P} \in [-1, 1]$ can be replaced by the probability $p \in [0, 1]$ for detecting a positive parity. This can also be regarded as a rescaling of the problem from $C * \cos(N * \phi - \phi_0)$ to $\frac{1}{2}(1 + C * \cos(N * \phi - \phi_0))$. Again, the measurement results follow a binomial distribution in sense of "Was a positive parity observed: yes/no?" For a predicted probability p obtained from M measurements, the error is $\Delta p = \sqrt{\frac{p*(1-p)}{M}}$. Therefore, extreme values such as a probability close to 0 or 1 are considerably better determined than probabilities close to 0.5. This

additional information about the precision of the obtained data can be taken into account by weighting each point $p(\phi_i)$ with $w_i = \Delta p(\phi_i)^2$. The accordingly weighted least-squares fit is then

$$C^f, \phi_0^f = \arg\min_{C,\phi_0} \sum_i w_i(|\mathcal{P}(\phi_i, \{C, \phi_0\}) - \mathcal{P}(\phi_i)|^2) = \arg\min_{C,\phi_0} \sum_i \frac{|\mathcal{P}(\phi_i, \{C, \phi_0\}) - \mathcal{P}(\phi_i)|^2}{\Delta\mathcal{P}(\phi_i)^2}. \tag{6.11}$$

This function, although taking into account the precision of the individual data points, has other shortcomings: the weights are based on the assumption that the measured mean parity coincides with the mean parity for an infinite number of measurements. For the case of few measurements or very high coherences it is likely that the experiment suggests a mean parity of either -1 or 1 (or equivalently: a probability of 0 or 1). In this case the weight becomes infinite and the fit procedure fails. It is implausible that a value can be determined with infinite precision with a finite amount of data. This problem of estimating the error for reoccurring measurements has been considered by Laplace in his "Rule of Succession" in 1814 [45]: considering d different possible outcomes of an experiment that was repeated M times, the minimum precision for the different outcomes is $\frac{1}{M+d}$. The least-squares fit can therefore be corrected be a redefinition of the errors for each data point:

$$\Delta p_i = \max\left(\frac{1}{M+2}, \sqrt{\frac{p(\phi_i) * (1 - p(\phi_i))}{M}}\right) \tag{6.12}$$

With this approach, a data analysis has been achieved that is statistically sound with regards to weighting each data point appropriately and obtaining the most likely coherence that can be contributed to the realised GHZ state. A sufficiently large amount of data would have enough statistical scatter and therefore an appropriate error estimation may be inferred.

This leads to a final argument: the complete data analysis so far does not take physical validity of the data into account. The coherence (including its error bar) has to be smaller than twice the geometric mean of $|S \ldots S\rangle\langle S \ldots S|$ and $|D \ldots D\rangle\langle D \ldots D|$. Projection noise may result in data points that suggest a non-physical coherence, for example, that is larger than 1, or breaks one other restriction based on the populations. It is possible to modify the weighted fit to include these restrictions. At this point, however, the complete analysis with its numerous adjustments may be up to a discussion of the following points:

- A normal least-squares fit does not include the information about the error of the different data points.
- A least-squares fit weighted by the projection noise errors may overestimate the precision of the data.
- A least-squares fit weighted by a modified error estimation including Laplace' Rule of Succession may result in unphysical predictions for the coherence and its error compared with the observed populations.
- Unphysical predictions can not be excluded without extensive modifications to the fit routine.

The third evaluation method follows the ideas of a *Bayesian analysis* (see Sec. 3.1.3) and pursues an alternative approach: For perfectly distinguishable results, the probability distribution function $\beta(p, \mathfrak{P}, M)$ (see Eq. 3.8)

$$\beta(p, \mathfrak{P}, M) = \left(\begin{array}{c} M \\ \mathfrak{P} \end{array} \right) p^{\mathfrak{P}} \, (1-p)^{M-\mathfrak{P}} \tag{6.13}$$

provides the likelihood that a probability p was responsible for the obtained $\mathfrak{P}$ results (of a bimodal reply from an experiment such as the investigated parity) when M experiments are performed. For K obtained parity data $\mathfrak{P}(\phi_j)$ at the different chosen phases ϕ_j with M measurements each, the fit function from Eq. 6.9 is regarded as a two parameter Bayesian investigation for the coherence C and relative phase ϕ_0

$$\mathcal{B}(C, \phi_0) = \prod_{j=1}^{K} \beta(\frac{1}{2}(1 + C\cos(N * \phi_j + \phi_0)), \mathfrak{P}(\phi_j), M) \tag{6.14}$$

The function $\mathcal{B}(C, \phi_0)$ includes all information about the obtained data and describes how likely the combination of a coherence C and a relative phase ϕ_0 is for delivering the obtained data. Numerically $\mathcal{B}(C, \phi_0)$ is investigated for a 2-dimensional grid of coherences, with coherences C_j between zero and the physically motivated maximum coherence provided by the geometric mean of the according populations $C_{\max} = 2\sqrt{\langle S \ldots S|\rho|S \ldots S\rangle \cdot \langle D \ldots D|\rho|D \ldots D\rangle}$, and phases $0 \leq \phi_j \leq 2\pi$. Normalised to one, this grid can be used to derive the probability distribution function of the coherence $\mathrm{Tr}_{\phi_0}(\mathcal{B}(C, \phi_0))$ and phase $\mathrm{Tr}_C(\mathcal{B}(C, \phi_0))$. Here, $\mathrm{Tr}_{\phi_0}(\mathcal{B}(C, \phi_0))$ describes the probability that a coherence C may lead to the observed data. The describtion in terms of a probability distribution function is similar to the distribution of continous variables: The averaged coherence consistent with the obtained data is

$$\bar{C} = \int_0^{C_{\max}} \mathrm{d}C \; C \; \mathrm{Tr}_{\phi_0}(\mathcal{B}(C, \phi_0)) \tag{6.15}$$

and the standard deviation is then given by

$$\Delta C^2 = \int_0^{C_{\max}} \mathrm{d}C \; (C - \bar{C})^2 \; \mathrm{Tr}_{\phi_0}(\mathcal{B}(C, \phi_0)) \tag{6.16}$$

The calculation of ϕ_0 and $\Delta\phi_0$ follows the same route as for the coherence C. At first glance this may seem to produce the very same results as the corrected weighted least-square fit discussed above. However, there are numerous differences:

- Data points are taken as a list of events and not interpreted as mean value. This acknowledges finite weights for each data point for a finite total number of measurements (in contrast to weighted fits that required adding Laplace's Rule of Succession).
- The weighted fit as well as the Bayesian approach both predict the same most-likely coherence. However, the *mean* coherence is only equal to the most-likely coherence if the probability distribution function is symmetric. Especially for cases close to the border of the investigated coherences (such as high fidelity GHZ states) this may not be the case.

- The error bar of the coherence, ΔC, takes into account the probability that other coherences may be responsible for the obtained data. Even if the obtained data fully lies on the "fitted" curve, the error bar is non-zero for a finite amount of data - in contrast to a standard least-squares fit.

In the *fourth method* based on Bayesian analysis including the Poison statistics of the measured counts, the evaluation is taken one step further by dropping the assumption that one measurement can be perfectly assigned to a specific quantum state. Poisson statistics of count rates should directly be included in the evaluation with regards to expected mean count rates for different quantum states. This only requires an adjustment in the $\beta(p, f, M)$ distribution function. For M measurements with the same setting and k_i counts obtained with respect to mean values μ_i:

$$\beta(p, k_i, N) = \prod_{i=1}^{M} \frac{p * \mathrm{Pois}(k_i, \mu^{\mathrm{even}}) + (1-p) * \mathrm{Pois}(k_i, \mu^{\mathrm{odd}})}{\mathrm{Pois}(k_i, \mu^{\mathrm{even}}) + \mathrm{Pois}(k_i, \mu^{\mathrm{odd}})} \tag{6.17}$$

with $\mathrm{Pois}(k_i, \mu^{\mathrm{even}}) = \sum_{j \in \text{even excitation}} \mathrm{Pois}(k_i, \mu_j)$ and $\mathrm{Pois}(k_i, \mu^{\mathrm{odd}}) = \sum_{j \in \text{odd excitation}} \mathrm{Pois}(k_i, \mu_j)$ short forms for the probability that measurement of k_i counts can be assigned to an even/odd number of excited ions (and the corresponding parity). For perfect distinguishability Eq. (6.17) turns into Eq. (6.13) except for the factor $\begin{pmatrix} M \\ \mathfrak{P} \end{pmatrix}$ which adds information about all possible combinations of how $\mathfrak{P}$ events can chosen from M measurements.

The difference of the three evaluation techniques described above will be illustrated in the following example based on data taken of a 2-qubit GHZ state: The Poisson distributions are well separated (see Fig. 6.3 (a)) allowing one to use thresholds to distinguish between the quantum states. A least-squares fit is compared with a weighted least-squares fit, including Laplace's Rule of Succession to ensure finite weights of each data point. Error bars result from the diagonal of the covariance matrix of the fit routine. In addition, $\mathcal{B}(C, \phi_0)$ is calculated (as shown in Fig. 6.4) from which $\bar{C}$ and ΔC is derived by tracing out all other parameters and calculating the average and standard deviation. The different results for a 2-qubit GHZ state [Data09k] are shown in Tab. 6.2.

	lsq, {t}	weighted lsq, {t}	Bayesian, {t}	Bayesian, {p}
coherence, %	98.3	100.1	98.3	97.8
coherence error, %	0.8	0.4	0.3	0.3

Table 6.2: Different predictions for the GHZ-coherence of an experimentally investigated two-qubit quantum state depending on the technique employed: least-squares (lsq) and Bayesian fits based on the application of thresholds ({t}) on the counting results, whereas {p} implies an evaluation including the Poisson nature of the count events. Least-squares fit (Eq. (6.10)) and Bayesian inference (Eq. (6.14)) based on the threshold method yield comparable results whereas a weighted fit (Eq. (6.11) including the correction from Eq. (6.12)) indicates a non-physical coherence. If the Poisson nature is included in the calculations (Eq. (6.14) based on Eq. (6.17)), the predicted coherence is slightly smaller than the Bayesian evaluation assuming perfect distinguishability. Interestingly, the Bayesian inference yields similar error estimations as the weighted least-squares fit - hinting at the similar weighting of the data.

From both the parity as well as populations, the fidelity can now be calculated. It should

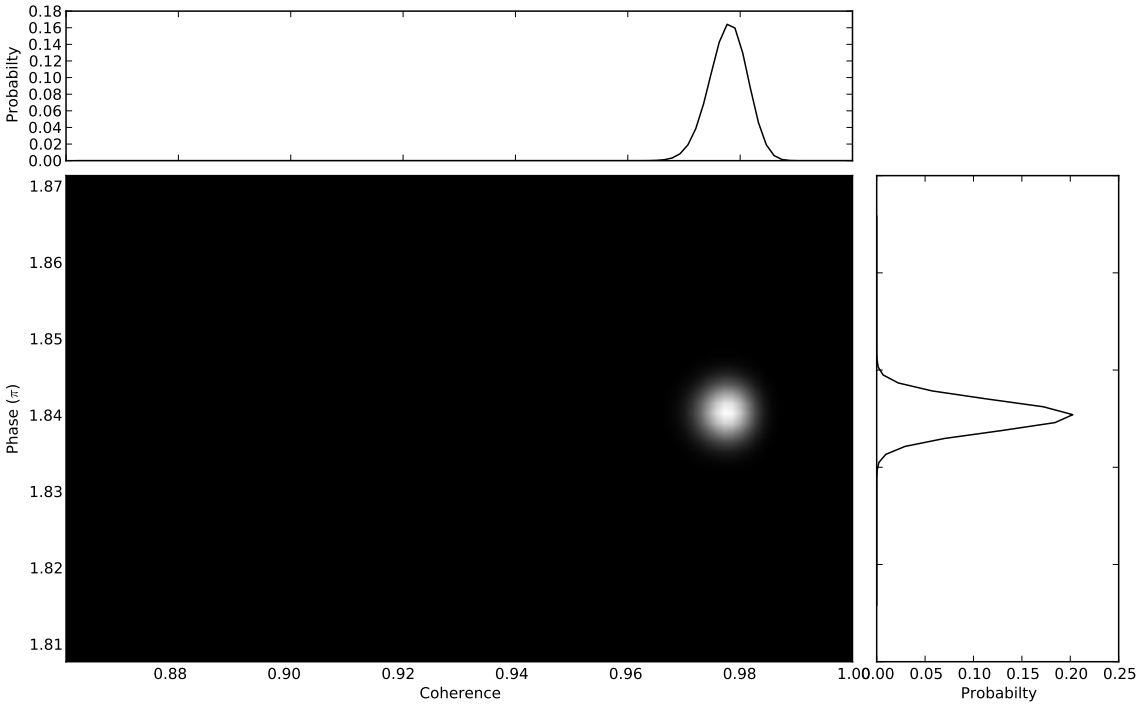

Figure 6.4: $\mathcal{B}(C, \phi_0)$ for two-qubit data: The coherence of a GHZ state is investigated based on Bayesian inference including the Poisson nature of the count events. The centre figure shows the probability for pairs of C and ϕ_0 to generate the obtained data. Tracing out one of the two axis, either the probability distribution for the coherence C (top) or for the relative phase ϕ_0 (right) can be obtained. Mean values and standard deviations are calculated similar to continuous variables (see Eq. (6.15) and Eq. (6.16)).

be noted that the goal of the presented experiments is not only to generate quantum states that are "close" to GHZ states (measured for instance via the fidelity) but also should give clear indication whether multi-particle entanglement has been achieved between all ions or not. The following description and calculations will show how additional statements about the entanglement present in the generated quantum state can be made solely based on the knowledge of the observed coherence and the populations of the different excitations.

The fidelity describes the probability of detecting the desired quantum state for a given density matrix. In that sense, the fidelity does not necessarily prove multi-particle entanglement. Additionally, a quantum state may be multi-particle entangled while also being orthogonal to the desired quantum state. Reference 105 shows that a fidelity larger than 50% is sufficient to claim multi-particle entanglement. However, the confidence in a claim of multi-particle entanglement becomes small when fidelities are close to 50%. Indeed it may not really be necessary to create multi-particle entanglement in every single realisation - it may be sufficient to realise "enough" entanglement in a particular state, generate several copies of it and then use entanglement-distillation procedures [110] to concentrate entanglement in a desired multi-qubit state. Ref. 111 describes in detail a criterion that is compatible with the measurement procedure described above to infer whether a multi-qubit GHZ state may be distilled from (several copies)

of a given state. The idea is roughly outlined in the following: Consider the product state

$$|\psi\rangle_{\text{prod}} = \frac{1}{2}(|0\rangle + |1\rangle) \otimes (|0\rangle + |1\rangle) = |\phi^+\rangle + |\psi^+\rangle. \tag{6.18}$$

The above measurement procedure, however, would only provide information on the populations as well as the coherence of the GHZ state $2|\text{tr}(\rho|00\rangle\langle 11|)|$. The question then is: Can the GHZ coherence be explained by a combination of separable quantum states based on the knowledge of the populations?

Consider the quantum state to belong to the family of states [111]

$$\rho = \sum_{\sigma=\pm} \lambda_0^\sigma |\Psi_0^\sigma\rangle\langle\Psi_0^\sigma| + \sum_{k\neq 0} \lambda_k (|\Psi_k^+\rangle\langle\Psi_k^+| + |\Psi_k^-\rangle\langle\Psi_k^-|) \tag{6.19}$$

where $|\Psi_k^\pm\rangle = \frac{1}{\sqrt{2}}(|k_1 k_2 \dots k_{N-1}0\rangle \pm |\bar{k}_1\bar{k}_2\dots\bar{k}_{N-1}1\rangle)$ with $\bar{k}_i = 0,1$ if $k_i = 1,0$. This particular description can be interpreted as a density matrix consisting to some degree of a coherent GHZ state (described by λ_0^σ) and additional populations (described by λ_k) though without any coherence - in the term $|\Psi_k^+\rangle\langle\Psi_k^+| + |\Psi_k^-\rangle\langle\Psi_k^-|$ populations will add up while the coherence interferes destructively. In this notation, the coherence of the quantum state is given by $\Delta = \lambda_0^+ - \lambda_0^-$. In a similar way the different λ_j can be derived: $2\lambda_j = \langle\Psi_j^+|\rho|\Psi_j^+\rangle + \langle\Psi_j^-|\rho|\Psi_j^-\rangle = \langle j0|\rho|j0\rangle + \langle\bar{j}1|\rho|\bar{j}1\rangle$ with $|j0\rangle = |k_1 k_2 \dots k_{N-1}0\rangle$ and $|\bar{j}0\rangle = |\bar{k}_1\bar{k}_2\dots\bar{k}_{N-1}0\rangle$. According to details outlined in Ref. [111] it follows that if

$$\lambda_k < \frac{\Delta}{2}\,\forall k, \tag{6.20}$$

an N-qubit GHZ state can be distilled from several copies of the investigated quantum state.

Measurements based on counts obtained from a PMT are not able to distinguish between quantum states with an equal number of excited states and accordingly assign all these states to the same excitation. At a first glance this might represent a problem for the above investigation, considering that the individual populations $\langle j0|\rho|j0\rangle$ are not obtained. Nevertheless it is possible to provide a bound on the distillability: Consider all m states $|j_n0\rangle$ with the same number of n excitations (and their m counterparts $|\bar{j_n}1\rangle$) that are detected with a PMT. Eq. (6.20) would result in m inequalities. A PMT measurement would only provide the sum of the investigated populations $\sum_{n=1}^m \langle j_n0|\rho|j_n0\rangle$ (with its counterpart $\sum_{n=1}^m \langle\bar{j_n}1|\rho|\bar{j_n}1\rangle$). This quantity can nevertheless be used in Eq. (6.20) and represents a worst-case scenario (equal to all populations being assigned to a single $|j_n0\rangle$ and its counterpart $|\bar{j_n}1\rangle$).

A similar investigation of the coherence with regards to obtained populations allows one to answer the question whether multi-qubit entanglement has been created in every single realisation. In contrast to Eq. (6.20), derived in Ref. 111, the coherence is not compared with regards to pairs of quantum states $|j_n0\rangle$ and $|\bar{j_n}1\rangle$ but directly with respect to all possible combinations of them. In this sense, Ref. 112 shows that if

$$2|\text{tr}(\langle 0\dots0|\rho|1\dots1\rangle)| > \sum_{k=2}^{2^{N-1}} \sqrt{\rho_{k,k}\rho_{\bar{k},\bar{k}}}, \tag{6.21}$$

with $\rho_{k,k}$ being the kth diagonal element of the density matrix and $\bar{k}$ its conjugate $\bar{k} = 2^N+1-k$, the quantum state is fully N-particle entangled for a GHZ state. The basic idea follows from

providing an upper bound on a coherence given by the geometric mean of the corresponding populations, in this case $\rho_{k,\bar{k}} \leq \sqrt{\rho_{k,k}\rho_{\bar{k},\bar{k}}}$. These coherences may add up to a virtual coherence. If this virtual coherence is smaller than the observed GHZ coherence, multiqubit entanglement can be inferred. Again, data based on PMT measurements are not able to directly infer the required populations $\rho_{k,k}$ but rather the populations of all states with an equal number of excitations. These summed populations can nevertheless be employed in Eq.(6.21) and provide a worst-case criterion for the employed measurement procedure.

Both criteria, distillability and single-shot multiparticle entanglement, are employed in the presented GHZ state evaluation. Based on error propagation the confidence of fulfilling these criteria is provided in units of standard deviations, which can readily be translated into confidence probabilities.

Populations, coherence, fidelity, multi-qubit entanglement and distillability have been investigated for N-particle GHZ-type states generated by the maximally-entangling MS($\pi/2$) interaction. A summary of the obtained parameters for 2 [Data09k], 3 [Data09j], 4 [Data09g], 5 [Data10b], 6 [Data09i], 8 [Data09f], 10 [Data10h], 12 [Data10i] and 14 [Data10d] ions is presented in Tab. 6.5. The fidelities range from 99% for two qubits to about 51% for 14 qubits. Employing the multi-qubit entanglement criterion from Ref. 112, a confidence of 76% can be assigned to creating 14-particle entanglement at every single realisation while distillability of fully entangled multi-qubit states is possible with a confidence of more than 17 σ for all realised states.

With regards to the error budget, the size of the quantum register exceeds the capabilities of all except a few selected classical computers. Therefore it has not been possible to simulate the influence of different error sources on the realised parameters. For 14 qubits, current estimations assign the main errors to state initialisation ($\approx 14\%$), inhomogeneous illumination of the quantum register (no estimate possible) and correlated dephasing. As described in Appendix A, the sensitivity of GHZ states to collective dephasing scales quadratically with the number of qubits [59]. For single-qubit coherence times of about 10 ms, the coherence time of the 14 qubit GHZ state was approximately 50 μs. This value needs to be compared with the time-scale of the entangling MS interaction of about 100 μs which is twice the coherence time of the GHZ state. It seems reasonable to assume that the quantum state strongly dephases - already during its creation.

Ions	2	3	4	5	6	8	10	12	14
Populations, %	99.50(7)	97.6(2)	97.5(2)	96.0(4)	91.6(4)	84.7(4)	67.0(8)	53.3(9)	56.2(11)
Coherence, %	97.8(3)	96.5(6)	93.9(5)	92.9(8)	86.8(8)	78.7(7)	58.2(9)	41.6(10)	45.4(13)
Fidelity, %	98.6(2)	97.0(3)	95.7(3)	94.4(5)	89.2(4)	81.7(4)	62.6(6)	47.4(7)	50.8(9)
Dist. crit. [111], σ	283	151	181	100	95	96	40	18	17
Ent. crit. [112], σ	265	143	167	101	96	92	25	-6	0.7

Figure 6.5: Summary of a GHZ state investigation based on the MS interaction involving 2 to 14 ions [59].

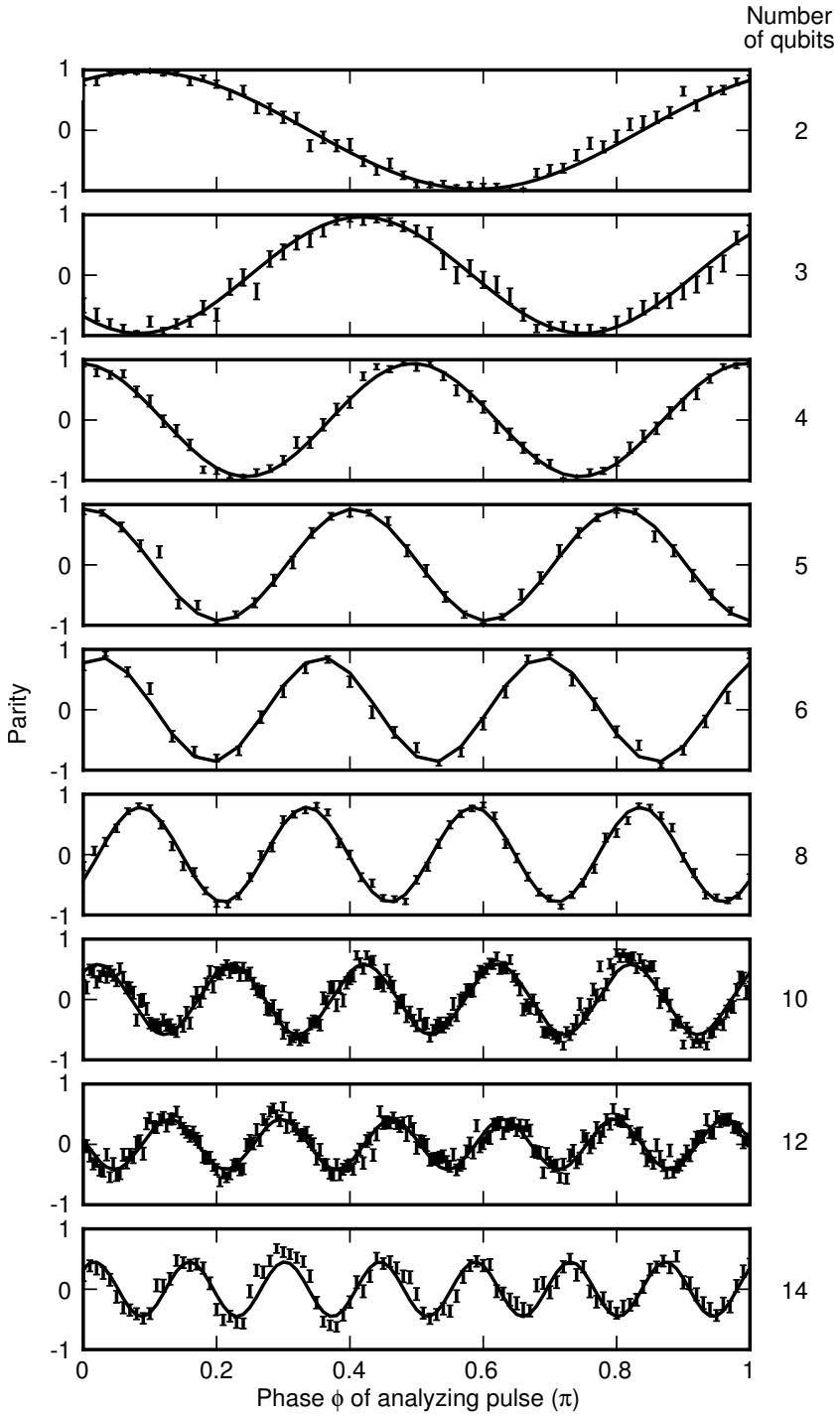

Figure 6.6: Parity signal of {2,3,4,5,6,8,10,12,14} ions. The coherences of the GHZ states range between 98% to 41%. Combined with the populations of the quantum states, all parameters presented in Tab. 6.5 can be calculated.

Chapter 7

Implementation of quantum algorithms

The previous chapters have presented various gate implementations suitable to be combined into a universal set of quantum gates. However, the ultimate goal is not to investigate the performance of individual building blocks of a quantum computer but to combine them and implement complex quantum algorithms. In the following, two different quantum algorithms are presented: deterministic entanglement swapping - an algorithm that is able to create entanglement between non-interacting parties; and the implementation of a controlled-NOT operation within a decoherence-free subspace.

7.1 Deterministic entanglement swapping

Entanglement between two parties is often created by bringing two systems locally close together and having them interact. This approach, however, is not scalable to a large number of distributed quantum registers, especially if the registers are physically separated from each other. Nevertheless is it possible to create entanglement between non-interacting parties. One possible approach is to project entanglement onto the state of two parties using non-local measurements.

Consider two systems consisting of two qubits each: System A will be represented by qubits 1 and 2, while the second system B consists of qubits 3 and 4. Both systems are initialised in a Bell state, specifically $|\psi^-\rangle = \frac{1}{\sqrt{2}}(|01\rangle - |10\rangle)$. The resulting quantum state of the complete Hilbert space $|\Psi\rangle_{1234} = |\psi^-\rangle_{12} \otimes |\psi^-\rangle_{34}$ can be rewritten as

$$|\Psi\rangle_{1234} = -\frac{1}{2}\left(|\phi^+\rangle_{14}|\phi^+\rangle_{23} - |\phi^-\rangle_{14}|\phi^-\rangle_{23} - |\psi^+\rangle_{14}|\psi^+\rangle_{23} + |\psi^-\rangle_{14}|\psi^-\rangle_{23}\right) \tag{7.1}$$

It follows that when measuring qubits {1,4} in the Bell basis, the remaining qubits {2,3} will also be projected into a Bell state. It is important to note that during this procedure there is no interaction between qubits {2,3} at any time - yet, they will be entangled in the end. This does not require local proximity between the remaining qubit pair at any stage of the algorithm and represents a protocol to create entanglement in a network of distributed quantum registers [113, 114].

Several challenges need to be faced before an experimental realisation may be considered. The creation of entangled qubits without direct interaction as indicated in Eq. 7.1 requires a

projective measurement of qubits {1,4} in the Bell basis. For an ion-trap based quantum computer, electron-shelving represents the favoured measurement technique. This, however, is a local projection of the individual qubits and not suitable for measurements in an entangled basis. A solution for this local aspect of measurements in the majority of current ion-trap based quantum computers has been introduced in Sec. 5.2.1 and Eq. 5.4. There, a controlled-NOT operation can be used to entangle qubits and its inverse can be applied to disentangle qubits. Following this line of thought, a CNOT operation can be used to de-entangle qubit pair {1,4} and then measure them locally via electron shelving. In the presented ion-trap based quantum computer, the mapping process is based on the CNOT operation from Seq. 5.4 and returns the quantum state

$$|\Psi_{1234}\rangle = \frac{1}{2}\left(|DD\rangle_{14}|\phi^+\rangle_{23} + e^{i\phi}|DS\rangle_{14}|\phi^-\rangle_{23} - e^{-i\phi}|SD\rangle_{14}|\psi^+\rangle_{23} + |SS\rangle_{14}|\psi^-\rangle_{23}\right) \quad (7.2)$$

with $e^{\pm i\phi}$ and $\phi = \pi/\sqrt{2}$ an additional phase factor obtained from the short phase gate. This additional phase, however, can be ignored in the rest of the sequence as it turns into a global phase after the projective measurement and thus can no longer be detected.

Another challenge apparent in Eq. 7.1 is the non-deterministic aspect of creating entanglement at qubits {2,3}. All four possible measurement results at qubits {1,4} are equally likely. Without any form of selection based on the measurement results, the qubit pair {2,3} will be found in an incoherent superposition of all four Bell states and therefore completely mixed. Ideally a physical realisation takes this problem into account and provides means of correcting the obtained quantum state deterministically into the desired quantum state depending on the measurement result from qubit pair {1,4}. In this particular entanglement-swapping procedure, the reconstruction pulses can be realised by classically controlled X or $Z = XY$ operations, considering that

$$|\psi^-\rangle = \mathbb{1} \otimes Z|\psi^+\rangle = \mathbb{1} \otimes X|\phi^-\rangle = \mathbb{1} \otimes XZ|\phi^+\rangle. \quad (7.3)$$

In combination with Eq. 7.2 one can see that detecting qubit 1 in state $|D\rangle$ requires an additional X-bit-flip to be applied to one of the qubits of pair {2,3}, while detecting qubit 4 in state $|D\rangle$ heralds an additional Z-bit-flip. In our apparatus, state-dependent operations have successfully been implemented in quantum teleportation experiments [19]. State detection requires electron shelving which is applied to the complete quantum register. Considering that only a single qubit should be projected at a time and the remaining qubits, especially {2,3}, ought to remain undisturbed, a π pulse on the $|S\rangle \leftrightarrow |D'\rangle$ transition with $|D'\rangle = \mathrm{D}_{5/2}(m = -5/2)$ is employed to effectively hide the remaining qubits. This encodes quantum information in $\{|D\rangle, |D'\rangle\}$ and renders the qubit insensitive to electron shelving on $S_{1/2} \leftrightarrow P_{1/2}$. The hiding pulses work with a fidelity of better than 99% on the addressed qubit. The overall performance of the hiding (and its inverse) with respect to the entire register is only limited by undesired addressing of neighbouring ions. For our particular implementation, the addressing error was about 3%. Subsequently, 397 nm light illuminates the ion string and the scattered photons, about 50 kc/s per ion being in $|S\rangle$, are counted. In our particular realisation, the ion string is illuminated for 300 μs, resulting in an average number of counts of 16.4 being obtained in case of $|S\rangle$ and 0.4 counts for $|D\rangle$. A Boolean threshold at 5 counts allows us to distinguish between these two states with a confidence of >99%. The Boolean result is stored in a buffer and is later used to trigger the reconstruction pulses. In Seq. 7.1, storing information about a specific qubit is implemented by the command "MBPMDetection(1,300)". Here, the first argument indicates

the buffer where the result is stored and the second argument corresponds to the detection time. Subsequent state-dependent pulses may be triggered depending on the buffer and its value, by the command "MBRcar(buffer, θ, ϕ, ion)" following the same convention as Rcar(θ, ϕ, ion) defined in Seq. 5.1.

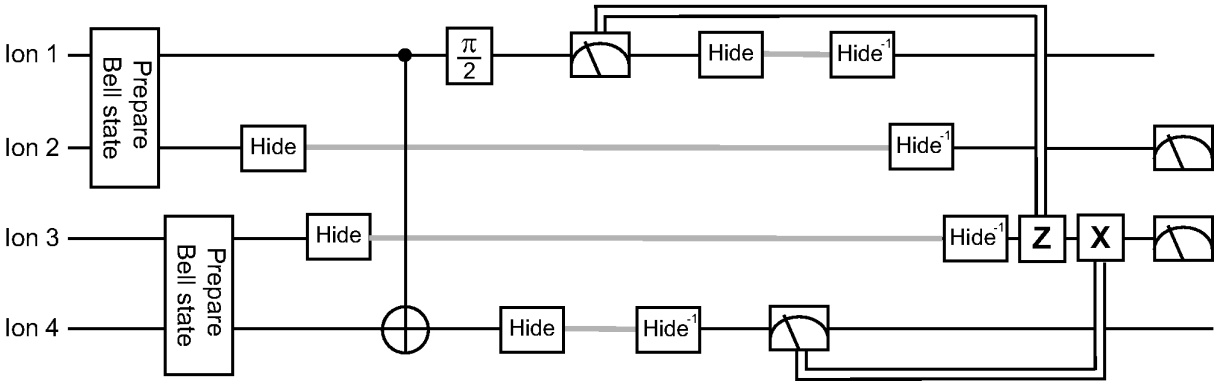

Figure 7.1: Underlying scheme for entanglement swapping in an ion-trap based quantum computer. Two Bell pairs between qubits {1,2} and {3,4} are created. Qubits 2 and 3 are hidden in the $\{|D\rangle, |D'\rangle\}$ manifold from detection light at 397 nm. A CNOT gate operation effectively maps the Bell states into the product basis. Subsequently qubits 1 and 4 are projected. Depending on the measurement result, reconstruction pulses deterministically create the Bell state $|\psi^-\rangle$ at qubits {2,3}.

At this point Eq. (7.1) has successfully been translated into a pulse sequence shown in Seq. 7.1 which is schematically illustrated in Fig. 7.1:

- The initial quantum state $|\Psi\rangle_{1234} = |\psi^-\rangle_{12} \otimes |\psi^-\rangle_{34}$ is created using the pulse sequence discussed in Sec. 6.1.
- A CNOT gate operation based on Seq. 5.4 maps qubits {1,4} from the Bell basis into the product basis.
- Qubits are selectively encoded in the $\{|D\rangle, |D'\rangle\}$ Hilbert-space, making these qubits insensitive to subsequent projective measurements on the entire ion string.
- Bell-measurements are performed in the local basis and, depending on the obtained results, additional operations are performed on the remaining qubit pair.
- State tomography is performed on the complete quantum register to investigate the performance of the implementation.

Without reconstruction pulses, the quantum state of qubits {2,3} is ideally an incoherent mixture of all four Bell states and therefore a completely mixed state. Performing state tomography on the output state of qubits {2,3} without reconstruction pulses applied, we confirm this expectation by obtaining a completely mixed state with 98% [Data07d] fidelity compared with the expected one. Postselecting the data by the measurement results at qubits {1,4}, the very same data should yield the four different Bell states as described in Eq. (7.2). Fig. 7.2 shows the derived density matrices, with fidelities of the density matrix of qubits {2,3} with the expected quantum state defined by the output state of qubits {1,4} being shown in Tab. 7.1.

Sequence 7.1 Pulse sequence for deterministic entanglement swapping

```
Rblue(0.5,0.5,3)                # Bell state prep. 3 & 4
Rcar(1,-0.5,4)
Rblue(1,0.5,4)

Rblue(0.5,0.5,2)                # Bell state prep. 1 & 2
Rcar(1,-0.5,1,1)
Rblue(1,0.5,1)

Rcar2(1,0,2,1)                  # hide ions 2 & 3 to further reduce addressing errors
Rcar2(1,0,3,1)

Rblue(1,0,1)                    # short CNOT: control qubit 1, target qubit 4
Rcar(0.5,-0.5,4)
Rblue(0.5,0.5,4)
Rblue(sqrt(2),0,4)
Rblue(0.5,-0.5,4)
Rcar(0.5,0.5-(2-1/sqrt(2)),4)
Rblue(1,1,1)

Rcar(1,0,2)                     # spinecho pulse on ion 2 & 3 against slow fluctuations
Rcar2(1,0,2)
Rcar(1,0,2)

Rcar(1,0,3)
Rcar2(1,0,3)
Rcar(1,0,3)

Rcar(0.5,-0.5-1/sqrt(2),1)      # additional Hadamard to complete
                                # mapping from Bell basis onto product basis

                                # perform Bell state measurement in unentangled basis
Rcar2(1,0, 4)                   # hide target ion
MBPMDetection(1,300)            # readout control ion
Rcar2(1,0, 1)                   # hide control ion
Rcar2(1,1,4)                    # unhide target ion
MBPMDetection(2,300)            # readout target ion
Rcar2(1,1,1)                    # unhide control ion

Rcar2(1,1,2)                    # unhide the remaining ions
Rcar2(1,1,3)

MBRcar(1,1,0,3)                 # final state reconstruction
MBRcar(1,1,0.5,3)
MBRcar(2,1,0,3)
```

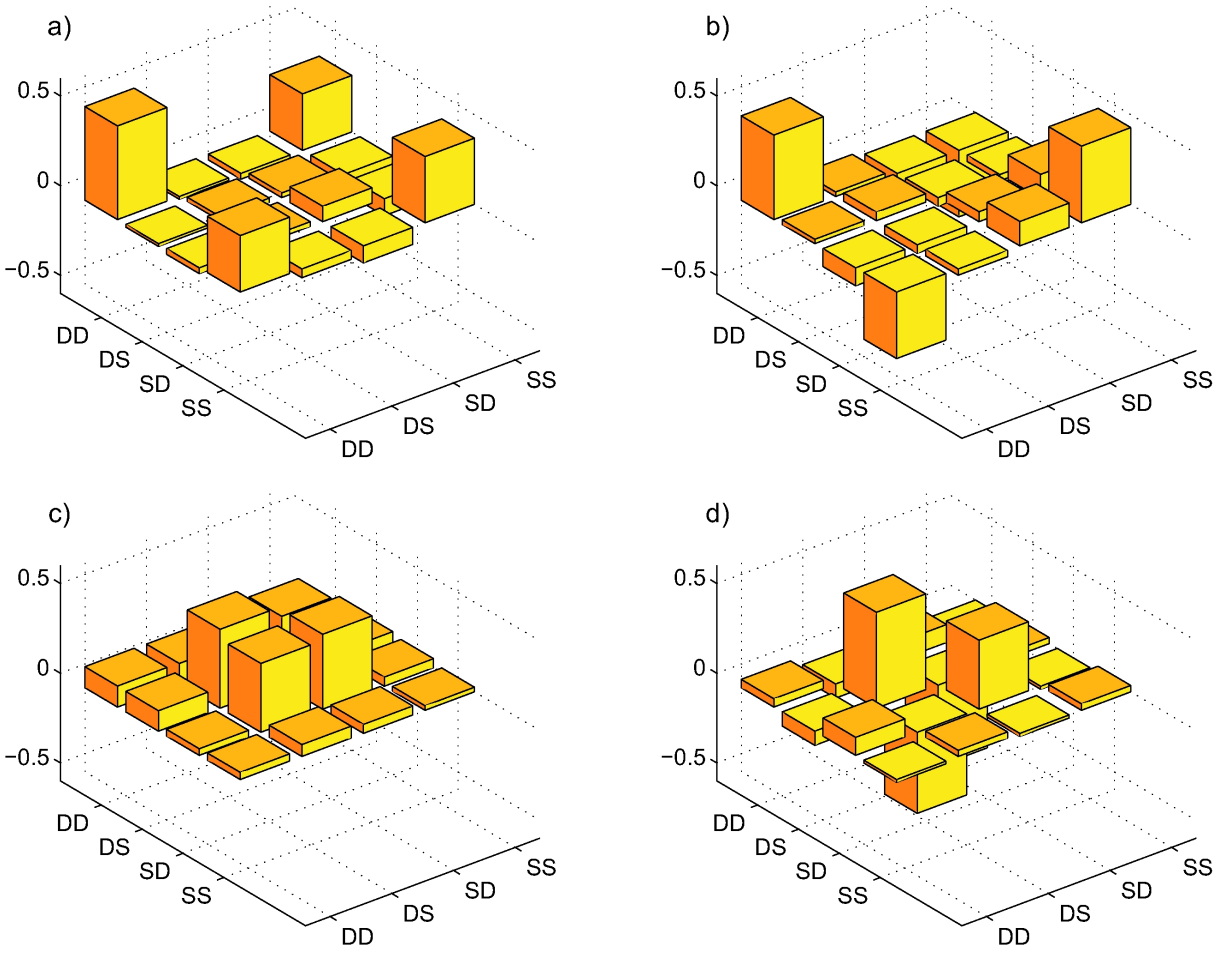

Figure 7.2: Entanglement swapping without reconstruction pulses. Without any postselection, the obtained quantum state shows a fidelity of 98% when compared to a totally mixed quantum state. If the measurement results are sorted by qubits {1,4} into (a)$|DD\rangle_{14}$, (b)$|DS\rangle_{14}$, (c)$|SD\rangle_{14}$, (d)$|SS\rangle_{14}$, quantum state reconstruction yields the four different Bell states $|\phi^+\rangle, |\phi^-\rangle, |\psi^+\rangle, |\psi^-\rangle$ with a mean fidelity of about 82%.

postselected: $\|DD\rangle_{14}$	F(ρ_{23},$\|\phi^+\rangle$) = 76(5)%
postselected: $\|DS\rangle_{14}$	F(ρ_{23},$\|\phi^-\rangle$) = 82(5)%
postselected: $\|SD\rangle_{14}$	F(ρ_{23},$\|\psi^+\rangle$) = 81(5)%
postselected: $\|SS\rangle_{14}$	F(ρ_{23},$\|\psi^-\rangle$) = 91(3)%

Table 7.1: Obtained fidelity of the expected with the detected quantum state as described in Eq. (7.2), postselected by the quantum state of qubits {1,4}.

Applying the deterministic reconstruction pulses [Data07c], the quantum state $|\psi^-\rangle$ is generated with a fidelity of 79(2)%. This number is consistent with the mean fidelity of the postselected data of 82% and suggests a high performance of the deterministic correction pulses. Overall, these fidelities are consistent with the initial Bell-state fidelity of about 96% each and a CNOT gate performance of approximately 93%.

This experiment represents the first realisation of a deterministic entanglement swapping al-

gorithm. All features of entanglement swapping are implemented and tested, deterministically returning entangled states between non-interacting qubits at a fidelity of about 82%. For a scalable, segmented ion trap, a realisation would follow the same procedure, although here qubits {1,4} may be physically separated from qubits {2,3} which currently can not be performed in the presented linear Paul trap.

7.2 Quantum computation in a decoherence-free subspace

One important parameter for quantum computation is the total number of quantum operations that can be applied to a quantum register before its information is lost. Leaving aside limitations by the gate fidelity, the computational power can be estimated by the coherence time divided by the typical duration of an entangling gate operation. In the presented apparatus a coherence time of up to 100 ms has been achieved in comparison to the entangling MS gate interaction that operates at a gate time of about 100 μs. From that follows that algorithms would be limited to about 1000 gate operations - even if the gate operations were perfect. The computational power can be increased by shortening the gate times in addition to increasing the coherence time of the quantum register. For the realisation of faster gates, various approaches are currently investigated [115–117]. On the other hand the coherence time in our ion-trap based quantum computer may be extended by encoding quantum information in decoherence-free subspaces (DFSs) or noiseless subsystems [118, 119]. The idea of decoherence-free subspaces for our system is the following: Realising that each qubit in the quantum register is equally affected by dephasing (in the following referred to as collective dephasing), there exists a subspace of states where all states obtain the same phase. If quantum information is restricted to that subspace, the acquired phase turns into a global phase which does not alter the encoded information:

$$|\phi\rangle = \alpha|0\rangle + \beta|1\rangle \xrightarrow{\text{phase}} \alpha|0\rangle + \exp^{i\phi}\beta|1\rangle \tag{7.4}$$

$$|\psi\rangle_{\text{DFS}} = \alpha|01\rangle + \beta|10\rangle \xrightarrow{\text{phase}} \exp^{i\phi}\alpha|01\rangle + \exp^{i\phi}\beta|10\rangle = \exp^{i\phi}(\alpha|01\rangle + \beta|10\rangle) \tag{7.5}$$

This effect can also be considered from a different point of view: The collective fluctuations of magnetic field and laser frequency induce energy differences between the qubit with respect to the reference. Those relative energy differences, combined with the time that they affect the register, effectively map into phase changes. Quantum states of equal energy, such as $|01\rangle = |DS\rangle$ and $|10\rangle = |SD\rangle$, are still affected, but their *relative* energy difference, which determines the phase evolution, remains unaffected. The approach mentioned above, however, relies on the assumption that phase fluctuations affect the quantum register collectively - each qubit is affected at the same time with equal strength. For the experimental setup here employed there are indications that phase noise is most likely collective along the ion string:

- Any system encoding information in energetically non-degenerate quantum states requires a phase reference to coherently apply quantum operations to the quantum register. In the presented setup, this phase reference is represented by the laser resonant with the $|S\rangle \leftrightarrow |D\rangle$ transition. Any phase or frequency fluctuations on the phase reference will affect the complete quantum register uniformly.

- Degeneracy of the $S_{1/2}$ and $D_{5/2}$ Zeeman manifold is lifted by applying a magnetic field. In our particular case, coils installed in the Helmholtz configuration generate a magnetic field of 3 G at a current of 1.5 A. Considering the size of the coils is about 10 cm, compared to the length of the ion-strings in our experiment of about 20 μm, magnetic field fluctuations based on current fluctuations in the coils are estimated to uniformly affect the quantum register.

While these dephasing processes are present in the majority of current ion-trap quantum computers, they are not necessarily dominant. Sufficiently high control on the laser as well as low-noise current drivers may allow one to realise a system in which the coherence time of a qubit is limited by the lifetime of the exited quantum state[1] and therefore the dephasing process would correspond to uncorrelated phase damping. The presence of dominant, correlated phase noise is verified by creating a quantum state that is insensitive to correlated phase noise and a subsequent investigation of its coherence as a function of time: in the presence of correlated phase noise, states that ought to be insensitive to correlated phase noise ought to show a significantly longer coherence time than sensitive states. This criterion, however, is not sufficient to claim that only correlated phase noise is presented in a give apparatus. A quantum state in the decoherence-free subspace used here is, in theory, totally insensitive, or immune, to correlated phase noise. Spontaneous decay of excited states, if present, ought to be the only source of coherence loss. In that sense, dominant correlated phase noise will be verified by investigating a quantum state that is immune to correlated phase noise and the coherence decay being consistent with a lifetime limitation provided by the number of excited states. In the following the MS gate operation is employed to generate an 8 qubit GHZ state of the form $\frac{1}{\sqrt{2}}(|0\ldots0\rangle+|1\ldots1\rangle)$. This state is highly sensitive to dephasing. However, four additional bit-flip operations create the quantum state:

$$|\mathrm{GHZ}\rangle_8^{\mathrm{DFS}} = \frac{1}{\sqrt{2}}(|00001111\rangle + |11110000\rangle). \tag{7.6}$$

Any correlated phase fluctuations affecting this quantum state turn into a global phase and can not be detected (see Eq. (7.5)). An additional advantage of this state, which is locally equivalent to GHZ states, is the straightforward investigation of its coherence as discussed in Sec. 6.3.2. After creating the quantum state $|\mathrm{GHZ}\rangle_8^{\mathrm{DFS}}$ from a GHZ state, it evolves for a fixed amount of time. Subsequently, four bit-flips map the quantum state back onto a standard GHZ state, whose coherence is then investigated via parity oscillations. The measurement shows that the coherence of $|\mathrm{GHZ}\rangle_8^{\mathrm{DFS}}$ decays with a time constant of 319(75) ms [Data09h] (see Fig. 7.3) which is consistent with lifetime limitations of the quantum state: 1168 ms /4 $\approx$ 290 ms. The storage time of a GHZ state of the form $\frac{1}{\sqrt{2}}(|00000000\rangle + |11111111\rangle)$ of about 150 μs [59] is approximately a factor of 1000 shorter than the coherence time of the locally equivalent decoherence-free state.

The advantages of decoherence-free subspaces have been demonstrated in numerous systems including photons [120, 121], nuclear magnetic resonance experiments [122] and trapped ions [123–125]. However, quantum computation restricted to operations within a DFS are highly demanding and has not been realised until recently [126]. The main challenge is finding a set of operations that can effectively be implemented and, at the same time, constitute a

[1] To be precise, the dephasing time-constant of a lifetime limited qubit is twice the lifetime of the excited state.

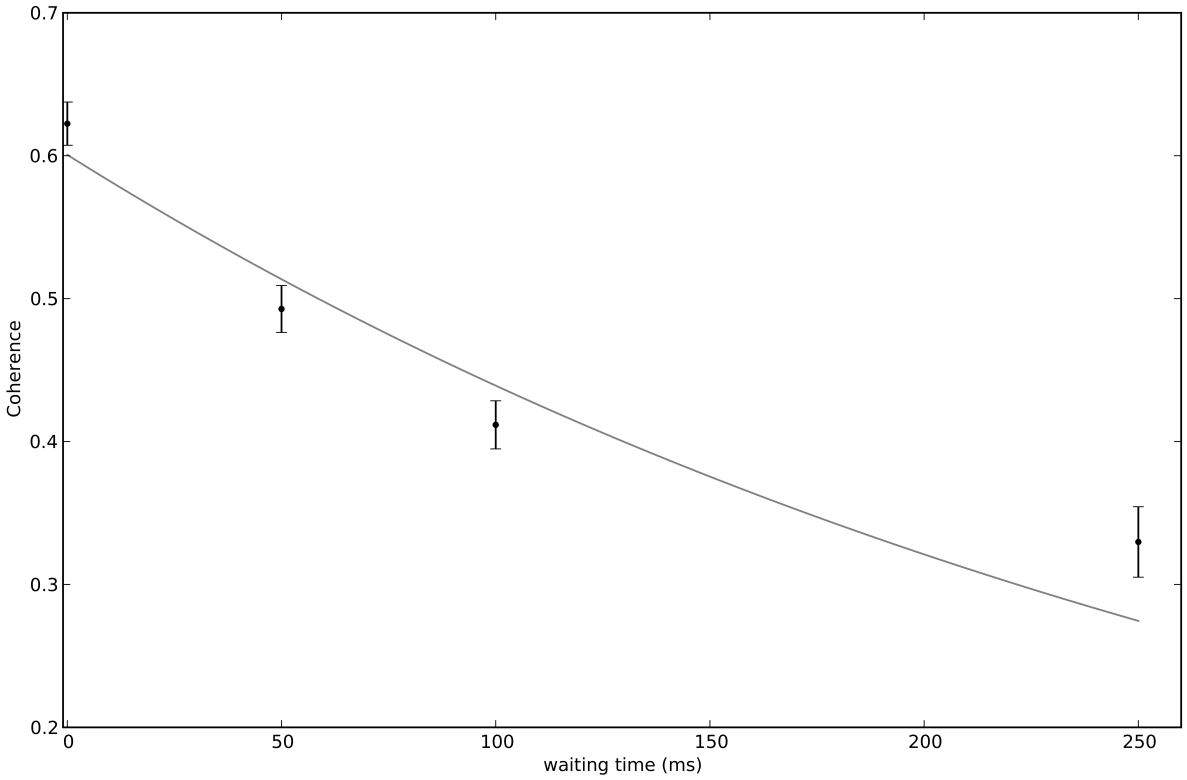

Figure 7.3: Demonstration of a decoherence-free subspace. An eight-qubit GHZ state is mapped into the decoherence-free state $1/\sqrt{2}(|SSSSDDDD\rangle + |DDDDSSSS\rangle)$ with four local bit-flip operations. After a variable waiting-time, the quantum state is mapped back into a GHZ state and investigated as described in Sec. 6.3.2. The obtained coherence follows an exponential decay with a time constant of 319(75) ms, in agreement with lifetime limitations of 1168 ms /4 $\approx$ 290 ms solely based on spontaneous decay of the excited state.

universal set of gates within the chosen noiseless subsystem. In our particular case, quantum information of a single logical qubit is encoded in two physical ions:

$$\begin{aligned} |0\rangle_L &= |1\rangle_P \otimes |0\rangle_P \\ |1\rangle_L &= |0\rangle_P \otimes |1\rangle_P \end{aligned}$$

where the index $L(P)$ denotes the logical (physical) subspace. As mentioned above, both logical states experience the same phase rotation under collective dephasing. Now logical operations can be expressed in physical operations as:

$$\begin{aligned} X_L &= X_P \otimes X_P \\ Z_L &= \mathbb{1}_P \otimes Z_P \text{ or alternatively } Z_P \otimes \mathbb{1}_P \\ Z_L \otimes Z_L &= \mathbb{1}_P \otimes Z_P \otimes Z_P \otimes \mathbb{1}_P \end{aligned}$$

For quantum computation limited to the decoherence-free subspace, this set of quantum operations is universal and can be directly implemented in an ion-trap based quantum computer with the operations presented in Sec. 5: the MS interaction (equivalent to logical X) combined with addressed phase rotations (equivalent to logical Z) allows us to perform arbitrary

single logical-qubit operations; the geometric phase gate (acting as a phase gate in the logical subspace) complements arbitrary single-qubit operations into a universal set of quantum operations. These operations need to be applied pairwise onto ions as illustrated in Fig. 7.4 which requires a reconfiguration of the addressed beam setup. The beam width was increased to illuminate two ions equally while little light is sent to neighbouring ions, resulting in an addressing error of about 5% - again defined by the ratio of the Rabi frequencies of an addressed physical qubit to its neighbours.

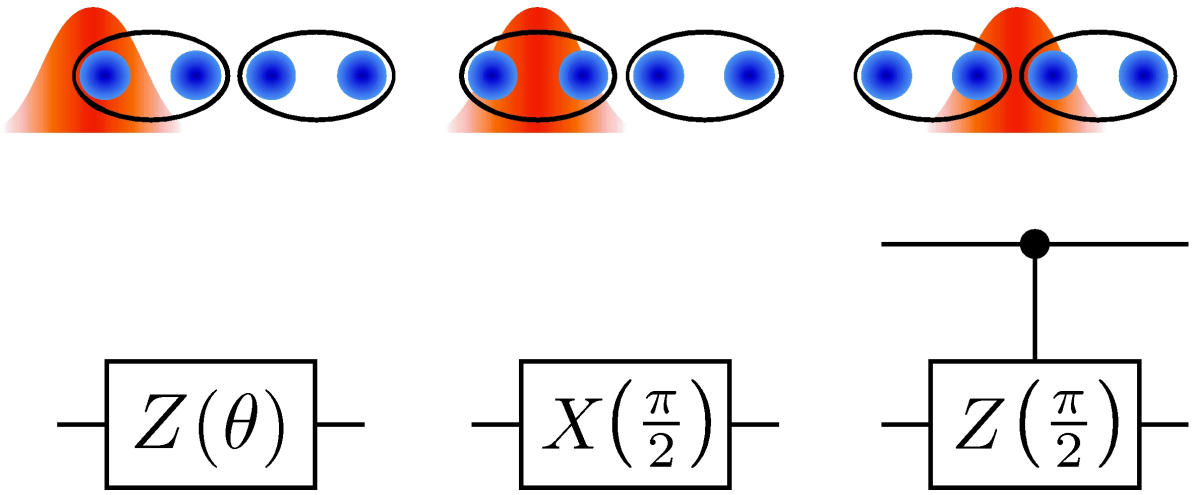

Figure 7.4: Implementation of quantum operations acting within a DFS: (left) Phase gate operations applied on single physical qubits directly affect the phase of the corresponding logical qubit. (centre) The MS interaction implemented as $X_P \otimes X_P$ on two physical qubits translates into a X_L in the subspace of a single logical qubit. (right) A geometric phase gate applied onto the centre-two of four qubits $\mathbb{1}_P \otimes Z_P \otimes Z_P \otimes \mathbb{1}_P$ is equivalent to a logical phase gate $Z_L \otimes Z_L$.

Coherent manipulation of quantum information encoded in a decoherence-free subspace is demonstrated by implementing a logical CNOT operation. The decomposition of the CNOT gate follows the same principle as the C&Z gate operation introduced in Sec. 5.2.1. A phase gate acting on the two logical qubits is enclosed by two Ramsey pulses acting on the target qubit. These two Ramsey pulses are represented by $X/Y(\pi/2)$ operations in the logical subspace and equivalent to MS$(\pi/2)$ operations acting on a pair of qubits (see Fig. 7.4 and Fig. 7.5).

As a first step the CNOT-gate performance is investigated by creating Bell states within the DFS. The control qubit is initialised in a superposition of $|0\rangle_L$ and $|1\rangle_L$ with the target qubit being either in $|0\rangle_L$ or $|1\rangle_L$. Depending on the relative phase of the control qubit and the chosen target qubit, any of the four Bell states within the DFS is generated [Data07f]. Here, two different aspects need to be considered: a) is the obtained state within the DFS? and b) how close is the generated quantum state to the desired one within the DFS? Question a) is answered in terms of the probability for finding the output state in the DFS. In the following this probability will be referred to as permanence P and is not necessarily related to the actual performance of the operation within the DFS. Question b) can be answered by quantum state reconstruction. Fig. 7.6 illustrates the density matrices of the four Bell states with state reconstruction yielding a mean fidelity of the quantum states of 91(2)% at a permanence of 89(4)%. The encouraging results of this initial investigation have been extended to the complete process tomography of

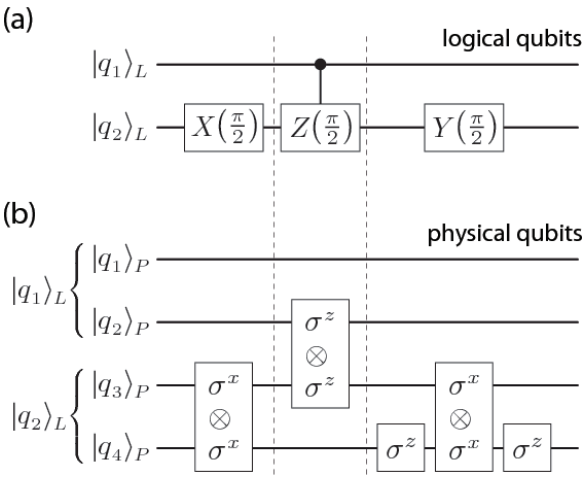

Figure 7.5: Pulse sequence to implement a CNOT operation within a decoherence-free subspace: The logical pulse sequence (a) illustrates a phase gate enclosed by Ramsey pulses of appropriate phases. In the physical space of 4 ions, this sequence translates into (b) MS gate interactions, a geometric phase gate and the application of addressed AC-Stark operations.

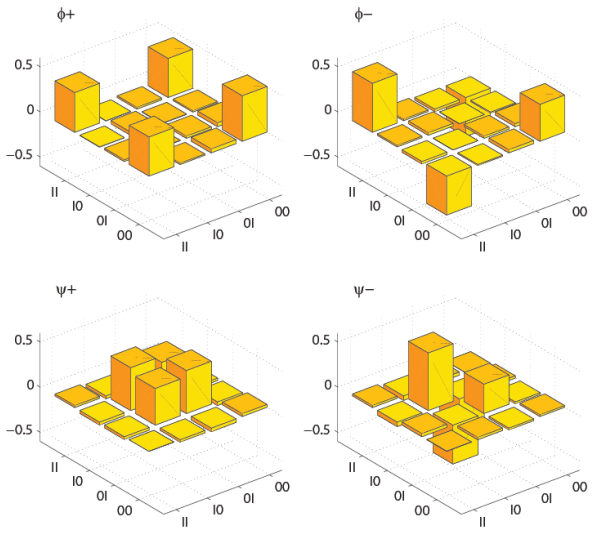

Figure 7.6: Bell states $\{\phi^+,\phi^-,\psi^+,\psi^-\}$ are generated within the logical subspace with fidelities of {89(1),91(1),91(1),92(1)}% at a permanence of {90.2,94.3,83.9,86.0}%. The figure presents the real part of the density matrix reconstructions from tomography data.

the logical CNOT operation [Data07f]. The mean permanence $\bar{P}$ is found to be 89(7)% and the mean process fidelity $\bar{F}$ is 89(4)%. The absolute values of the ideal as well as experimentally obtained χ matrices are shown in Fig. 7.7. The overall fidelity $\bar{P} \cdot \bar{F} \approx 79(7)\%$ is consistent with an expected value of about 83% based on the gate performance of the individual gates in the physical space.

Taking into account that the employed gate operations as well as the logical qubits are insensitive to magnetic field or laser frequency fluctuations, the obtained infidelities are estimated to stem mainly from laser-intensity-related imperfections. These can be separated into errors causing leakage from the DFS and errors within the DFS. Intensity fluctuations strongly affect the performance of the AC-Stark based phase-shift operations. However, this effect is limited to a single qubit and will result in errors that stay within the DFS. On the other hand, during MS gate interactions residual light illuminating neighbouring ions induces additional, undesired bit-flip operations. These operations map the quantum state out of the DFS. In case of the geometric phase gate, off-resonant excitations have a similar effect. All these issues, however, are of technical nature and can be improved with a better ion-addressing unit, an improved laser lock with a bandwidth notably higher than 1 MHz (which currently coincides with the trap-frequency) and more suitable trap parameters.

The above investigations show the advantages of encoding quantum information in a DFS - if available. The drawbacks are a notably reduced Hilbert-space because one qubit is encoded in two ions, and the challenging implementation of quantum gate operations acting within the DFS. At the current stage and in in view of the above experiments, it seems advisable to store quantum information in insensitive quantum states and investigate whether implementation of

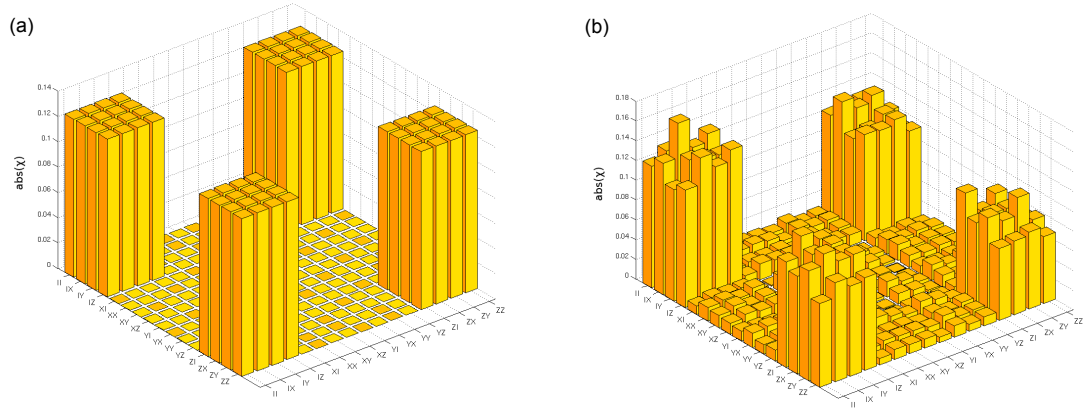

Figure 7.7: Illustration of the absolute values of the chi matrix for the CNOT operation within a decoherence-free subspace: (a) The ideal χ matrix (b) The experimentally derived χ matrix.

advanced algorithms can employ quantum states with a considerable overlap with decoherence-free subspaces. Regarding the size of currently available quantum registers of about 8, at most 14, qubits, encoding and computing quantum information completely within DFS seems to require too many resources to be advantageous for the encoding presented.

Chapter 8

Summary and outlook

The work presented in this thesis demonstrates part of the progress made on ion-trap based quantum quantum computation in Innbruck over the last five years.

The initial proposal for ion-trap-based quantum computation by Ciraz and Zoller [67] was successfully extended to incorporate higher phonon number. As a result, a scalable pulse sequence for the generation of GHZ states has been derived and experimentally realised, yielding GHZ states with a fidelity of about 88%. In addition, encoding of quantum information in higher vibrational numbers enabled the first realisation of a quantum Toffoli gate in an ion-trap based quantum computer [127]. Full process tomography was performed on several different implementations, yielding a mean gate fidelity of up to 70%.

The apparatus has been improved by adding a magnetic shield, refurbishing a large part of the electronic connections, and improving the magnetic-field generation as well as the mechanical stability of the setup, resulting in a coherence time of up to 100 ms which corresponds to at least a ten-fold improvement [59] compared to previous achievements in the same apparatus. For the first time in our setup, the coherence time approaches the lifetime of the excited state of our optical qubit of 1 s.

A global beam has been added to homogeneously illuminate the entire quantum string. The global beam has been applied to create W-states with a constant number of pulses regardless the number of qubits, yielding fidelities of about 89% for two and four qubits. Additionally the optical setup has been altered to allow for bichromatic light fields being applied onto the ion-qubits. With these bichromatic light fields, the MS gate interaction [98] as well as the geometric phase gate [103] have been implemented. In combination with the global addressing, the MS gate has been successfully applied to generate genuine 14-particle entanglement with a confidence of 76%. During these investigations we found the MS gate to perform at fidelities from about 99% for two ions to about 82% for 8 ions [59]. These promising results were the stepping stone in several high-fidelity experiments employing the MS gate as its core entangling operation [106, 128, 129].

In conclusion, previous algorithms in the presented setup which were limited to at most three qubits (the realisation of deterministic quantum teleportation [19]) have been successfully extended to four qubits by demonstrating an implementation of deterministic entanglement swapping [107] as well as performing logical operations on qubits encoded in a decoherence-free subspace [126].

The improvements to the apparatus which have been presented – specifically a coherence

time of up to 100 ms and entangling-gate operations of above 80% fidelity when acting on 8 qubits and notably better on fewer qubits – represent the basis for world-leading experiments to come. Nevertheless, there remains a list of experimental problems that still need to be tackled. Additional necessary improvements, such as better intensity stabilisation, greater temperature stability of the trap, improved beam-pointing stability, lower magnetic field noise and several more, have been mentioned along the lines of the work presented and are discussed in detail in Appendix C.

On a broader scope, scalability of quantum computers to significantly more qubits will be required in future experimental setups. Here, several aspects need to be considered: Besides storing larger quantum registers, the ratio of coherence time to time for quantum operations – effectively the number of quantum operations that can be implemented – needs to be increased. The presented linear trap can only store about 14 ions as a linear string. In contrast to our four-blade linear trap, traps with segmented electrodes can handle 100 and more ions efficiently [130]. With such large quantum registers, additional challenges need to be addressed. The worst-case sensitivity of optical qubits to phase noise scales quadratically with the size of the register (see Appendix A). Using decoherence-free subspaces as presented in Sec. 7.2, this problem can be suppressed up to the point when life-time limitations of the qubits are reached. Encoding qubits in quantum states that do not represent any realistic life-time limitations (for example encoding the qubit in the Zeeman manifold of $4^2\mathrm{S}_{1/2}$) may allow for temporal longer computations. Alternatively, significantly faster quantum operations such as proposed and partially already realised in Ref. 115–117 allow for more quantum operations within the coherence time of the quantum register.

A conceptionally more challenging aspect will be the characterisation of the experiments that can now be realised in our apparatus. Full state tomography has been performed with up to eight qubits. A full tomography on the 14 qubit quantum state, or even more challenging, a process tomography of the employed entangling gate, is not feasible with current techniques. There are some promising approaches that require fewer resources for a characterisation, but these alternative methods are novel and not fully investigated yet. Hopefully the experiments performed during the presented work will trigger additional theoretical investigations with regards to characterising quantum information and coherent control in a real-life experiment beyond 10 qubits.

Appendix A

Collective phase noise affecting quantum registers

The following theoretical derivation is based on discussions with William Coish, a co-author in a joint publication [59].

Decoherence effects represent one of the main limitations in the presented ion-trap quantum computer. However, symmetries in the noise, here in particular collective phase noise, may also present means of overcoming that decoherence mechanism, as represented in Sec. 7.2. Considering collective phase noise is dominant in the presented apparatus, the following represents an in-detail derivation of how the said decoherence affects GHZ states. While this may seem to be a very specific topic, it is important to note that collective phase noise is present in almost every system employing energetically non-degenerate qubits - fluctuations in the required phase-reference would collectively affect the quantum register. In addition, the conclusions derived from this investigation affect any quantum state ρ with $\mathrm{tr}(\rho|1\ldots1\rangle\langle0\ldots0|) \neq 0$.

We model collective phase noise by magnetic-field fluctuations affecting the complete quantum register by

$$H(t) = \frac{1}{2}\mu\Delta B(t)S_z \tag{A.1}$$

with μ describing the magnetic-field sensitivity, $\Delta B(t)$ being the fluctuations of the magnetic field as a function of time t and $S_z = \sum_{k=1}^{N} \sigma_z^{(k)}$ representing a collective phase fluctuation of each qubit k in a quantum register consisting of N qubits[1]. The initial quantum state affected by this noise is

$$|\psi(t=0)\rangle = \frac{1}{\sqrt{2}}(|0\ldots0\rangle + |1\ldots1\rangle) \tag{A.2}$$

As a measure for the state preservation we use the fidelity of the quantum state $\rho(t) = |\psi(t)\rangle\langle\psi(t)|$ after a time t compared to its initial state $|\psi(0)\rangle$

$$F(t) = \langle \mathrm{Tr}(|\psi(0)\rangle\langle\psi(0)|\rho(t))\rangle \tag{A.3}$$

where $\langle\ldots\rangle$ indicates an ensemble average over random fluctuatinos $\Delta B(t)$ and

[1] Frequency fluctations in the reference laser can be described the very same way, with $\mu\Delta B$ being directly replaced by the frequency detuning $\hbar\Delta\nu$

$|\psi(t)\rangle \;=\; U(t)\,|\psi(0)\rangle$ with

$$|\psi(t)\rangle = \frac{1}{\sqrt{2}}\langle\left[\exp\left(-i\frac{N}{2\hbar}\mu\int_0^t \mathrm{d}t'\Delta B(t')\right)|0\ldots0\rangle + \exp\left(i\frac{N}{2\hbar}\mu\int_0^t \mathrm{d}t'\Delta B(t')\right)|1\ldots1\rangle\right]\rangle \tag{A.4}$$

It follows that $\mathrm{Tr}(|\psi(0)\rangle\langle\psi(0)|\rho(t)) = |\langle\psi(0)|\psi(t)\rangle|^2$ with

$$|\langle\psi(0)|\psi(t)\rangle|^2 \;=\; \frac{1}{2}\langle\left[1+\cos\left(N\frac{\mu}{\hbar}\int_0^t \mathrm{d}t'\Delta B(t')\right)\right]\rangle \tag{A.5}$$

which can be rewritten as

$$F(t) = \frac{1}{2}(1+\mathrm{Re}(\langle\exp\left(-i\frac{\mu}{\hbar}N\int_0^t \mathrm{d}t'\Delta B(t')\right)\rangle)) \tag{A.6}$$

We assume that $\Delta B(t)$ is a Gaussian process. From the Gaussian moment theorem [131] it follows that

$$\langle\exp(-i\Phi)\rangle = \exp(-\frac{1}{2}\langle\Phi^2\rangle) \tag{A.7}$$

with $\Phi = N\frac{\mu}{\hbar}\int_0^t \mathrm{d}t'\Delta B(t')$. This allows us to rewrite the state preservation in terms of a fidelity as

$$F(t) = \frac{1}{2}(1+\exp(-\frac{1}{2}(\frac{\mu}{\hbar}N)^2 C(t)) \tag{A.8}$$

with

$$C(t) = \int_0^t \mathrm{d}t_1\int_0^t \mathrm{d}t_2\langle\Delta B(t_1)\Delta B(t_2)\rangle. \tag{A.9}$$

Up to this point we have only assumed the process to be Gaussian. In order to derive an analytical form for the fidelity decay we need to make further assumptions. First we assume that the noise process can be regarded as stationary, i.e.:

$$\langle\Delta B(t+\tau)\Delta B(t)\rangle = \langle\Delta B(\tau)\Delta B(0)\rangle\;\forall t \tag{A.10}$$

We then rewrite Eq. (A.9) using Eq. (A.10) as

$$C(t) = \int_0^t \mathrm{d}t_1\int_0^t \mathrm{d}t_2\langle\Delta B(t_1-t_2)\Delta B(0)\rangle \tag{A.11}$$

Changing the variables according to $\tau = t_1 - t_2, t' = \frac{1}{2}(t_1+t_2)$,

$$\text{for } t_2 = 0 \;:\; \tau = t_1 = 2t' \tag{A.12}$$

$$\text{for } t_1 = t \;:\; \tau = t - t_2 = 2t' = t - (2t'-t) = 2(t-t') \tag{A.13}$$

Eq. (A.11) can be regarded as a two-dimensional integral that transforms with the new variables into

$$C(t) \;=\; 2\int_0^t \mathrm{d}t_1\int_0^{t_1} \mathrm{d}t_2\langle\Delta B(t_1-t_2)\Delta B(0)\rangle \tag{A.14}$$

$$\;=\; 2\int_0^t \mathrm{d}\tau\int_{\tau/2}^{t-\tau/2} \mathrm{d}t'\langle\Delta B(\tau)\Delta B(0)\rangle \tag{A.15}$$

It follows that the initial function $C(t)$, for stationary and Gaussian noise, simplifies to

$$C(t) = 2\int_0^t \mathrm{d}\tau(t-\tau)\langle\Delta B(\tau)\Delta B(0)\rangle \tag{A.16}$$

As an additional assumption, we insert a generic form for the correlation function $\langle\Delta B(\tau)\Delta B(0)\rangle$ of the noise. We choose the noise to be characterised by an exponentially decaying correlation with a decay time $\tau_c = \frac{1}{\gamma}$:

$$\langle\Delta B(\tau)\Delta B(0)\rangle = \langle\Delta B^2\rangle \exp(-\gamma t) \tag{A.17}$$

The integral is straightforward to calculate and yields

$$C(t) = 2\frac{\langle\Delta B^2\rangle}{\gamma^2}\{\exp(-\gamma t) + \gamma t - 1\} \tag{A.18}$$

Combining Eq. (A.8) and Eq. (A.18), we derive a formula describing the loss of fidelity of GHZ states affected by collective Gaussian, stationary phase noise:

$$F(t) = \frac{1}{2}(1 + \exp(-\frac{(\frac{\mu}{\hbar}N)^2\langle\Delta B^2\rangle}{\gamma^2}\{\exp(-\gamma t) + \gamma t - 1\}) \tag{A.19}$$

This equation describes the static, the Markovian and the intermediate regime:

- For $\gamma t \ll 1$, $\{\exp(-\gamma t) + \gamma t - 1\} \approx \frac{1}{2}\gamma^2 t^2$ from which follows the static result:

$$F(t) \cong \frac{1}{2}(1 + \exp(-\frac{1}{2}(\frac{t}{\tau})^2)),\ \frac{1}{\tau} = N\frac{\mu}{\hbar}\sqrt{\langle\Delta B^2\rangle} \tag{A.20}$$

- For $\gamma t \gg 1$, we recover the Markovian limit:

$$F(t) \cong \frac{1}{2}(1 + \exp(-\frac{t}{T_2}),\ \frac{1}{T_2} = N^2\frac{\langle(\frac{\mu}{\hbar}\Delta B)^2\rangle}{\gamma} \tag{A.21}$$

Up to this point the description is based on the assumptions that the noise is Gaussian, stationary and follows a specific correlation function. In particular, modelling the correlation function as an exponential decay might be questioned. We test the correlation function of the magnetic field noise by independently measuring the magnetic field fluctuations next to the vacuum chamber using a probe[2], calculating the expected fidelity decay and compare this prediction with the experiment.

Figure A.1 shows the power spectrum of the magnetic field fluctuations [Data10e]. Strong frequency components are observed at 50 Hz and 150 Hz which are contributed by the powerline. The broad peaks at 1.5 kHz attributed to the servo-bump of the current-stabilisation. These 1.5 kHz components directly correspond to the oscillations seen in the correlation function (see Fig. A.2), with an envelope following an exponential decay with a time constant of 1.983(3) ms. Thus we have verified that the assumption of an exponentially decaying correlation function agrees well with the apparatus presented[3]. The central limit theorem suggests that many noise processes combined will be Gaussian.

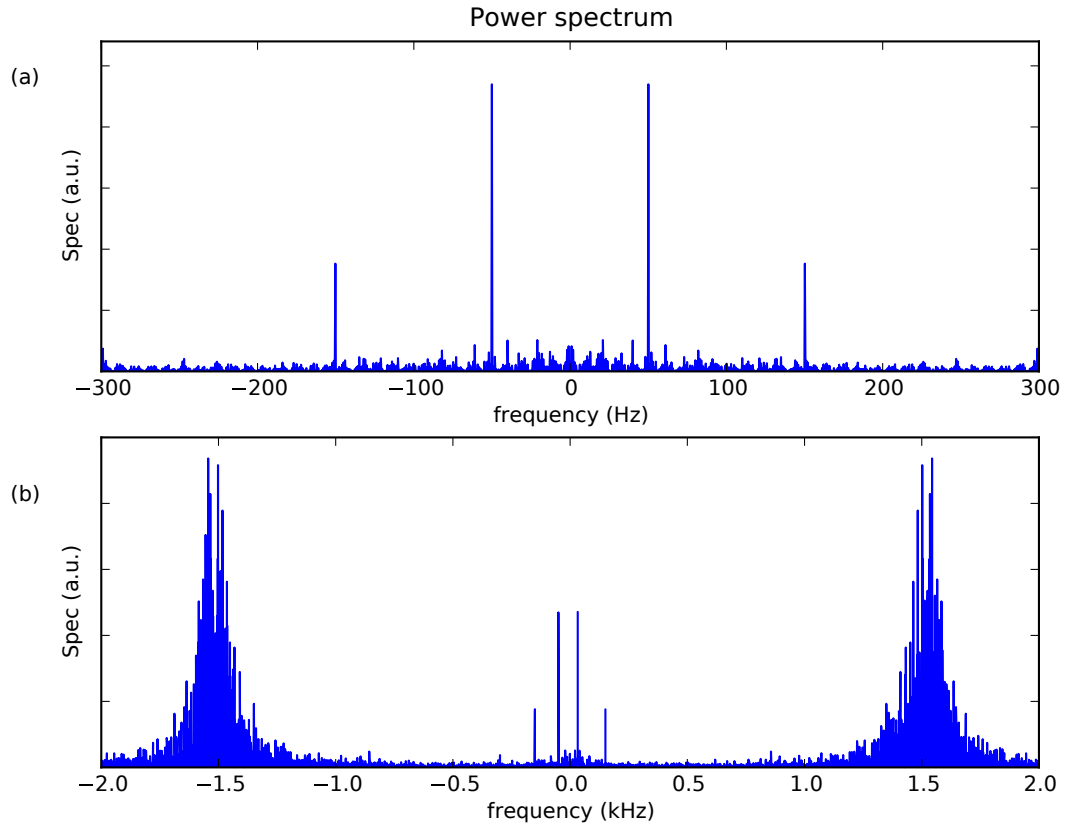

Figure A.1: The power spectrum of the magnetic field fluctuations shows dominant components at 50 Hz and 150 Hz (a) as well as servo-bumps of the current-stabilisation electronics at about 1.5 kHz (b).

Based on the correlation function calculated from magnetic field fluctuations a fidelity decay can be predicted via Eq.(A.8), only assuming the noise to be Gaussian. The predicted fidelity decay is shown as solid line in Fig. A.3 with additional features not covered in the model which returned Eq. A.19: The broad frequency components at 1.5 kHz can be interpreted as short coherence time in the noise and results in a swiftly vanishing oscillation of the fidelity decay within the first 5 ms as shown in the inset in Fig. A.3. The strong component at 50 Hz leads to a decay behaviour that flattens out every 20 ms. The prediction for the coherence decay shows good agreement with Ramsey experiments [Data10e] depicting the coherence of a single qubit as a function of time.

The above investigation supports our Gaussian noise model with an exponentially decaying correlation time. However, our model was only investigated with a single qubit. In chapter 7.2 we verified that collective phase noise is dominant in the presented apparatus. In the following we will present an additional investigation on to whether GHZ state are affected as described by our model.

[2]Spicer Consulting; Field Cancelling System, Type SC12; AC probe (SN: 02090)

[3]In detail, the envelope of the correlation function follows an exponential decay. The superimposed oscillation that was found in the experiment does not change the overall predictions of our model.

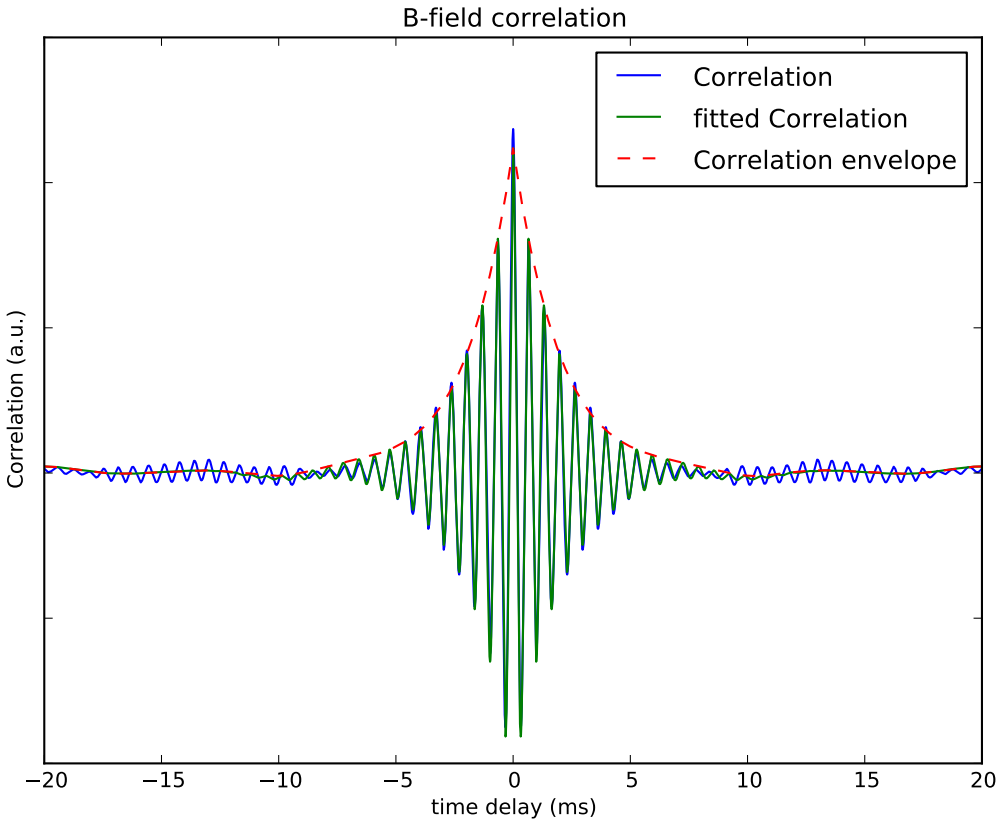

Figure A.2: Correlation function of the measured magnetic-field fluctutations: The envelope clearly follows an expomential decay with a time-constant of 1.983(3) ms. The enclosed oscillation has a frequency of 1.5 kHz in agreement with the servo bump of the current stabilisation circuit. Other frequency components and their beat frequencies follow accordingly, yet are negligibly small (visible at correlation times larger than 10 ms).

For collective phase noise affecting the complete quantum register, the result of our derivation in Eq. (A.19) suggests that GHZ states should be N^2 more sensitive to correlated phase noise compared to a single qubit. Following a measurement procedure as described in Sec. 6.3.2, the coherence of GHZ states is investigated and compared with a single qubit. Including a waiting time between the generation of the GHZ state and the investigation of parity measurements, the coherence of the quantum state can be derived as a function of time. Figure A.4 a) illustrates measurements performed on 2 [Data09a], 3 [Data09b], 4 [Data09c], 6 [Data09d] and 8-qubit [Data09e] GHZ states in comparison with a single qubit. The relative sensitivity between the GHZ state and a single qubit as a function of the number of qubits taking part in the GHZ state is found to scale with $N^{2.0(1)}$ (see Fig. A.4 b)). This is in full agreement with the predictions of the presented model on the coherence decay of GHZ states in the presence of correlated phase noise.

This "superdecoherence" [132] has implications beyond the field of quantum information processing. For instance GHZ states have been investigated in the field of quantum metrology - a discipline trying to improve the precision of measurements with the help of quantum effects.

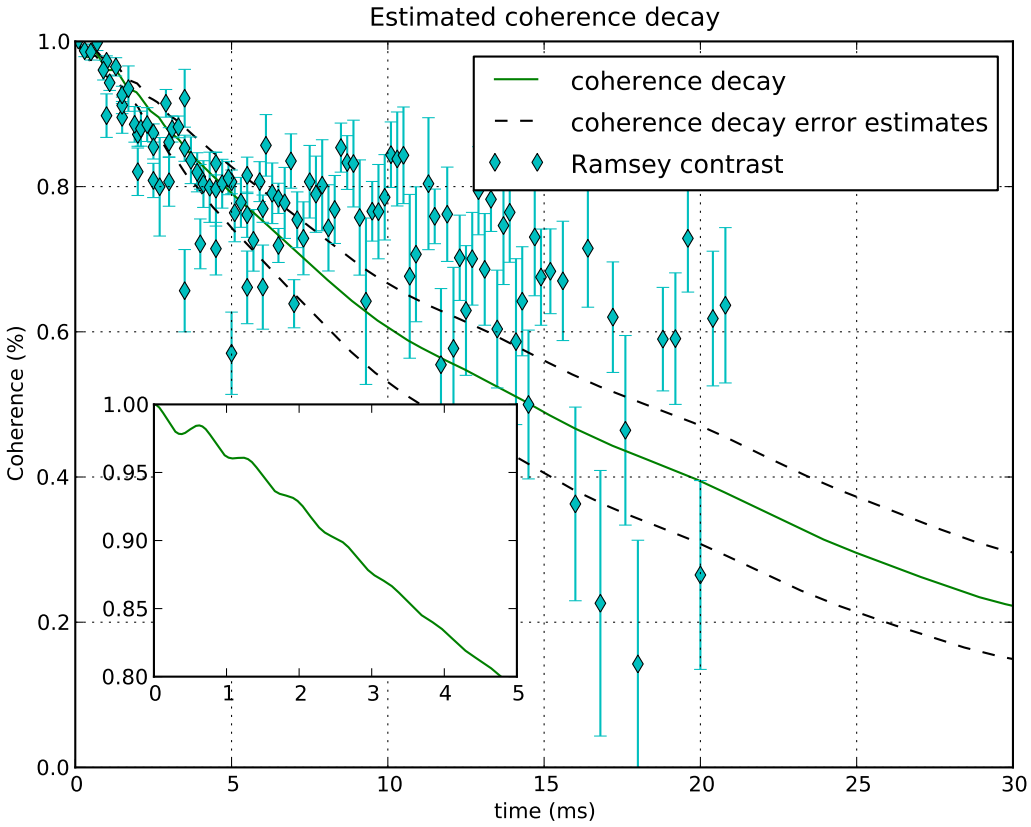

Figure A.3: The estimated coherence decay of a single qubit is calculated based on Eq. (A.8) and the measured magnetic-field fluctuations. Here, the magnetic-field sensor could not be placed at the location of the ion so estimations on the actual magnetic field and its flucations in the centre of the trap were required. The uncertainty in the noise is indicated by dashed lines. The theoretical prediction roughly overlaps with experimentally obtained results. At around 10 ms the observed coherence levels out, in agreement with dominant 50 Hz noise in the investigated apparatus. Higher frequency components of the coherence decay, such as the servo-bump of the current stabilisation electronics, can not be observed within the limitations set by projection noise. Here, the inset shows the predicted, swiftly decaying oscillations assigned to the servo-bump with an amplitude of below 1%.

GHZ states are often used as an example for enhanced phase sensitivity. In Sec. 6.3.2 (see Fig. 6.6) the parity of N-qubit GHZ states was shown to be a factor of N more sensitive to the phase of the investigating light-field. This is often proposed as a tool to determine frequencies or relative detunings, with higher resolution. At a first glance, this approach is promising but does not take into account the higher sensitivity of these states with respect to noise. Even for dominant uncorrelated phase noise it has been shown that frequency measurements employing GHZ-states will not improve the precision compared to unentangled qubits [133]. In the following we will show that in the presence of dominant collective phase noise two unentangled qubits already outperform any GHZ state.

Consider N qubits subject to Ramsey experiments to determine a frequency detuning within 1 s. The noise is assumed to be in the Markovian regime. The resolution of the Ramsey

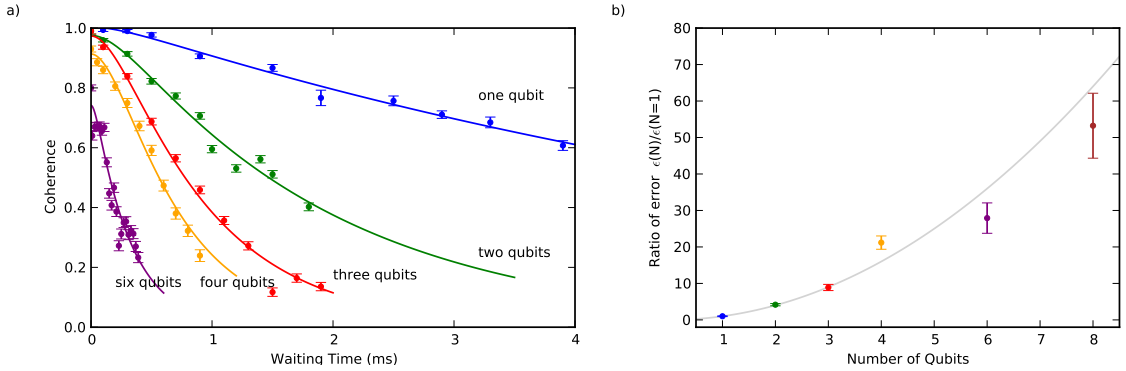

Figure A.4: Comparison of the single qubit coherence to an N-qubit GHZ state. (a) GHZ state coherences decay significantly faster than a single qubit coherence. (b) We find a ratio in the decay equal to $N^{2.0(1)}$, in agreement with the predictions for correlated phase noise.

experiment scales linearly with the Ramsey time t_R. However, the remaining contrast of the Ramsey signal decreases exponentially by $\exp(-t_R/t_C)$ with t_C representing the coherence time of a single qubit. Averaging over N qubits yields an additional gain in the precision proportional to $\sqrt{N}$. These experiments can be performed $1/t_R$ times within 1 s and increase the precision by $1/\sqrt{t_R}$ via averaging. In total, the precision P_{unent} of the experiment employing unentangled qubits, as a function of the Ramsey time t_R, is

$$P_{\text{unent}}(t_R) = t_C \exp(-t_R/t_C)\sqrt{\frac{N}{t_R}} \tag{A.22}$$

Too-short Ramsey times do not reach a suitable precision of the experiment, while too-long Ramsey times face a loss of contrast. The ideal Ramsey time $t_R^{\text{unent,ideal}}$ maximising P_{unent} is

$$t_R^{\text{unent,ideal}} = \frac{t_C}{2} \tag{A.23}$$

and leads to a precision

$$P_{\text{unent}}(t_R^{\text{unent,ideal}}) = \sqrt{\frac{N t_C}{2e}} \tag{A.24}$$

The same derivation (similar to Eq. (A.22)) can be performed with N-qubit GHZ states. Here, the contrast decreases by $\exp(-N^2 t_R/t_C)$ while the N-qubit GHZ state directly provides a measurement gain proportional to N (in contrast to a gain of $\sqrt{N}$ from averaging unentangled qubits) These $1/t_R$ measurements within 1 s average to an additional gain of $1/\sqrt{t_R}$. The ideally chosen Ramsey time $t_R^{\text{ent,ideal}}$ for frequency measurement based on GHZ states is

$$t_R^{\text{ent,ideal}} = \frac{t_C}{2N^2} \tag{A.25}$$

accompanied by a maximum precision of

$$P_{\text{ent}}(t_R^{\text{ent,ideal}}) = \sqrt{\frac{t_C}{2e}}. \tag{A.26}$$

Interestingly, the maximum precision achievable by a Ramsey experiment employing GHZ states in the presence of dominant collective phase noise is constant. In particular it is equal to the precision achievable by a single qubit. In this sense, two unentangled qubits already outperform any multi-qubit GHZ state - if the environment induced dominant collective phase noise.

This is not to say that GHZ states will not perform better than uncorrelated qubits under any conditions. The above derivation is based on a frequency measurement where ideal Ramsey times may be chosen based on the noise parameters of the experiment with a correlation time of the noise significantly smaller than the Ramsey time. Should there be additional constraints, such as a maximum Ramsey interrogation time that may employed, GHZ states may outperform uncorrelated qubits. Here GHZ states are able to indicate frequency detunings faster than uncorrelated qubits which may be benefiting under certain conditions.

Even if collective phase noise may not be apparent in the experiment, for a large enough quantum register any collective phase noise[4] will overtake any linearly scaling noise in the experiment. This effect may limit upcoming quantum metrology investigations based on GHZ states. Possible solutions to this problem may be based on alternative quantum states that yield higher precision measurements compared to unentangled qubits yet are not as susceptible to correlated phase noise as GHZ states. Ideas along these lines are mentioned, together with a more detailed theoretical derivation of the metrology experiments mentioned above, in a publication by Uwe Dorner [134] that was prepared at the same time as this manuscript.

[4]For instance a laser or radio frequency often represents the phase reference for a energetically non-degenerate quantum register. Any noise on the phase reference is correlated with respect to the entire quantum register. Considering that all qubits need to be phase-stable with respect to each other, it is not possible to consider individual, local phase references for each qubit.

Appendix B

Quantum state detection and spontaneous decay

Quantum state detection is currently performed by electron shelving [17], with the scattered photons being detected by a photo-multiplier tube (PMT) and/or a CCD camera. While this technique is easy to apply, it may be subject to an often neglected error: spontaneous decay of the excited state during the detection period. Considering a detection time of about 3 ms for the PMT and about 8 ms for the CCD camera, the probability for spontaneous decay happening in this detection window is approximately 0.3% for the PMT or 0.8% for the CCD camera per $^{40}Ca^{+}$ ion. From this follows that there is a trade-off between scattering a sufficient number of photons and risking spontaneous decay during the detection window. The following calculations provide an estimate of these errors which help one to select an optimal detection time.

The work follows extensive discussions with Koenraad Audenaert who provided detailed investigations of an ion string being subject to a measurement based on electron shelving with the scattered photons detected by a PMT. The majority of this work has been performed by Koenraad Audenaert. His notes are included directly here to emphasise his role in this investigation. They show that our current detection time of 3 ms with the PMT is an ideal trade-off between detection-fidelity and errors from spontaneous decay.

Error sources in PMT detection of a number of bright ions

Koenraad Audenaert, priv. comm.

In this note I derive an approximate formula for conditional outcome probabilities of a PMT detector used for determining the number of bright (S-state) ions in a string of N ions, conditional on B ions being bright and $D = N - B$ ions being dark. Let A be the count rate produced by a single bright ion (in numerical examples below, I assume $A = 55000$). This detector integrates the accumulated photons scattered by the ions over a time interval T and bins them in bin intervals $[(j-1/2)\mu, (j+1/2)\mu]$, where $\mu = TA$ is the average number of counts produced by a single bright ion during the time interval T.

The main sources of error that are considered here are spill-over to incorrect bins, due to the inherent Poissonian character of the scattered light, and decay of a dark state (D-state) to a bright state (S-state). We assume the bright state has a life-time of τ=1s. Throughout this note, k will stand for the number of photons detected by the PMT during T.

Let's consider a single ion first. If it is in the bright state, it will scatter light during the entire time interval T, and give rise to a number of counts k that is Poisson distributed with mean $\mu = TA$:

$$P_k^{(1\text{ bright})} = e^{-\mu}\mu^k/k! \tag{B.1}$$

If, however, it is in the dark state, it will remain so during time interval T with probability

$$\int_T^\infty dt e^{-t/\tau}/\tau = e^{-T/\tau}.$$

This gives a contribution $e^{-T/\tau}$ to $P_k^{(1\text{ dark})}$ at $k = 0$. With probability $dt\, e^{-t/\tau}/\tau$ the ion will decay during the infinitesimal time interval $[t, t+dt]$, at which point it will become bright and scatter photons for the remaining $T - t$ amount of time. This gives a contribution to $P_k^{(1\text{ dark})}$ equal to

$$dt\,\frac{1}{\tau}e^{-t/\tau}e^{-(T-t)A}((T-t)A)^k/k!$$

Integrating over $0 \le t \le T$ and adding the $k = 0$ contribution yields

$$\begin{aligned} P_k^{(1\text{ dark})} &= \delta_{k,0}e^{-T/\tau} + \int_0^T dt\,\frac{1}{\tau}e^{-t/\tau}e^{-(T-t)A}((T-t)A)^k/k! \\ &= \delta_{k,0}e^{-T/\tau} + \frac{e^{-T/\tau}}{\tau}\frac{A^k}{(A-1/\tau)^{k+1}}P(k+1,(A-1/\tau)T). \end{aligned}$$

Here, P is the regularised incomplete gamma function defined as

$$P(k+1,z) = \int_0^z \frac{t^k}{k!}e^{-t}dt, \tag{B.2}$$

i.e. it is the cumulative distribution function, meaning the sum of all probabilities from 0 to z as indicated by the integral in Eq. (B.2), of the gamma distribution with parameter k. We made the assumption $A > 1/\tau$, because otherwise the integral does not reduce to P. In practice, this condition is always fulfilled. Moreover, $1/\tau$ can always be ignored w.r.t. A. Thus we get

$$P_k^{(1\text{ dark})} \approx \delta_{k,0}e^{-T/\tau} + \frac{e^{-T/\tau}}{A\tau}P(k+1,\mu).$$

The value of $P(k+1,\mu)$ is approximately 1 for k much less than μ and approximately 0 for k much larger than μ. It decreases gradually over the interval $[\mu-2\sqrt{\mu},\mu+2\sqrt{\mu}]$ (which is the interval where the Poisson distribution with mean μ is essentially non-zero). To simplify the calculations in the remainder of this note, I will approximate P by a step function positioned at $k=\mu$. Rescaling the coefficient so that $\sum_{k=0}^{\infty} P_k = 1$ then gives

$$P_k^{(1\text{ dark})} \approx \delta_{k,0}e^{-T/\tau} + \frac{1-e^{-T/\tau}}{\mu}(1-\Phi(k-\mu)). \tag{B.3}$$

This formula has a simple intuitive explanation: with probability $e^{-T/\tau}$, the dark state remains dark throughout the interval $[0,T]$ and does not scatter any photons; with probability $1-e^{-T/\tau}$ the dark state decays at a time instant distributed roughly rectangular over the interval $[0,T]$, yielding photon counts that are distributed roughly rectangular as well, over each interval $\{0,1,\ldots,\mu-1\}$.

We now consider the photon count probabilities for B bright ions. Since the sum of Poissonian variables is again Poissonian with the mean of the overall distribution equal to the sum o the means of individual distributions, we simply get

$$P_k^{(B\text{ bright})} = e^{-B\mu}(B\mu)^k/k! \tag{B.4}$$

The calculations for D dark ions are more involved. The $D=1$ probability distribution consists of two contributions: a $\delta_{k,0}$ part, with probability $1-\alpha = e^{-T/\tau}$, and a discrete rectangular part (over $\{0,1,\ldots,\mu-1\}$) with probability α (usually small). Thus we get

$$P_k^{(D\text{ dark})} = \sum_{j=0}^{D}\binom{D}{j}(1-\alpha)^{D-j}\alpha^j p_k(j,\mu),$$

where $p_k(j,\mu)$ is the probability distribution of a sum of j discrete random variables, distributed according to a discrete rectangular distribution over $\{0,1,\ldots,\mu-1\}$. In addition, we define $p_k(0,\mu)=\delta_{k,0}$. For $j=1$ we have the original discrete rectangular distribution over $\{0,1,\ldots,\mu-1\}$, for $j=2$ we get a discrete triangular distribution over $\{0,1,\ldots,2\mu-2\}$, while for larger j we get a distribution that tends to a discretised Gaussian distribution. In all cases the mean is $j(\mu-1)/2$ and the variance is $j(\mu^2-1)/12$. For small enough α, however, only the $j=0$ and $j=1$ terms contribute appreciably, and we can use the approximation

$$P_k^{(D\text{ dark})} \approx (1-\alpha)^D\delta_{k,0} + (1-(1-\alpha)^D)p_k(1,\mu). \tag{B.5}$$

To check the validity of this approximation, we compare the coefficients of the $j=1$ term; the original value is $D\alpha(1-\alpha)^{D-1}$, while the value in the approximation is $1-(1-\alpha)^D$. Expanding as a Taylor series to second degree in α gives $D\alpha - D(D-1)\alpha^2$ for the former and $D\alpha - D(D-1)\alpha^2/2$ for the latter. The approximation is therefore well justified when $D(D-1)\alpha^2/2$ is small compared to $D\alpha$, i.e. when $(D-1)\alpha/2$ is much smaller than 1.

Numerical example: $T=0.004$ and $\tau=1$ give $\alpha\approx T/\tau = 0.004$, hence for $D=16$, $(D-1)\alpha/2 = 0.03$. Dropping the $j>1$ terms therefore has the effect of a 3% increase of the $j=1$ term, which itself is already small, with a magnitude of the order of 0.06.

Now we can combine the two formulas (for dark and bright ions) and get the distribution of K, the random variable representing the total photon count, conditional on B ions being bright and D ions (initially) dark, with $N = B + D$:

$$\begin{aligned} P_K(k|B,D) &= \sum_{j=0}^{k} P_j^{(D)} P_{k-j}^{(B)} \\ &= \sum_{j=0}^{k} \left((1-\alpha)^D \delta_{j,0} + (1-(1-\alpha)^D) p_j(1,\mu)\right) \; e^{-B\mu}(B\mu)^{(k-j)}/(k-j)! \\ &= (1-\alpha)^D e^{-B\mu}(B\mu)^k/k! + (1-(1-\alpha)^D) \sum_{j=0}^{\min(k,\mu)} e^{-B\mu}(B\mu)^{(k-j)}/(k-j)! \end{aligned}$$

The summation over j simplifies to

$$w_\mu(k,B) := Q(k+1, B\mu) - Q(k-l, B\mu),$$

where $l = \min(k,\mu)$ and $Q = 1-P$. For $k > \mu$, this simplifies to $Q(k+1,B\mu) - Q(k-\mu,B\mu)$. For $0 \le k \le \mu$, we have $Q(k+1,B\mu) - Q(0,B\mu)$ instead.

The function $w_\mu(k,0)$, with $B = 0$, is equal to $1 - \Phi(k-\mu)$. For $B > 0$, $w_\mu(k,B)$ is roughly equal to 1 when $B\mu \le k \le (B+1)\mu$, and approximately 0 otherwise. At the boundary of this interval, w_μ changes smoothly from one value to the other, and the larger the value of B the more slowly this happens (see figure B.1).

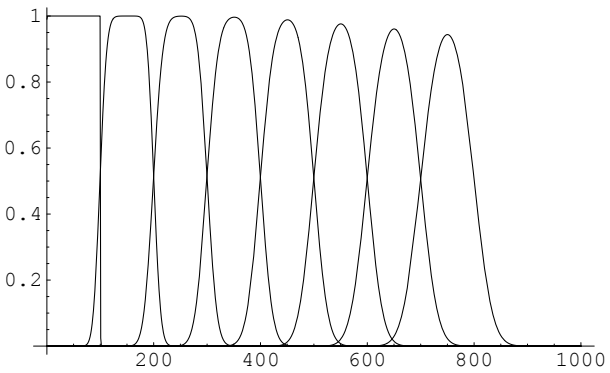

Figure B.1: Graph of the function $w_\mu(k,B)$ for $\mu = 100$ and $B = 0, 1, \ldots, 7$.

In summary, we have, to a good approximation,

$$P_K(k|B,D) = (1-\alpha)^D e^{-B\mu}(B\mu)^k/k! + (1-(1-\alpha)^D) w_\mu(k,B). \tag{B.6}$$

The final stage of the PMT detector is the binning stage. As mentioned, the photon counts are collected in bin intervals $[(n-1/2)\mu, (n+1/2)\mu)$, $n = 1, 2, \ldots$ where $\mu = TA$. That is to say, if the photon count k lies in the n-th bin interval, the detector will produce outcome n. The first ($n = 0$) bin of course only ranges over $[0, \mu/2)$. We now calculate the probability

$P_N(n|B,D)$ that outcome n is produced, conditional on B specified ions being bright and the others (initially) dark. This is simply done by summing $P_K(k|B,D)$ over the various bin intervals. Thus:

$$\begin{aligned} P_N(0|B,D) &= \sum_{k=0}^{\mu/2-1} P_K(k|B,D) \\ P_N(n|B,D) &= \sum_{k=(n-1/2)\mu}^{(n+1/2)\mu-1} P_K(k|B,D). \end{aligned}$$

We first calculate the contribution due to the first term in $P_K(k|B,D)$, which is solely due to the Poissonian character of the counts. This can be stated again in terms of the incomplete gamma function, using

$$\sum_{k=k_0}^{k_1} e^{-B\mu}(B\mu)^k/k! = Q(k_1+1, B\mu) - Q(k_0+1, B\mu).$$

Thus the contribution of the first term is

$$\begin{aligned} P_N(0|B,D)' &= Q(\mu/2, B\mu) - Q(1, B\mu) \\ P_N(n|B,D)' &= Q((n+1/2)\mu, B\mu) - Q((n-1/2)\mu+1, B\mu). \end{aligned}$$

This is illustrated, for $\mu = 100$, in Tab. B.1.

One sees that there is spill-over from the main bin (corresponding to $n = B$) to both neighbouring bins, and the amount of spill-over increases with B. This is intuitively clear. The variance of a Poisson distribution is equal to the mean, hence with B bright ions, the variance is $B\mu$. To limit the amount of spill-over to, say 5%, the main $n = B$ bin should be wide enough to contain the probability mass contained in the interval $B\mu \pm 2\sqrt{B\mu}$. To reduce it further to, say, 0.003, it should be made as wide as $B\mu \pm 3\sqrt{B\mu}$. Of course, the width of the bins is fixed by μ, namely to $\pm\mu/2$. Therefore, noting that the largest possible value of B is N, we get our first result:

> To get the Poissonian spill-over term below 0.05 (0.003), the value of μ should be at least $16N$ ($36N$).

For example, with $N = 16$ and the reported value of $A = 55000$, the measurement time T should be 4.6 ms (10.5 ms). An explicit formula for the worst-case Poissonian spill-over probability is

$$1 - (Q((N+1/2)\mu, N\mu) - Q((N-1/2)\mu+1, N\mu)), \tag{B.7}$$

which decays roughly exponentially. For $N = 16$, this probability is approximately $e^{-\frac{\mu}{107}}/1.94$.

Next, we treat the second term, due to decay of the dark state. Consider figure B.1, for the case $\mu = 100$. Hence, the bins are centered at multiples of 100 and have width ± 50. The $w_\mu(k,B)$ curves are (to a good approximation) symmetric around the value $k = (B+1/2)\mu$, and for not too great a value of B, their width is $\pm\mu/2$. Thus, to a first approximation, each curve contributes half of the counts to the bin $n = B$, and half of the counts to the next bin $n = B+1$. A more precise calculation is not needed since this term contribution is already a first order correction to the final result, as it contributes by an amount $1-(1-\alpha)^D \approx D\alpha$). Thus, our second result is:

B, n	0	1	2	3	4	5	6	7	8	9
0	1.00000									
1		1.00000								
2			0.99954	0.00036						
3			0.00137	0.99601	0.00261					
4				0.00504	0.98750	0.00746				
5					0.01100	0.97459	0.01443			
6						0.01853	0.95874	0.02274		
7							0.02703	0.94120	0.03177	

Table B.1: Illustration of the spill over from main bins to neighbouring bins for mean clicks per ion $\mu = 100$.

Due to dark-state decay, there is spill-over from the main bin ($n = B$) to the next one ($n = B + 1$) by an amount of approximately $D\alpha/2 \approx \frac{DT}{2\tau}$.

Note that the worst case here is for $D = N$, as opposed to the Poissonian spill-over, which is largest when $B = N$. Furthermore, while the Poissonian spill-over is reduced by increasing T, the decay spill-over actually increases with T. Hence, there is a trade-off.

For $N = 16$, $T = 10$ms, and the previously used values for A and τ, we get a decay spill-over of $NT/(2\tau) = 0.08$, which is much larger than the corresponding Poisson spill-over of 0.003 (obtained using (B.7)). The optimal value of T, which has both worst-case spill-over contributions equal, lies at 5 ms for $N = 16$ ($\mu = 275$) and at 3.5 ms for $N = 8$ ($\mu = 190$). This corresponds to worst-case spill-over of 4% each for $N = 16$ and 1.5% each for $N = 8$.

Whichever reasonable value is chosen for T, we arrive at the final result that the two sources of error yield spill-over from the main bin $n = B$ in the neighbouring bins $n = B \pm 1$. The probabilities can be calculated using the formulae

$$P_N(n = B + 1|B, D) = (1 - D\alpha)(Q((B + \frac{3}{2})\mu, B\mu) - Q((B + \frac{1}{2})\mu, B\mu)) + \frac{D\alpha}{2} \quad \text{(B.8)}$$

$$P_N(n = B - 1|B, D) = (1 - D\alpha)(Q((B - \frac{1}{2})\mu, B\mu) - Q(\max(B - \frac{3}{2}, 0)\mu, B\mu)) \quad \text{(B.9)}$$

where $\alpha \approx T/\tau$ and $\mu = TA$. Note that the function $Q(a, z)$ is implemented in Mathematica as `GammaRegularized[a,z]`.

Appendix C

Considerations for a revised experimental setup

The presented work is not focussed only on the realisation of quantum states, operations, and algorithms but repeatedly stirs discussion on possible improvements for the employed apparatus. The measurements on the transition frequency $4s^2S_{1/2} - 3d^2D_{5/2}$ [135] as well as creating 14-particle entanglement [59] have provided a critical view on possible features for upcoming ion-trap quantum computers. Possible improvements with regards to the current experiment can be divided into three areas: (i) changes that would improve the trap or its vicinity such as the vacuum chamber, (ii) elements such as radio-frequency generators, rf-power sources, acousto-optical modulators, and similar devices, and (iii) statistical error sources at approximatly 1%.

Concerning trap and vacuum vessel possible improvements may be introduced by considering the following points:

- **Trap temperature**: For the majority of our experiments the temperature of the blades constituting the trap is of little importance. However, the unknown black body radiation emitted by the trap blades turned out to be the largest uncertainty in the error budget when determining the $S_{1/2} \leftrightarrow D_{5/2}$ transition frequency [135]. For an input power of about 9 W, the trap temperature is estimated to be 150±50 °C [65, p.102]. A vacuum-compatible temperature sensor would significantly lower this uncertainty and ought to be considered for a new trap design.

- **Trap frequency**: A change in temperature relates to a change in the mechanical dimensions of the trap size. This affects the electric fields and thus the trap frequencies. With typical temperature expansions of steel of about 10^{-5}/°C to 10^{-6}/°C, temperature changes by a few degrees will result in trap-frequency changes of several Hz, which is comparable to the linewidth of the laser resonant with the qubit transition, the linewidth of our laser and the corresponding precision of the current stabilisation for driving the magnetic field.

  Temperature changes are currently induced by lowering and raising the trap drive power. These changes in the trap-drive power are performed automatically during a "refreezing process". Should the count rate from the ion-string during the Doppler-cooling phase drop below a specified value, the computer control assumes that the crystal has melted. It will lower the RF power and tip voltages while shining in a strong light-field at 397 nm detuned by about 160 MHz to the red. This procedure is usually sufficient to recrystalise

the ion-string. However, when the RF power on the blades is lowered, the temperature of the trap changes also. Seeing that it takes several minutes for the trap to reach the original temperature again, the assumed trap frequency during that time window is off by several Hz (depending on the time that the RF trap power was lowered) with respect to the real trap frequency.

One possible solution would may be the following: The trap potential is only defined by the voltages on the surface of the electrodes. Instead of fabricating the trap blades from bulk material, it may be advantageous to fabricate the blades from ceramics with a low thermal expansion coefficient. These ceramics could then be coated with gold or a similar good conductor. Assembled, this trap would show the very same trap parameters as the original trap with blades produced from bulk metal - however with a notably smaller susceptibility of the trap frequency to temperature fluctuations.

- **Trap mount**: After the magnetic-field shield has been installed, the gain in coherence time was not as large as expected. During extensive searches for the reason of coherence times of only about 30 ms, floating the table was found to directly increase the coherence time up to the presented 100 ms. This result suggests that vibrations of the ion trap lead to decoherence. The stored ions follow the motion of the trap which influences the phase relation between the laser beam and the ion. Besides the trap mount, external vibrations, for instance from the helical resonator, could also couple to the ion trap. It might be beneficial to attach a small mirror or any other reflecting area onto a follow-up ion trap which could be used to investigate the trap stability by interference measurements.

- **Global ion-string illumination**: Addressing more and more ions with the global beam becomes more challenging the longer the ion-chain is. Instead of broadly illuminating the ion-string from the side, it would be advantageous to shine the laser light along the axis of the ion-string. The focus of the light field may remain constant independent of the size of the ion-string. Additionally, due to a more efficient momentum transfer the coupling to the axial sideband would become stronger.

Favourable improvements regarding the experimental controls are mainly concerned with control electronics for currents and laser fields:

- **Magnetic-field stability**: The atomic linewidth of the $S_{1/2} \leftrightarrow D_{1/2}$ transition is about 1 Hz. Consequently all parameters ought to be stable on a similar or better level. Ramsey experiments show that magnetic-field fluctuations contribute to a large extent to the coherence time in the experiment. The magnetic field is mainly determined by the current flowing through the magnetic-field coils. Considering a Zeeman splitting of a few MHz/G and the coils generating a magnetic field of about 2G/A, the current needs to be stabilized better than 10^{-5} at a mean current of about 1 A. The installed current-stabilisation is able to operate in that regime, yet a factor of 10 better stability would be desirable.

- **Laser-intensity fluctuations**: Including AC-Stark shift operations into the set of operations significantly lowered the effective addressing errors but also made the set of gates more sensitive to intensity fluctuations: addressing errors are provided in terms of relative Rabi frequencies between target and neighbour qubit and are roughly 3%. The rotation

angle of the AC-Stark operation (see Sec. 5.2.2), however, depends on the intensity, not the electric field. This leads to an effective addressing error on neighbouring ions for the AC-Stark gate of $(3\%)^2$. The drawback of the linear dependence of the rotation angle on the intensity is an increased sensitivity to intensity fluctuations. These are mainly caused by beam pointing instability, polarisation fluctuations and temperature changes in AOMs upon switching RF pulses on and off. With respect to beam-pointing instability, the setup has been improved by replacing the majority of the posts with pedestals. Polarisation problems solely depend on the quality of the installed optics and their alignment with respect to the quantisation axis. Heating effects in AOMs are currently investigated. Here, functionality of switching light fields on and off may be moved from AOMs to fibre-integrated Mach-Zehnder interferometers.

Infidelities in quantum state preparations of down to 1%[59, 99] started discussions about possible error sources contributing in general at that level. In the following, different sources are mentioned that may need to be considered in the future:

- **Evaluation precision**: The calibration of experimental parameters is performed at a precision of several percent, however usually not better than this. For instance Rabi frequencies on individual qubits and transitions are calibrated by driving 2.5 Rabi oscillations on the qubit, from which the Rabi frequency is inferred. The error bar on this measurement, however, is on the order of about 1%. A more precise calibration would require improvements with regards to intensity stabilisation, better measurement statistics as well as a generally enhanced measurement procedures to determine the Rabi frequency with higher precision.

- **Ancilla-mode-related Rabi frequency**: A calibration of Rabi frequencies on sidebands is currently not only limited from a statistical point of view. Secular modes couple to the sideband as a second-order term and influence the effective Rabi frequency according to

$$\Omega_{n_i,n_i+1} = \eta_i \Omega \sqrt{n_i+1}(1 - \sum_{l \neq i} \eta_l^2 (2n_l + 1)) \tag{C.1}$$

  with the Rabi frequency Ω_{n_i,n_i+1} on the sideband i described by the Lamb-Dicke parameter η_i at a population of n_i phonons in the presence of other modes described by their individual Lamb-Dicke parameters η_l and phonon populations of n_l. While this term scales quadratically with the Lamb-Dicke parameter of ancilla modes and is currently neglected, this may play a significant effect in larger quantum registers with more modes. Additional cooling of these spectator modes might be required.

- **Ancilla-mode-related frequency shifts**: Coupled modes not only influence the effective Rabi frequency but also may influence resonance frequencies. This effect has been investigated in detail in Ref. 136. Depending on the chosen transition, this effect may affect the performance of implemented quantum algorithms.

- **State initialisation**: State initialisation needs to work significantly better than 1%. Currently qubits are initialised using a σ-polarised beam along the quantisation axis of the magnetic field, coupling $S_{1/2} \leftrightarrow P_{1/2}$. This initialises the qubits with a probability of

>99.1% [Data07b]. Considering that this effect is estimated to have played a crucial role in the generation of W-states [20] and GHZ-states [59], alternative techniques ought to be considered to significantly improve the state initialisation.

- **Spontaneous decay during state detection**: This error source induces errors of a few percent depending on the number of ions investigated. There are means of detecting spontaneous decay happening during the detection [137], however these techniques may be hard to adapt for a CCD camera [138] - the key requirement for scalable quantum state detection.

It is notable that, despite all these error sources, our apparatus operates at extremely high fidelities as presented in several publications [59, 106, 128, 129]. This leads to the conclusion that there is still room for improvements which allows us to increase the complexity of quantum information processing (and related experiments) in the upcoming years.

Appendix D

Journal publications

The work of this thesis resulted in numerous publications in the field of quantum information processing:

- "14-qubit entanglement: creation and coherence", **T. Monz**, P. Schindler, J. T. Barreiro, M. Chwalla, D. Nigg, W. A. Coish, M. Harlander, W. Hänsel, M. Hennrich, and R. Blatt , Phys. Rev. Lett. 106 , 130506 (2011)
- "Realization of universal ion-trap quantum computation with decoherence-free qubits", **T. Monz**, K. Kim, A. S. Villar, P. Schindler, M. Chwalla, M. Riebe, C. F. Roos, H. Häffner, W. Hänsel, M. Hennrich, and R. Blatt, Phys. Rev. Lett. 103, 200503 (2009)
- "Realization of the quantum Toffoli gate with trapped ions", **T. Monz**, K. Kim, W. Hänsel, M. Riebe, A. S. Villar, P. Schindler, M. Chwalla, M. Hennrich, and R. Blatt, Phys. Rev. Lett. 102, 040501 (2009)
- "Deterministic entanglement swapping with an ion trap quantum computer", M. Riebe, **T. Monz**, A. S. Villar, P. Schindler, M. Chwalla, M. Hennrich, and R. Blatt, Nature Physics 4, 839 (2008)
- "Process tomography of ion trap quantum gates", M. Riebe, K. Kim, P. Schindler, **T. Monz**, P. O. Schmidt, T. K. Körber, W. Hänsel, H. Häffner, C. F. Roos, and R. Blatt, Phys. Rev. Lett. 97, 220407 (2006)

In the framework of this thesis, additional publications in a more general context have been

- "Experimental repetitive quantum error correction", P. Schindler, J. T. Barreiro, **T. Monz**, V. Nebendahl, D. Nigg, M. Chwalla, M. Hennrich, and R. Blatt , Science 332, 1059-1061 (2011)
- "An open-system quantum simulator with trapped ions", J. T. Barreiro, M. Müller, P. Schindler, D. Nigg, **T. Monz**, M. Chwalla, M. Hennrich, C. F. Roos, P. Zoller, and R. Blatt, Nature 470, 486 (2011)
- "Experimental multiparticle entanglement dynamics induced by decoherence", J. T. Barreiro, P. Schindler, O. Gühne, **T. Monz**, M. Chwalla, C. F. Roos, M. Hennrich, and R. Blatt, Nature Physics 6, 943 (2010)

- "Raman spectroscopy of a single ion coupled to a high-finesse cavity", C. Russo, H.G. Barros, A. Stute, F. Dubin, E.S. Phillips, **T. Monz**, T.E. Northup, C. Becher, T. Salzburger, H. Ritsch, P.O. Schmidt, and R. Blatt, Appl. Phys. B 95, 205 (2009)

- "Absolute frequency measurement of the $^{40}Ca^{+}$ $4s^2S_{1/2}$ - $3d^2D_{5/2}$ clock transition", M. Chwalla, J. Benhelm, K. Kim, G. Kirchmair, **T. Monz**, M. Riebe, P. Schindler, A. S. Villar, W. Hänsel, C. F. Roos, R. Blatt, M. Abgrall, G. Santarelli, G. D. Rovera, and Ph. Laurent, Phys. Rev. Lett. 102, 023002 (2009)

- "Nonlinear coupling of continuous variables at the single quantum level", C. F. Roos, **T. Monz**, K. Kim, M. Riebe, H. Häffner, D. F. V. James, and R. Blatt, Phys. Rev. A 77, 040302(R) (2008)

- "Precision spectroscopy with two correlated atoms", M. Chwalla, K. Kim, **T. Monz**, P. Schindler, M. Riebe, C. F. Roos, and R. Blatt, Appl. Phys. B 89, 483 (2007)

Appendix E

Data sets

A large number of experiments discussed in this thesis is referenced in the following to facilitate reevaluation or additional investigations. A brief title serves as a reminder of the experiment to which a data set refers. Subsequently time tags as well as the measurement day are presented. Here, a time tag indicates when an experiment was finished and directly corresponds to the file name of the data stored on the laboratory computer as well as on the back-up server. References to extensive measurements that consist of several data sets are shortened to the start and end time. In these cases, the specific time tags need to be extracted from the laboratory note book.

Data sets investigated

[Data07a] Bell state generation based on a geometric phase gate. *Time: populations - 1220; parity - 1218*, November 7^{th}, 2007.

[Data07b] Efficiency of optical pumping. *Time: 1714-1735*, November 15^{th}, 2007.

[Data07c] Entanglement swapping including deterministic correcting pulses. *time: 1745*, October 4^{th}, 2007.

[Data07d] Entanglement swapping without deterministic correcting pulses. *time: 1750*, October 4^{th}, 2007.

[Data07e] Four-qubit GHZ employing higher vibrational excitations. *Time: 0847*, October 4^{th}, 2007.

[Data07f] Process tomography of a CNOT gate operation acting within a DFS. *Time: 1732 - 2059*, November 29^{th}, 2007.

[Data07g] Process tomography of the geometric phase gate. *Time: 1212*, November 7^{th}, 2007.

[Data07h] Three-qubit GHZ employing higher vibrational excitations. *Time: 2110*, October 4^{th}, 2007.

[Data07i] Toffoli gate operation based on a multi-phonon phase gate. *Time: 2124-1520*, September 19^{th} and 20^{th}, 2007.

[Data07j] Toffoli gate operation based on a short phase gate. *Time: 1153-1829*, September 19^{th}, 2007.

[Data07k] Toffoli gate operation based on the four-pulse composite phase gate. *Time: 0540*, September 14^{th}, 2007.

[Data08] Two-qubit W-state generation using the global beam. *Time: 1812*, July 3^{rd}, 2008.

[Data09a] Coherence decay of a 2-qubit GHZ state. *single-qubit reference: 1256-1339, ghz: 1128-1231*, June 23^{th}, 2009.

[Data09b] Coherence decay of a 3-qubit GHZ state. *single-qubit reference: 1327-1423, ghz: 1230-1326*, June 24^{th}, 2009.

[Data09c] Coherence decay of a 4-qubit GHZ state. *single-qubit reference: 1152-1228, ghz: 1115-1149*, July 3^{rd}, 2009.

[Data09d] Coherence decay of a 6-qubit GHZ state. *single-qubit reference: 1256-1339, ghz: 2003-2126*, June 23^{rd}, 2009.

[Data09e] Coherence decay of a 8-qubit GHZ state. *single-qubit reference: 0702-0802 (July 8^{th}, ghz: 2316-2347*, July 7^{th}, 2009.

[Data09f] Eight-qubit GHZ-state creation based on the Mølmer-Sørensen gate. *parity: 1431, populations: 1437*, April 15^{th}, 2009.

[Data09g] Four-qubit GHZ-state creation based on the Mølmer-Sørensen gate. *parity: 1044, populations: 1032*, July 22^{th}, 2009.

[Data09h] Local equivalent to a 8-qubit GHZ state in a decoherence-free subspace. *Time: 0047 - 0303*, July 8^{th}, 2009.

[Data09i] Six-qubit GHZ-state creation based on the Mølmer-Sørensen gate. *parity: 1709, populations: 1713*, April 14^{th}, 2009.

[Data09j] Three-qubit GHZ-state creation based on the Mølmer-Sørensen gate. *parity: 1523, populations: 1450*, June 24^{th}, 2009.

[Data09k] Two-qubit GHZ-state creation based on the Mølmer-Sørensen gate. *parity: 1058, populations: 1104*, June 23^{th}, 2009.

[Data10a] Beat measurement between three lasers to estimate the laser linewidth. *Time: 1410*, June 30^{th}, 2010.

[Data10b] Five-qubit GHZ-state creation based on the Mølmer-Sørensen gate. *parity: 2325, populations: 2320*, August 11^{th}, 2010.

[Data10c] Four-qubit W-state generation using the global beam. *Time: 1846*, December 29^{th}, 2010.

[Data10d] Fourteen-qubit GHZ-state creation based on the Mølmer-Sørensen gate. *parity: 2130, populations: 2132*, February 2^{nd}, 2010.

[Data10e] Ramsey contrast in comparison to predictions based on magnetic field measurements. *time: 1358-1750, 2010-2300*, January 21^{th}, 2010.

[Data10f] Ramsey decay of the S(m=-1/2) $\leftrightarrow$ D(m=-1/2) and S(m=-1/2) $\leftrightarrow$ D(m=-5/2) transition. *Time: 2006-2235*, February 1^{st}, 2010.

[Data10g] Spectrum of a single ion in a linear Paul trap. *Time: 1001*, June 12^{th}, 2010.

[Data10h] Ten-qubit GHZ-state creation based on the Mølmer-Sørensen gate. *parity: 1403, populations: 1341*, January 27^{th}, 2010.

[Data10i] Twelve-qubit GHZ-state creation based on the Mølmer-Sørensen gate. *parity: 1550, populations: 1538*, February 2^{nd}, 2010.

List of Sequences

Bibliography

[1] A. Einstein, Annalen der Physik **322**, 132 (1905), ISSN 1521-3889, URL http://dx.doi.org/10.1002/andp.19053220607.

[2] E. Schrödinger, Physical Review Online Archive (Prola) **28**, 1049 (1926), URL http://dx.doi.org/10.1103/PhysRev.28.1049.

[3] E. Schrödinger, The British Journal for the Philosophy of Science **III**, 233 (1952), ISSN 1464-3537, URL http://dx.doi.org/10.1093/bjps/III.11.233.

[4] P. Wolfgang and H. Steinwedel, Zeitschrift für Naturforschung A **8**, 448 (1953).

[5] W. Neuhauser, M. Hohenstatt, P. E. Toschek, and H. Dehmelt, Physical Review A **22**, 1137 (1980), URL http://dx.doi.org/10.1103/PhysRevA.22.1137.

[6] W. Nagourney, J. Sandberg, and H. Dehmelt, Physical Review Letters **56**, 2797 (1986), URL http://dx.doi.org/10.1103/PhysRevLett.56.2797.

[7] T. Sauter, W. Neuhauser, R. Blatt, and P. E. Toschek, Physical Review Letters **57**, 1696 (1986), URL http://dx.doi.org/10.1103/PhysRevLett.57.1696.

[8] J. C. Bergquist, R. G. Hulet, W. M. Itano, and D. J. Wineland, Physical Review Letters **57**, 1699 (1986), URL http://dx.doi.org/10.1103/PhysRevLett.57.1699.

[9] D. Deutsch, Proceedings of the Royal Society of London. A. Mathematical and Physical Sciences **400**, 97 (1985), URL http://dx.doi.org/10.1098/rspa.1985.0070.

[10] P. W. Shor, Foundations of Computer Science, 1994 Proceedings., 35th Annual Symposium on pp. 124–134 (1994), URL http://ieeexplore.ieee.org/xpls/abs_all.jsp?arnumber=365700.

[11] L. K. Grover, Physical Review Letters **79**, 325 (1997), URL http://dx.doi.org/10.1103/PhysRevLett.79.325.

[12] D. P. DiVincenzo, Fortschr. Phys. **48**, 771 (2000), ISSN 1521-3978, URL http://dx.doi.org/10.1002/1521-3978(200009)48:9/11%3C771::AID-PROP771%3E3.0.CO;2-E.

[13] R. Feynman, International Journal of Theoretical Physics **21**, 467 (1982), ISSN 0020-7748, URL http://dx.doi.org/10.1007/BF02650179.

[14] S. Lloyd, Science **273**, 1073 (1996), URL http://dx.doi.org/10.1126/science.273.5278.1073.

[15] D. J. Wineland, J. J. Bollinger, W. M. Itano, and D. J. Heinzen, Physical Review A **50**, 67 (1994), URL http://dx.doi.org/10.1103/PhysRevA.50.67.

[16] K. Southwell, Nature **453**, 1003 (2008), ISSN 0028-0836, URL http://dx.doi.org/10.1038/4531003a.

[17] H. Dehmelt, Bulletin of the American Physical Society **20**, 60 (1975), ISSN 0003-0503.

[18] F. Schmidt-Kaler, H. Häffner, M. Riebe, S. Gulde, G. P. T. Lancaster, T. Deuschle, C. Becher, C. F. Roos, J. Eschner, and R. Blatt, Nature **422**, 408 (2003), ISSN 0028-0836, URL http://dx.doi.org/10.1038/nature01494.

[19] M. Riebe, H. Häffner, C. Roos, W. Hänsel, J. Benhelm, G. Lancaster, T. Körber, C. Becher, F. Schmidt-Kaler, D. James, et al., Nature **429**, 734 (2004), ISSN 0028-0836, URL http://dx.doi.org/10.1038/nature02570.

[20] H. Häffner, W. Hänsel, C. Roos, J. Benhelm, D. Chek-al kar, M. Chwalla, T. Körber, U. Rapol, M. Riebe, P. O. Schmidt, et al., Nature **438**, 643 (2005), ISSN 0028-0836, URL http://dx.doi.org/10.1038/nature04279.

[21] M. Born, Zeitschrift für Physik A Hadrons and Nuclei **37**, 863 (1926), ISSN 1434-6001, URL http://dx.doi.org/10.1007/BF01397477.

[22] R. Horodecki, P. Horodecki, M. Horodecki, and K. Horodecki, Reviews of Modern Physics **81**, 865 (2009), ISSN 0034-6861, URL http://dx.doi.org/10.1103/RevModPhys.81.865.

[23] D. M. Greenberger, M. A. Horne, and A. Zeilinger, quant-ph/0712.0921 (2007), URL http://arxiv.org/abs/0712.0921.

[24] C. F. Roos, M. Riebe, H. Häffner, W. Hänsel, J. Benhelm, G. P. T. Lancaster, C. Becher, F. Schmidt-Kaler, and R. Blatt, Science **304**, 1478 (2004), URL http://dx.doi.org/10.1126/science.1097522.

[25] M. Eibl, N. Kiesel, M. Bourennane, C. Kurtsiefer, and H. Weinfurter, Physical Review Letters **92**, 077901+ (2004), URL http://dx.doi.org/10.1103/PhysRevLett.92.077901.

[26] N. A. Peters, T. C. Wei, and P. G. Kwiat, Physical Review A **70**, 052309+ (2004), URL http://dx.doi.org/10.1103/PhysRevA.70.052309.

[27] L. Gurvits and H. Barnum, Physical Review A **66**, 062311+ (2002), URL http://dx.doi.org/10.1103/PhysRevA.66.062311.

[28] R. Hildebrand, quant-ph/0601201 (2006), URL http://arxiv.org/abs/quant-ph/0601201.

[29] M. A. Nielsen and I. L. Chuang, *Quantum Computation and Quantum Information* (Cambridge University Press, 2000), ISBN 0521635039, URL http://www.amazon.com/gp/product/0521635039.

[30] V. Vedral, M. B. Plenio, M. A. Rippin, and P. L. Knight, Physical Review Letters **78**, 2275 (1997), URL http://dx.doi.org/10.1103/PhysRevLett.78.2275.

[31] W. K. Wootters, Physical Review Letters **80**, 2245 (1998), URL http://dx.doi.org/10.1103/PhysRevLett.80.2245.

[32] V. Coffman, J. Kundu, and W. K. Wootters, Physical Review A **61**, 052306+ (2000), URL http://dx.doi.org/10.1103/PhysRevA.61.052306.

[33] V. Vedral, Reviews of Modern Physics **74**, 197 (2002), URL http://dx.doi.org/10.1103/RevModPhys.74.197.

[34] A. Gilchrist, N. K. Langford, and M. A. Nielsen, Physical Review A **71**, 062310+ (2009), URL http://dx.doi.org/10.1103/PhysRevA.71.062310.

[35] R. Jozsa, Journal of Modern Optics **41**, 2315 (1994), URL http://dx.doi.org/10.1080/09500349414552171.

[36] A. Uhlmann, Reports on Mathematical Physics **9**, 273 (1976), ISSN 00344877, URL http://dx.doi.org/10.1016/0034-4877(76)90060-4.

[37] G. Vidal and R. F. Werner, Physical Review A **65**, 032314+ (2002), URL http://dx.doi.org/10.1103/PhysRevA.65.032314.

[38] A. Jamiolkowski, Reports on Mathematical Physics **3**, 275 (1972), ISSN 00344877, URL http://dx.doi.org/10.1016/0034-4877(72)90011-0.

[39] M. Choi, Linear Algebra and its Applications **10**, 285 (1975), ISSN 00243795, URL http://dx.doi.org/10.1016/0024-3795(75)90075-0.

[40] K. Zyczkowski and H.-J. Sommers, Journal of Physics A: Mathematical and General **34**, 7111+ (2001), ISSN 0305-4470, URL http://dx.doi.org/10.1088/0305-4470/34/35/335.

[41] M. Horodecki, P. Horodecki, and R. Horodecki, Physical Review A **60**, 1888 (1999), URL http://dx.doi.org/10.1103/PhysRevA.60.1888.

[42] S. T. Flammia and Y. K. Liu, Physical Review Letters **106**, 230501+ (2011), URL http://dx.doi.org/10.1103/PhysRevLett.106.230501.

[43] M. P. da Silva, O. Landon-Cardinal, and D. Poulin (2011), 1104.3835, URL http://arxiv.org/abs/1104.3835.

[44] A. Shabani, R. L. Kosut, M. Mohseni, H. Rabitz, M. A. Broome, M. P. Almeida, A. Fedrizzi, and A. G. White, Physical Review Letters **106**, 100401+ (2011), URL http://dx.doi.org/10.1103/PhysRevLett.106.100401.

[45] P.-S. Laplace, *Essai philosophique sur les probabilités* (1814).

[46] M. S. Kaznady and D. F. V. James, Physical Review A **79** (2009), URL http://scitation.aip.org/getabs/servlet/GetabsServlet?prog=normal&id=PLRAAN000079000002022109000001&idtype=cvips&gifs=yes.

[47] J. A. Smolin, J. M. Gambetta, and G. Smith (2011), 1106.5458, URL http://arxiv.org/abs/1106.5458.

[48] M. Ježek, J. Fiurášek, and Z. Hradil, Physical Review A **68**, 012305+ (2003), URL http://dx.doi.org/10.1103/PhysRevA.68.012305.

[49] D. Gross, Y. K. Liu, S. T. Flammia, S. Becker, and J. Eisert, Physical Review Letters **105**, 150401+ (2010), URL http://dx.doi.org/10.1103/PhysRevLett.105.150401.

[50] S. Flammia (2011), private communication.

[51] K. M. R. Audenaert and S. Scheel, New Journal of Physics **11**, 023028+ (2009), ISSN 1367-2630, URL http://dx.doi.org/10.1088/1367-2630/11/2/023028.

[52] Y. S. Teo, H. Zhu, B. G. Englert, J. Řeháček, and Z. Hradil, Physical Review Letters **107**, 020404+ (2011), URL http://dx.doi.org/10.1103/PhysRevLett.107.020404.

[53] R. B. Kohout, Physical Review Letters **105**, 200504+ (2010), URL http://dx.doi.org/10.1103/PhysRevLett.105.200504.

[54] P. Gregory, *Bayesian Logical Data Analysis for the Physical Sciences: A Comparative Approach with Mathematica Support* (Cambridge University Press, 2005), ISBN 052184150X, URL http://www.amazon.com/exec/obidos/redirect?tag=citeulike07-20&path=ASIN/052184150X.

[55] K. M. R. Audenaert and S. Scheel, New Journal of Physics **11**, 113052+ (2009), ISSN 1367-2630, URL http://dx.doi.org/10.1088/1367-2630/11/11/113052.

[56] D. Simon, *Optimal State Estimation: Kalman, H Infinity, and Nonlinear Approaches* (Wiley & Sons, 2006), 1st ed., ISBN 0471708585, URL http://www.amazon.com/Optimal-State-Estimation-Nonlinear-Approaches/dp/0471708585.

[57] M. Mohseni, A. T. Rezakhani, and D. A. Lidar, Physical Review A **77**, 032322+ (2008), URL http://dx.doi.org/10.1103/PhysRevA.77.032322.

[58] M. Mohseni and D. A. Lidar, Physical Review Letters **97**, 170501+ (2006), URL http://dx.doi.org/10.1103/PhysRevLett.97.170501.

[59] T. Monz, P. Schindler, J. T. Barreiro, M. Chwalla, D. Nigg, W. A. Coish, M. Harlander, W. Hänsel, M. Hennrich, and R. Blatt, Physical Review Letters **106**, 130506+ (2011), URL http://dx.doi.org/10.1103/PhysRevLett.106.130506.

[60] M. Richter (2010), Priv. comm.; The Cray XT5-HE (Jaguar) can store a 43-qubit quantum state.

[61] R. F. Wuerker, H. Shelton, and R. V. Langmuir, Journal of Applied Physics **30**, 342 (1959), URL http://scitation.aip.org/getabs/servlet/GetabsServlet?prog=normal&id=JAPIAU000030000003000342000001&idtype=cvips&gifs=yes.

[62] F. Schmidt-Kaler, H. Häffner, S. Gulde, M. Riebe, G. P. T. Lancaster, T. Deuschle, C. Becher, W. Hänsel, J. Eschner, C. F. Roos, et al., Applied Physics B: Lasers and Optics **77**, 789 (2003), ISSN 0946-2171, URL http://dx.doi.org/10.1007/s00340-003-1346-9.

[63] S. Gulde, Ph.D. thesis, University of Innsbruck, Austria (2003), URL http://heart-c704.uibk.ac.at/publications/dissertation/gulde_diss.pdf.

[64] M. Riebe, Ph.D. thesis, University of Innsbruck, Austria (2005), URL http://heart-c704.uibk.ac.at/publications/dissertation/riebe_diss.pdf.

[65] M. Chwalla, Ph.D. thesis, University of Innsbruck, Austria (2009), URL http://heart-c704.uibk.ac.at/publications/dissertation/chwalla_diss.pdf.

[66] P. Schindler, Master's thesis, University of Innsbruck, Austria (2008), URL http://heart-c704.uibk.ac.at/publications/diploma/diplom_schindler.pdf.

[67] J. I. Cirac and P. Zoller, Physical Review Letters **74**, 4091 (1995), URL http://dx.doi.org/10.1103/PhysRevLett.74.4091.

[68] D. F. V. James, Applied Physics B: Lasers and Optics **66**, 181 (1998), ISSN 0946-2171, URL http://dx.doi.org/10.1007/s003400050373.

[69] P. A. Barton, C. J. S. Donald, D. M. Lucas, D. A. Stevens, A. M. Steane, and D. N. Stacey, Physical Review A **62**, 032503+ (2000), URL http://dx.doi.org/10.1103/PhysRevA.62.032503.

[70] A. Kreuter, C. Becher, G. P. T. Lancaster, A. B. Mundt, C. Russo, H. Häffner, C. Roos, W. Hänsel, F. S. Kaler, R. Blatt, et al., Physical Review A **71**, 032504+ (2005), URL http://dx.doi.org/10.1103/PhysRevA.71.032504.

[71] J. Home, Ph.D. thesis, Linacre College, Oxford, United Kingdom (2006), URL www.physics.ox.ac.uk/users/iontrap/pubs/theses/JHomethesis.pdf.

[72] D. Rotter, Master's thesis, University of Innsbruck, Austria (2003), URL http://heart-c704.uibk.ac.at/publications/diploma/diplom_rotter.pdf.

[73] R. Lechner, Master's thesis, University of Innsbruck, Austria (2010), URL http://heart-c704.uibk.ac.at/publications/diploma/diplom_rechner.pdf.

[74] A. Kastler, Journal de Physique et le Radium **11**, 255 (1950), ISSN 0368-3842, URL http://dx.doi.org/10.1051/jphysrad:01950001106025500.

[75] Y. Zel'dovich, JETP Letters **19**, 74 (1974).

[76] D. Wineland and H. Dehmelt, Bulletin of the American Physical Society **20**, 637 (1975), ISSN 0003-0503.

[77] C. Roos, T. Zeiger, H. Rohde, H. C. Nägerl, J. Eschner, D. Leibfried, F. S. Kaler, and R. Blatt, Physical Review Letters **83**, 4713 (1999), URL http://dx.doi.org/10.1103/PhysRevLett.83.4713.

[78] H. Rohde, S. T. Gulde, C. F. Roos, P. A. Barton, D. Leibfried, E. Eschner, F. Schmidt-Kaler, and R. Blatt, Journal of Optics B: Quantum and Semiclassical Optics **3**, 34+ (2001), URL http://iopscience.iop.org/1464-4266/3/1/357/.

[79] W. Neuhauser, M. Hohenstatt, P. Toschek, and H. Dehmelt, Physical Review Letters **41**, 233 (1978), URL http://dx.doi.org/10.1103/PhysRevLett.41.233.

[80] C. Roos, Ph.D. thesis, University of Innsbruck, Austria (2000), URL http://heart-c704.uibk.ac.at/publications/dissertation/roos_diss.pdf.

[81] S. Stenholm, Reviews of Modern Physics **58**, 699+ (1986), URL http://dx.doi.org/10.1103/RevModPhys.58.699.

[82] G. W. F. Drake, *Atomic, Molecular, & Optical Physics Handbook* (Amer Inst of Physics, 1996), ISBN 156396242X, URL http://www.amazon.com/gp/product/156396242X.

[83] H. Häffner, S. Gulde, M. Riebe, G. Lancaster, C. Becher, J. Eschner, F. S. Kaler, and R. Blatt, Physical Review Letters **90**, 143602+ (2003), URL http://dx.doi.org/10.1103/PhysRevLett.90.143602.

[84] N. F. Ramsey, Reviews of Modern Physics **62**, 541 (1990), URL http://dx.doi.org/10.1103/RevModPhys.62.541.

[85] L. Allen and J. H. Eberly, *Optical Resonance and Two-Level Atoms* (Dover Publications, 1987), soft cover ed., ISBN 0486655334, URL http://www.amazon.com/exec/obidos/redirect?tag=citeulike07-20&path=ASIN/0486655334.

[86] L. M. K. Vandersypen and I. L. Chuang, Reviews of Modern Physics **76**, 1037 (2005), URL http://dx.doi.org/10.1103/RevModPhys.76.1037.

[87] V. Nebendahl, Master's thesis, University of Innsbruck, Austria (2008), URL http://heart-c704.uibk.ac.at/publications/diploma/diplom_nebendahl.pdf.

[88] D. P. DiVincenzo, Physical Review A **51**, 1015 (1995), URL http://dx.doi.org/10.1103/PhysRevA.51.1015.

[89] T. Sleator and H. Weinfurter, Physical Review Letters **74**, 4087 (1995), URL http://dx.doi.org/10.1103/PhysRevLett.74.4087.

[90] M. Riebe, K. Kim, P. Schindler, T. Monz, P. O. Schmidt, T. K. Körber, W. Hänsel, H. Häffner, C. F. Roos, and R. Blatt, Physical Review Letters **97** (2006), URL http://dx.doi.org/10.1103/PhysRevLett.97.220407.

[91] F. Schmidt-Kaler, H. Häffner, S. Gulde, M. Riebe, G. Lancaster, J. Eschner, C. Becher, and R. Blatt, Europhysics Letters pp. 587+ (2004), URL http://dx.doi.org/10.1209/epl/i2003-10174-3.

[92] S. Gulde, M. Riebe, G. P. T. Lancaster, C. Becher, J. Eschner, H. Häffner, F. Schmidt-Kaler, I. L. Chuang, and R. Blatt, Nature **421**, 48 (2003), ISSN 0028-0836, URL http://dx.doi.org/10.1038/nature01336.

[93] L. M. K. Vandersypen, M. Steffen, G. Breyta, C. S. Yannoni, M. H. Sherwood, and I. L. Chuang, Nature **414**, 883 (2001), ISSN 0028-0836, URL http://dx.doi.org/10.1038/414883a.

[94] A. Barenco, C. H. Bennett, R. Cleve, D. P. DiVincenzo, N. Margolus, P. Shor, T. Sleator, J. A. Smolin, and H. Weinfurter, Physical Review A **52**, 3457 (1995), URL http://dx.doi.org/10.1103/PhysRevA.52.3457.

[95] V. V. Shende and I. L. Markov, quant-ph/0803.2316 (2008), URL http://arxiv.org/abs/0803.2316.

[96] T. C. Ralph, K. J. Resch, and A. Gilchrist, Physical Review A **75**, 022313+ (2007), URL http://dx.doi.org/10.1103/PhysRevA.75.022313.

[97] B. P. Lanyon, M. Barbieri, M. P. Almeida, T. Jennewein, T. C. Ralph, K. J. Resch, G. J. Pryde, J. L. O'Brien, A. Gilchrist, and A. G. White, Nature Physics **5**, 134 (2008), ISSN 1745-2473, URL http://dx.doi.org/10.1038/nphys1150.

[98] A. Sørensen and K. Mølmer, Physical Review A **62**, 022311+ (2000), URL http://dx.doi.org/10.1103/PhysRevA.62.022311.

[99] J. Benhelm, G. Kirchmair, C. F. Roos, and R. Blatt, Nature Physics **4**, 463 (2008), ISSN 1745-2473, URL http://dx.doi.org/10.1038/nphys961.

[100] G. Kirchmair, J. Benhelm, F. Zähringer, R. Gerritsma, C. F. Roos, and R. Blatt, New Journal of Physics **11**, 023002+ (2009), ISSN 1367-2630, URL http://dx.doi.org/10.1088/1367-2630/11/2/023002.

[101] C. F. Roos, New Journal of Physics **10**, 013002+ (2008), ISSN 1367-2630, URL http://dx.doi.org/10.1088/1367-2630/10/1/013002.

[102] D. Leibfried, B. DeMarco, V. Meyer, D. Lucas, M. Barrett, J. Britton, W. M. Itano, B. Jelenkovic, C. Langer, T. Rosenband, et al., Nature **422**, 412 (2003), URL http://dx.doi.org/10.1038/nature01492.

[103] K. Kim, C. F. Roos, L. Aolita, H. Häffner, V. Nebendahl, and R. Blatt, Physical Review A **77** (2008), URL http://scitation.aip.org/getabs/servlet/GetabsServlet?prog=normal&id=PLRAAN000077000005050303000001&idtype=cvips&gifs=yes.

[104] J. Benhelm, Ph.D. thesis, University of Innsbruck, Austria (2008), URL http://heart-c704.uibk.ac.at/publications/dissertation/benhelm_diss.pdf.

[105] D. Leibfried, E. Knill, S. Seidelin, J. Britton, R. B. Blakestad, J. Chiaverini, D. B. Hume, W. M. Itano, J. D. Jost, C. Langer, et al., Nature **438**, 639 (2005), ISSN 0028-0836, URL http://dx.doi.org/10.1038/nature04251.

[106] P. Schindler, J. T. Barreiro, T. Monz, V. Nebendahl, D. Nigg, M. Chwalla, M. Hennrich, and R. Blatt, Science **332**, 1059 (2011), URL http://dx.doi.org/10.1126/science.1203329.

[107] M. Riebe, T. Monz, K. Kim, A. Villar, P. Schindler, M. Chwalla, M. Hennrich, and R. Blatt, Nature Physics **4**, 839 (2008), ISSN 1745-2473, URL http://dx.doi.org/10.1038/nphys1107.

[108] Hume, D. B., Chou, C. W., Rosenband, T., and Wineland, D. J., Physical Review A **80**, 052302+ (2009), URL http://dx.doi.org/10.1103/PhysRevA.80.052302.

[109] C. A. Sackett, D. Kielpinski, B. E. King, C. Langer, V. Meyer, C. J. Myatt, M. Rowe, Q. A. Turchette, W. M. Itano, D. J. Wineland, et al., Nature **404**, 256 (2000), ISSN 0028-0836, URL http://dx.doi.org/10.1038/35005011.

[110] M. Huber and M. Plesch, quant-ph/1103.4294 (2011), URL http://arxiv.org/abs/1103.4294.

[111] W. Dür and J. I. Cirac, Journal of Physics A: Mathematical and General **34**, 6837 (2001), ISSN 0305-4470, URL http://dx.doi.org/10.1088/0305-4470/34/35/310.

[112] O. Gühne and M. Seevinck, New Journal of Physics **12**, 053002+ (2010), ISSN 1367-2630, URL http://dx.doi.org/10.1088/1367-2630/12/5/053002.

[113] M. Żukowski, A. Zeilinger, M. A. Horne, and A. K. Ekert, Physical Review Letters **71**, 4287 (1993), URL http://dx.doi.org/10.1103/PhysRevLett.71.4287.

[114] B. Yurke and D. Stoler, Physical Review A **46**, 2229 (1992), URL http://dx.doi.org/10.1103/PhysRevA.46.2229.

[115] J. J. Garcia-Ripoll, P. Zoller, and J. I. Cirac, Physical Review Letters **91**, 157901+ (2003), URL http://dx.doi.org/10.1103/PhysRevLett.91.157901.

[116] D. Hayes, D. N. Matsukevich, P. Maunz, D. Hucul, Q. Quraishi, S. Olmschenk, W. Campbell, J. Mizrahi, C. Senko, and C. Monroe, Physical Review Letters **104**, 140501+ (2010), URL http://dx.doi.org/10.1103/PhysRevLett.104.140501.

[117] W. C. Campbell, J. Mizrahi, Q. Quraishi, C. Senko, D. Hayes, D. Hucul, D. N. Matsukevich, P. Maunz, and C. Monroe, Physical Review Letters **105**, 090502+ (2010), URL http://dx.doi.org/10.1103/PhysRevLett.105.090502.

[118] P. Zanardi and M. Rasetti, Physical Review Letters **79**, 3306 (1997), URL http://dx.doi.org/10.1103/PhysRevLett.79.3306.

[119] D. A. Lidar, I. L. Chuang, and K. B. Whaley, Physical Review Letters **81**, 2594 (1998), URL http://dx.doi.org/10.1103/PhysRevLett.81.2594.

[120] P. G. Kwiat, A. J. Berglund, J. B. Altepeter, and A. G. White, Science **290**, 498 (2000), URL http://dx.doi.org/10.1126/science.290.5491.498.

[121] M. Bourennane, M. Eibl, S. Gaertner, C. Kurtsiefer, A. Cabello, and H. Weinfurter, Physical Review Letters **92**, 107901+ (2004), URL http://dx.doi.org/10.1103/PhysRevLett.92.107901.

[122] L. Viola, E. M. Fortunato, M. A. Pravia, E. Knill, R. Laflamme, and D. G. Cory, Science **293**, 2059 (2001), URL http://dx.doi.org/10.1126/science.1064460.

[123] D. Kielpinski, V. Meyer, M. A. Rowe, C. A. Sackett, W. M. Itano, C. Monroe, and D. J. Wineland, Science **291**, 1013 (2001), URL http://dx.doi.org/10.1126/science.1057357.

[124] C. F. Roos, G. P. T. Lancaster, M. Riebe, H. Häffner, W. Hänsel, S. Gulde, C. Becher, J. Eschner, F. S. Kaler, and R. Blatt, Physical Review Letters **92**, 220402+ (2004), URL http://dx.doi.org/10.1103/PhysRevLett.92.220402.

[125] H. Häffner, F. Schmidt-Kaler, W. Hänsel, C. F. Roos, T. Körber, M. Chwalla, M. Riebe, J. Benhelm, U. D. Rapol, C. Becher, et al., Applied Physics B: Lasers and Optics **81**, 151 (2005), ISSN 0946-2171, URL http://dx.doi.org/10.1007/s00340-005-1917-z.

[126] T. Monz, K. Kim, A. S. Villar, P. Schindler, M. Chwalla, M. Riebe, C. F. Roos, H. Häffner, W. Hänsel, M. Hennrich, et al., Physical Review Letters **103**, 200503+ (2009), URL http://dx.doi.org/10.1103/PhysRevLett.103.200503.

[127] T. Monz, K. Kim, W. Hänsel, M. Riebe, A. S. Villar, P. Schindler, M. Chwalla, M. Hennrich, and R. Blatt, Physical Review Letters **102**, 040501+ (2009), URL http://dx.doi.org/10.1103/PhysRevLett.102.040501.

[128] J. T. Barreiro, P. Schindler, O. Gühne, T. Monz, M. Chwalla, C. F. Roos, M. Hennrich, and R. Blatt, Nature Physics **6**, 943 (2010), ISSN 1745-2473, URL http://dx.doi.org/10.1038/nphys1781.

[129] J. T. Barreiro, M. Muller, P. Schindler, D. Nigg, T. Monz, M. Chwalla, M. Hennrich, C. F. Roos, P. Zoller, and R. Blatt, Nature **470**, 486 (2011), ISSN 0028-0836, URL http://dx.doi.org/10.1038/nature09801.

[130] D. Kielpinski, C. Monroe, and D. J. Wineland, Nature **417**, 709 (2002), ISSN 0028-0836, URL http://dx.doi.org/10.1038/nature00784.

[131] L. Mandel and E. Wolf, *Optical Coherence and Quantum Optics* (Cambridge University Press, 1995), ISBN 0521417112, URL http://www.amazon.com/gp/product/0521417112.

[132] G. M. Palma, K. A. Suominen, and A. K. Ekert, Proceedings: Mathematical, Physical and Engineering Sciences **452**, 567 (1996), ISSN 13645021, URL http://dx.doi.org/10.2307/52838.

[133] S. F. Huelga, C. Macchiavello, T. Pellizzari, A. K. Ekert, M. B. Plenio, and J. I. Cirac, Physical Review Letters **79**, 3865 (1997), URL http://dx.doi.org/10.1103/PhysRevLett.79.3865.

[134] U. Dorner (2011), 1102.1361, URL http://arxiv.org/abs/1102.1361.

[135] M. Chwalla, J. Benhelm, K. Kim, G. Kirchmair, T. Monz, M. Riebe, P. Schindler, A. S. Villar, W. Hänsel, C. F. Roos, et al., Physical Review Letters **102**, 023002+ (2009), URL http://dx.doi.org/10.1103/PhysRevLett.102.023002.

[136] C. F. Roos, T. Monz, K. Kim, M. Riebe, H. Häffner, D. F. V. James, and R. Blatt, Physical Review A **77**, 040302+ (2008), URL http://dx.doi.org/10.1103/PhysRevA.77.040302.

[137] A. H. Myerson, D. J. Szwer, S. C. Webster, D. T. C. Allcock, M. J. Curtis, G. Imreh, J. A. Sherman, D. N. Stacey, A. M. Steane, and D. M. Lucas, Physical Review Letters **100**, 200502+ (2008), URL http://dx.doi.org/10.1103/PhysRevLett.100.200502.

[138] A. H. Burrell, D. J. Szwer, S. C. Webster, and D. M. Lucas, Physical Review A **81**, 040302+ (2010), URL http://dx.doi.org/10.1103/PhysRevA.81.040302.

Index